A Study on Dense Plasmas using Molecular Dynamics and X-Ray Scattering Techniques

Paul Mabey

Keble College

University of Oxford

A thesis submitted for the degree of

Doctor of Philosophy

Michaelmas 2016

This thesis is dedicated to my parents,
Margaret and John Mabey

Acknowledgements

Firstly, I would like to thank my supervisor, Professor Gianluca Gregori, for his help and guidance during the course of my DPhil. The opportunities given to me over this time have been numerous, and surely without his intuition and expertise, this body of work would be far worse off. I have also had the privilege of working with my secondary supervisor, Scott Richardson, and his insight and experience has been invaluable throughout.

I must also thank Tom White for his input, firstly as a fellow DPhil student in the group and more recently as a post-doc, in making much of this work happen. I would also like to thank all of the other members in the group, past and present, for their advice, particularly during the weekly group meetings. The other members of the Simon Room must also be thanked for their constant eagerness to have a coffee break in the biochemistry cafe.

My housemates in my time at Oxford also deserve thanks for putting up with me for so long. Penultimately I would like to thank my fellow members of Keble MCR, far too numerous to name individually, for their continued willingness to grab lunch or go for a drink at the end (or indeed the middle) of a hard week of work. I would have finished far sooner without you.

Finally, and most importantly, I wish to thank my parents for their unerring support in helping me reach where I am today.

Abstract

Matter exists in the cores of planets and the crusts of neutron stars, as well as the inside of inertial fusion experiments, in the warm dense matter (WDM) regime. This type of matter, defined by temperatures of several electronvolts and densities comparable to solids, is characterised by long-range Coulomb interactions between ions and non-negligible electron degeneracy, and is therefore inherently difficult to model theoretically.

In this work, time resolved X-ray diffraction is used to study the temporal evolution of a laser-heated gold sample, from solid state towards WDM. The electron-ion equilibration time is extracted through the use of molecular dynamics simulations employing the two-temperature model, with the results compared to other methods.

Laser-produced X-ray sources are focused to high intensities, through the use of a polycapillary lens. This setup is thoroughly characterised, with the results suggesting a vastly improved signal-to-noise ratio could be achieved in many pump-probe experiments by employing this schematic.

Numerical predictions for the dynamic ion-ion structure factor of warm dense aluminium are presented, with significant changes observed when dissipative processes are included by Langevin dynamics. The results are compared to recent experimental data, suggesting electron-ion dynamical effects could play a crucial role in the dynamic properties of matter in the WDM regime.

Role of the Author in this Work

This thesis contains both theoretical and experimental results based on the creation, diagnosis and simulation of high energy density states of matter. The work presented in this thesis, as with most scientific endeavours, is the result of a collaborative effort from many people and this section will therefore attempt to outline the author's contributions.

Chapter 1 is an introduction to the thesis, and is aimed at motivating the experiments and theoretical studies described later on. It contains no original work and all sources are identified throughout.

In chapter 2, some of the background theory necessary to understand the work presented in later chapters is outlined. It also contains no original work by the author and all sources are again identified where appropriate.

In chapter 3, the results of a collaborative work are presented. The work has led to a publication in Physical Review B [1]. The experiment was conceived by A. Higginbotham and the team led by T. G. White, with the analysis and molecular dynamics simulations performed by the author. The paper was written primarily by T. G. White, with some parts written by the author.

In chapter 4, the results of another collaborative work, published in the Journal of Instrumentation [2], are described. The experiment described

was conceived by G. Gregori and the team led by the author. All preparatory work for the experiment, as well as subsequent data analysis and interpretation was performed by the author. The paper was also written solely by the author.

In chapter 5, the results of a theoretical work, published in Nature Communications [3], are presented. The original idea for the work was conceived by G. Gregori, with the work being carried out by S. Richardson and the author. The large scale simulations required by this work were performed by S. Richardson on the AWE supercomputer, while all subsequent analysis and comparison was performed by the author. The paper was also written by the author.

The work presented in chapter 6 is the result of a large collaboration, which is, as of now, unpublished. The experiment was conceived by G. Gregori and led by T. G. White. Although the author did not carry out the experiment, a brief outline is included here for completeness and to help with comprehension. The analysis of the data using molecular dynamics and hydrodynamics was carried out by the author.

Chapter 7 contains no new work and brings together the preceding four chapters.

Contents

List of Figures

List of Tables

Chapter 1

Introduction

"The Earth is the cradle of the mind, but one cannot live in a cradle forever."

- *Konstantin Eduardovich Tsiolkovsky*, 1911 CE

The matter we encounter on Earth, in our everyday lives, is often split into three categories: solids (such as the minerals in the Earth's crust); liquids (such as the water in its oceans); and gases (such as the air in the atmosphere). With moderate temperatures of ~ 300 K and an average pressure of 1 atm, the conditions here favour the formation of molecular structures composed of neutral atoms. It is therefore this kind of matter that has been the subject of our investigation since long before the beginning of the scientific revolution.

1.1 High energy density physics

The majority of the visible matter in the universe, however, exists at much higher temperatures and pressures than those encountered here on Earth. Indeed, one only has to look beneath the crust, towards the Earth's core, to encounter strange types of matter that are completely different to those we see around us on the surface [4]. Further afield, matter exists at even higher temperatures in stars [5], gas giants like

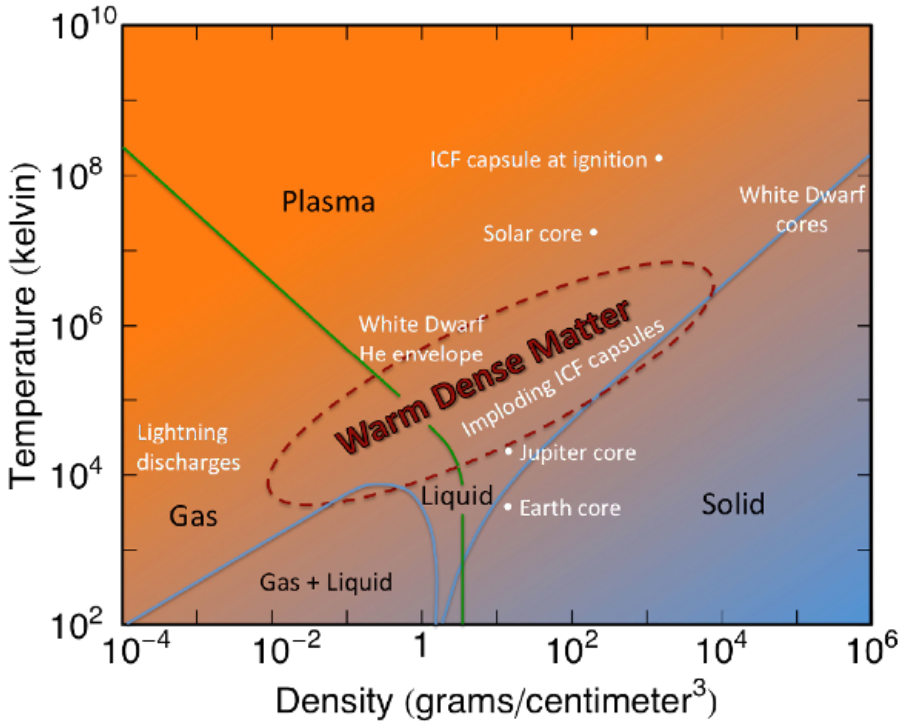

Figure 1.1: Temperature-density phase diagram, showing the relative position of commonly found states of matter and various celestial objects. Reproduced from [10].

Jupiter or Saturn [6], or even more exotic phenomena such as black holes [7] or neutron stars [8]. Here, the stable molecular structures, commonplace on Earth, cannot exist. Instead, we find a plethora of different structures, ranging from very dense charged matter, seemingly arranged in crystalline lattices, to very low density classical plasmas at very high temperatures. Figure 1.1 summarises the typical temperatures and densities of some of these states of matter. The study of matter in these conditions is now collectively referred to as high energy density physics (HEDP). For further reading, ref [9] provides a comprehensive introduction to this field.

1.1.1 Warm dense matter

The field of HEDP is a broad and diverse one: the National Plasma Science Committee defines this area of physics as referring to any system or material with an energy

density above 10^{11} J m^{-3}, equivalent to a pressure on the order of 1 Mbar [11]. Indeed, it is too general to be studied with any great detail in this work. Instead we confine ourselves to a particular subsection of the high energy density phase space, known as warm dense matter (WDM), also referred to in some text books as a strongly-coupled or non-ideal plasma. This regime is characterised by high pressures ($\sim$ 1 Mbar), moderate temperatures ($\sim$ 1 eV[1]) and solid densities, as highlighted in figure 1.1. The computational, theoretical and experimental study of this type of matter represents a significant challenge, as it lies in an area of phase space between traditional solid-state physics and classical plasma physics. Strongly coupled ions, different electron and ion temperatures, together with non-negligible electron degeneracy strongly affect ion dynamics [12]. An excellent introduction to the basics of this part of phase space and the current status of the field can be found in ref [10].

In astrophysics, WDM represents the state of matter typically found in planetary cores [13] and the crusts of neutron stars [14]. With the recent discovery of many new exoplanets, particularly with the help of the Kepler Space Telescope, the number of known planets has increased significantly recently, reaching over 1700 at last count, and set to increase even more in future years [15]. Many unanswered questions about their structure, formation and evolution are, however, still outstanding, and hence the need to understand the WDM regime is becoming increasingly more important [16].

The WDM state is also encountered in inertial confinement fusion experiments; the deuterium-tritium capsule passing through the warm dense state en route to potential ignition in a hotter state. In this case, understanding the transient WDM regime is important for modelling the instabilities and energy transfer [17, 18].

[1]It is often convenient to use electronvolts, rather than Kelvin, as the temperature units in this field. 1 eV = 11604.505 K

1.2 High energy density physics in the laboratory

Until quite recently, our understanding of HEDP was limited by our inability to create such states of matter in the laboratory - there is only so much one can learn about the properties of matter seen through a telescope, light years away. The creation of WDM (or any high energy density state of matter in general), here on Earth, requires depositing a large amount of energy into a particular system within a very short time frame. Hence it was in the 1940s with the invention and development of nuclear weapons that originally drove much of the research on matter at these conditions. With the Comprehensive Nuclear-Test-Ban Treaty, however, these types of experiments are no longer carried out. Nevertheless, the desire to study high energy density states of matter, for the reasons stated above, remains. The quite recent advent of high-power optical lasers, then, has come at an opportune moment and has made this possible.

1.2.1 High-power optical lasers

In 1960, Theodore H. Maiman developed the first functional optical laser by using flash-lamps to pump a ruby crystal emitting light at a wavelength of 694 nm [20]. The first lasers had very low average power and generally operated either in continuous wave mode or with very long pulse lengths. For this reason, they were not able to bring matter to the conditions needed to study HEDP. In the following years, however, each advancement in laser technology, such as mode-locking [21], Q-Switching [22] or chirped pulse amplification (CPA) [23, 24], increased the region of phase space able to be explored. This allowed for ever higher temperatures and pressures to be accessed, with even modest laser systems by today's standards able to create the states of matter necessary to study HEDP. Additionally, the precision with which laser pulses can

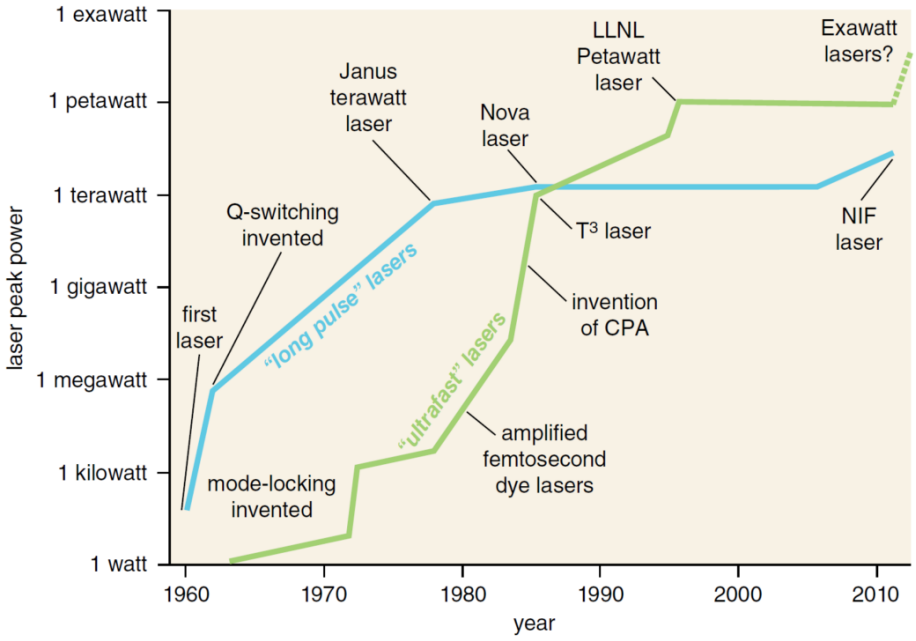

Figure 1.2: Overview of the advances in laser power from 1960s to early 2010s. The introduction of a new laser technology leads to a sharp jump in the power reached, followed by steady increase until another new technology becomes available. Reproduced from ref [19].

now be controlled both spatially and temporally has lead to a greater precision and reproducibility of the temperature and density of states accessible.

It was in the 1970s that lasers such as Shiva, and Janus, Livermore, CA, USA began to work in the terawatt power regime [25]. Facilities such as Omega, in Rochester, NY, USA [26]; Nova, in Livermore, CA, USA [27]; Gekko XII, in Osaka, Japan [28]; LULI, in Paris, France [29]; and Vulcan in Harwell, UK [30] followed in the next two decades, with multiple beam lines and laser energy surpassing the kilojoule level. Higher energies still became available in the 2000s, with the NIF, Livermore, CA, USA [31] and Orion, Aldermaston, UK, [32] as well as upgrades to some of the older laser facilities worldwide.

1.2.2 X-rays as a diagnostic

Although high-power laser systems offer one means of creating a WDM state in the laboratory, the question of how best to study this state still remains. The fleeting nature of the matter created by the interaction of a high-power laser with a target means the window of opportunity to learn about its properties is very small (from ns to μs). The need to make measurements on these short timescales severely limits the techniques available to the experimenter.

Commonly used methods, employed to great effect within the field, include neutron scattering [33, 34]; electron scattering [35]; optical techniques such as VISAR [36, 37]; proton radiography [38, 39] and spectroscopy [40, 41, 42]. Another possible method of extracting information about the properties of matter on these timescales is through the use of X-rays, which will be the primary diagnostic discussed in this thesis.

Since their discovery, X-rays have been responsible for many historical scientific breakthroughs including, but by no means limited to, the determination of crystalline structures in 1913 [43] and the discovery of the double helical nature of DNA in 1953 [44]. The wavelength of X-rays (conventionally 0.01 - 10 nm or 120 eV to 120 keV) makes them perfectly suited for probing closely packed or optically dense systems [45]. Following the first records of the diffraction pattern from a shocked solid recorded in 1969 [46], work has been performed to increase the brightness and decrease the pulse length of X-ray sources. In turn, this has led to two separate strands of research into different types of sources. The first of these notes that upon interaction with a solid target, a high-power optical laser not only creates a high energy density state of matter, but also copious amounts of X-rays through various processes that will be explained in Chapter 2. Typical experiments rely on one laser beam to create the state of interest and a second beam to probe it [47, 48]. The second commonly used

type of X-ray source is based on particle accelerator technology. The development of accelerator sources is typically divided into generations. Of particular interest is the fourth of these, where a high intensity X-ray beam is passed through an undulator to produce an ultra-short coherent X-ray beam [49].

1.3 Current status of the field

In recent years, larger, more powerful laser facilities coupled with faster, high performance computers have enabled ever more sophisticated experimental techniques or theoretical models to be employed. As a result, our understanding of the WDM regime has grown rapidly. However, there are still many important questions that remain unanswered. One of these uncertainties concerns the equation of state of high temperature and pressure systems [50, 51, 52]. This has a significant impact on theories describing planetary formation and evolution [53]. Moreover, the microscopic structure of matter found in the cores of planets and crusts of stars, remains uncertain. For example, it is theorised that matter re-crystallises under high pressures [54], and while initial experiments confirm this in some cases, many of these lattice structures have not yet been observed experimentally.

Also of great interest is the time scale of energy transfer between the electron and ion subsystems in non-equilibrium states [55, 56, 57, 58]. One typically assumes that the laser-produced high energy density state being probed is in thermal equilibrium but there is evidence to suggest this is not always the case [59, 60]. The experimental measurement of electron-ion equilibration rates is not only important for assessing the validity of many WDM studies, but also for understanding much of the physics of the WDM regime [61].

The stopping power of WDM represents another unknown quantity [62] with very few

experimental measurements having been made [63]. This has important implications for inertial confinement fusion, where understanding the transport of the α-particle in plasmas at extreme conditions is required to accurately model fusion experiments. Similarly, what are the transport coefficients (viscosity, diffusion coefficient, etc.) [64] or conductivities [65, 66, 67] of these dense plasmas? Do they follow trends that are observed at standard conditions or do they differ significantly?

Finally, the temperatures and pressures at which radiative effects play an important role is still unknown. How do we include these effects in commonly-used models and is it right to assume they are negligible at moderate temperatures [68, 69, 70]?

These are just several of the larger questions still yet to be answered, but there are many more smaller problems still to be solved as well. The field is still in its infancy and has progressed remarkably since its inception, but a great deal more work is required if we are to complete our understanding of this regime.

1.4 Thesis layout

This section briefly outlines the structure of the thesis and its contents.

In chapter 2, an explanation of some of the elementary theoretical concepts, upon which the work on this thesis is built, is provided. The topics discussed include: elementary plasma physics; correlation functions; laser-solid interactions including absorption processes, shocks and X-ray emission; X-ray scattering and diffraction; and molecular dynamics.

In chapter 3, the rate of temperature equilibration between electrons and ions in laser heated targets is determined. An experiment, employing X-ray diffraction as

the primary diagnostic, is performed with the aim of measuring the rate of equilibration in a gold sample. This is achieved, in part, through the use of state-of-the-art molecular dynamics simulations. The experiment was performed using the laser lab at Oxford University, demonstrating that important measurements can be taken on modest laser systems, without the need to always use large national facilities.

In chapter 4, a method of improving the quality of X-ray diagnostics in pump-probe experiments is introduced. A common problem with experiments of this type is the inability to distinguish the X-ray signal from the noise produced by the laser-target interactions. Instead, a new scheme, involving X-ray optics, is trialled and characterised in order to use obtain higher quality measurements in the future.

In chapter 5, novel simulations, including dynamical electron-ion effects in the WDM regime, are presented. This is the first time such calculations have been performed. The dynamic structure factor and dispersion relation are determined, and found to differ vastly from conventional techniques.

In chapter 6, the simulation techniques outlined in the previous chapter, are compared to experimental data from an experiment at a free-electron laser. Generalised hydrodynamics is also proposed as a fast, analytical method of determining dynamic structure factors.

The thesis concludes with chapter 7, drawing together the work performed and suggesting possible directions for future research.

Chapter 2

Background Theory

"There is no greater wealth than wisdom, no greater poverty than ignorance."

- *Ali bin Abi Talib*, 7th Century CE

This chapter will cover some of the background theory required for understanding the original work presented later in this thesis. Nothing described in this chapter is original, and indeed, may be found in many plasma physics textbooks. It is included here nonetheless as a self-contained, convenient reference to the elementary physics, upon which the later chapters are built.

2.1 Elementary plasma physics

Plasma is, along with solids, liquids and gases, one of the four fundamental states of matter. It is commonly defined as a quasi-neutral system of charged particles. Matter at high temperatures, where the electrons in the system have sufficient energy to be ionised, exists naturally in the plasma state. Classical plasma physics generally describes high temperature, low density systems, where ions are treated as point particles and ion-ion interactions are either treated as a perturbation or not at all. However, non-ideal plasmas, such as warm dense matter, are characterised

by strong ion-ion correlations and hence much of classical plasma physics does not apply. Instead, one may find short range order, like that found in liquids, or indeed long range order, such as that found in a solid. In either case, this prevents the use of classical statistics-based plasma physics techniques and necessitates the use of more sophisticated models.

We begin by introducing several concepts fundamental to the nature of any plasma. The first of these concerns the nature of the electrostatic field and the concept of quasi-neutrality. One may expect that the Coulomb force due to any given particle extends over the whole volume of the plasma. This is in fact, not the case. Debye, in 1923, was the first to point our that the field due to any charge imbalance is shielded so that its influence is effectively constrained to a finite range, commonly known as the Debye screening length, λ_D. The Coulomb field surrounding a positive ion in a plasma is screened by the negatively charged electrons that are attracted to it. Classically, it can be shown to be,

$$\lambda_D = \left(\frac{\epsilon_0 k_B T_e}{n_e e^2} \right)^{1/2} \quad , \tag{2.1}$$

where T_e is the electron temperature and n_e the electron number density. The Debye length then defines a region around an ion known as the Debye sphere within which charge neutrality may not be maintained. Conversely, beyond this sphere, the plasma remains effectively neutral. The potential, $v(r)$ between ions can be written as,

$$v(r) = \frac{Z^* e}{r} e^{-r/\lambda_D} \quad , \tag{2.2}$$

where Z^* is the average ionisation state of the system. This form is typically referred to as the screened Coulomb or Yukawa potential.

Another useful quantity is the Debye number, N_D, defined as the average number

of electrons within the Debye sphere,

$$N_D = \frac{4}{3}\pi n_e \lambda_D^3 \quad . \tag{2.3}$$

A plasma is generally considered ideal if this number approaches infinity. This is not the case for dense plasmas, however, where there may be only a handful or even fractions of particles present. Broadly speaking, the larger this number, the less likely it is there will be a significant resultant force on any particle due to collisions. It can also be used, therefore, as a measure of the dominance of collective interactions over collisional effects. The most fundamental of these collective interactions are plasma oscillations that arise from a charge imbalance. These occur at a characteristic frequency given by,

$$\omega_e = \left(\frac{n_e e^2}{m_e \epsilon_0}\right)^{1/2} \quad , \tag{2.4}$$

for the electrons and,

$$\omega_i = \left(\frac{n_i Z^{*2} e^2}{m_i \epsilon_0}\right)^{1/2} \quad , \tag{2.5}$$

for the ions, where m_e and m_i refer to the electronic and ionic masses respectively. Both quantities play an important role in both ideal and dense plasmas, although it is the ionic frequency that is of primary interest in this work, and will be discussed at greater length in chapter 5.

There are several parameters that have been defined specifically in the context of WDM and are generally not used in classical plasma physics. The first of these is the degeneracy parameter, Θ, which estimates the role of quantum statistical effects in the system. This parameter is defined by the ratio of the thermal energy and the Fermi energy, E_f,

$$\Theta = \frac{k_B T_e}{E_f} \quad , \quad E_f = \frac{\hbar^2}{2m_e}(3\pi^2 n_e)^{2/3} \quad . \tag{2.6}$$

When this parameter is small, the electrons are in a degenerate state and quantum statistics play a crucial role in their description. In particular, if the electrons are in lower energy states, the Pauli exclusion principle becomes important, such as in neutron stars. In a plasma that is fully degenerate, one must introduce a new screening length to replace that proposed by Debye. This is called the Thomas-Fermi screening length and is given by,

$$\lambda_{TF} = \left(\frac{2\epsilon_0 E_f}{3Z^{*2} n_e^2} \right)^{1/2} \quad . \tag{2.7}$$

In practice, in the WDM regime, the plasma is partially degenerate and so neither of the two limiting cases are entirely accurate. Success is often achieved by interpolating between the two [71].

Another useful quantity is the ion-ion coupling parameter, Γ, defined as the ratio of of the kinetic to potential energy in a system,

$$\Gamma = \frac{PE}{KE} = \frac{Z^2}{4\pi\epsilon_0 a} \times \frac{1}{k_B T_i} \quad , \tag{2.8}$$

wherer a is the Wigner-Seitz radius; that is the inter-particle separation, which is given by,

$$a = (3/4\pi n_i)^{1/3} \quad . \tag{2.9}$$

In chapter 1, the WDM state was defined in terms of temperature and pressure values. However, it may equally be defined as as the range of states for which Γ is roughly of order unity. When $\Gamma \gg 1$ the kinetic energy term dominates and classical plasma physics applies. When $\Gamma \ll 1$ the Coulomb interactions are greater than the kinetic energy and the ions arrange themselves into their equilibrium lattice positions [54].

2.2 Structure of matter

The purpose of this section is to give a brief introduction to some important functions which are commonly used to quantify the structural order within systems. We begin by looking at the states of matter that are more common in every day life and more familiar to the reader: solids, liquids and gases; and from there progress to the WDM regime, which, as we will see, shares some properties with all three of these states, while also exhibiting fundamental differences. It is also worth noting now the distinction between the terms *state* and *phase*, which are often used interchangeably. This should generally be avoided, as within a particular state there are often multiple phases of matter. E.g. shock compressed iron undergoes a solid-solid phase transition, changing its internal crystalline structure, but remaining in the same state throughout.

2.2.1 Radial distribution function

The first quantity of interest is the radial distribution function (RDF) denoted by the symbol, $g(r)$, which measures the structural order between ions in a system. This function is introduced by writing the average number of ions contained in a spherical shell of thickness δr at a distance r from any given reference ion as,

$$4\pi n_i \int_r^{r+\delta r} r^2 g(r) dr \quad . \tag{2.10}$$

In the limiting case of $g(r) = 1$ (an ideal gas), the number of ions one expects in the shell is simply the ion number density multiplied by the volume of the shell. This scenario represents a complete lack of structural order between the ions; regardless of the distance and direction one looks from a given reference ion, the average number of ions per unit volume is the same. For a crystalline solid at absolute zero, this function would be a sum of delta functions whose locations would be determined by the lattice

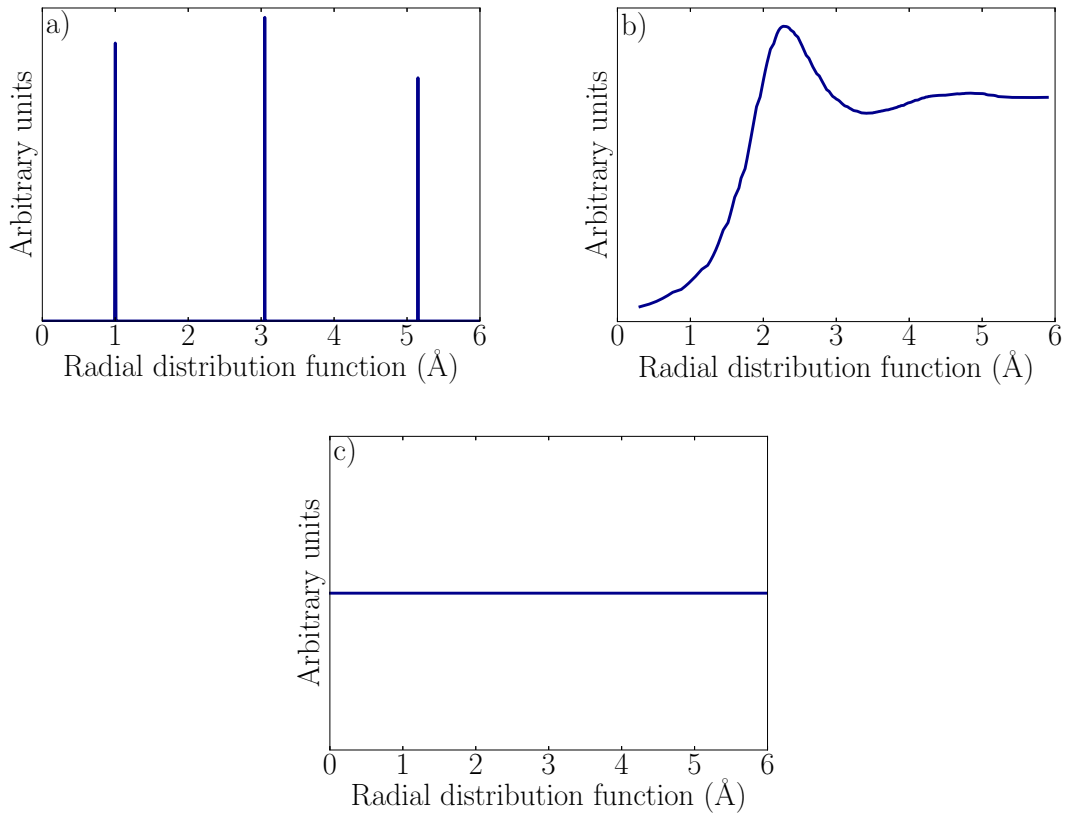

Figure 2.1: Example radial distribution functions for a) a solid at 0 K, b) a liquid at arbitrary conditions and c) an ideal gas with no inter-particle forces. Note the solid case *does not* tend to unity at large distances, indicating the presence of long-range order not seen in the liquid and gas cases.

spacings in the crystal. For liquids, the functional form of $g(r)$ is non-trivial but is generally a smooth curve with a peak at some given r value corresponding to a preferred distance between particles. The lack of long-range order means that $g(r)$ also tends to unity at large distances. Figure 2.1 shows these three cases explicitly. In general, WDM behaves more like the liquid form shown here, with strong short range order but weaker long range order. The higher the coupling parameter of the plasma, however, the stronger this long range order becomes, with re-crystallisation observed at very high temperature and density conditions. The radial distribution function plays an important role in the physics of non-ideal plasmas, partly because thermodynamic properties can be written as integrals over $g(r)$ [72].

2.2.2 Structure factors

The radial distribution function, introduced in the previous section, is an example of a correlation function. A correlation function measures the statistical correlation between one or more functions at multiple points. The radial distribution function describes the correlation in density at two different points in space within the system and is applied to some given moment in time. The obvious generalisation would be to seek a *time-dependent* correlation function that describes density correlations in both space *and* time.

Formally, a time dependent correlation function, C_{AB}, is defined generally as,

$$C_{AB} = \langle A(t)B^*(0)\rangle \ , \tag{2.11}$$

where A and B are dynamical variables; functions that depend on the positions and momenta of the N particle system. The angular brackets represent an equilibrium or thermal average, that is an average weighted by the partition function for a system in thermodynamic equilibrium at a given temperature. As our goal is to calculate the density-density correlations in space and time, A and B are the same and so the function is known as an auto-correlation function.

In order to construct our density-density time dependent auto-correlation function, we follow the derivation given by ref [73] and begin by defining $\hat{\mathbf{r}}_i$ as the position operator of the ith atom. The Heisenberg operator of the microscopic density can then be written as,

$$\hat{\rho}(\mathbf{r}, t) = \sum_{i=0}^{N} \delta(\mathbf{r} - \mathbf{r_i}) \ . \tag{2.12}$$

From the real space microscopic density, the correlations between the density at two points in space and time are defined with the van Hove function,

$$G(\mathbf{r}, \mathbf{r}', t) = \frac{1}{N}\langle \hat{\rho}(\mathbf{r}' + \mathbf{r}, t)\hat{\rho}(\mathbf{r}', 0)\rangle \quad . \tag{2.13}$$

For a homogeneous system, this function can be integrated over $\mathbf{r}$, removing the dependence on the choice of origin, giving,

$$\begin{aligned} G(\mathbf{r}, t) &= \frac{1}{N}\left\langle \int \hat{\rho}(\mathbf{r}' + \mathbf{r}, t)\hat{\rho}(\mathbf{r}', 0)d\mathbf{r}' \right\rangle \\ &= \frac{1}{N}\left\langle \sum_{i=0}^{N}\sum_{j=0}^{N} \delta(\mathbf{r} - \mathbf{r}_i(t) + \mathbf{r}_j(0)) \right\rangle \quad . \end{aligned} \tag{2.14}$$

The density-density correlation function can then be split into two terms. The first is the self-correlation term and describes a particle's correlation with itself; the second is the pair distribution function and describes the correlation between two different particles within the system,

$$G(\mathbf{r}, t) = G_s(\mathbf{r}, t) + G_p(\mathbf{r}, t) \quad , \tag{2.15}$$

with,

$$G_s(\mathbf{r}, t) = \frac{1}{N}\left\langle \sum_{i=0}^{N} \delta(\mathbf{r} - \mathbf{r}_i(t) + \hat{\mathbf{r}}_i(0)) \right\rangle \quad , \tag{2.16}$$

and,

$$G_p(\mathbf{r}, t) = \frac{1}{N}\left\langle \sum_{i=0}^{N}\sum_{i\neq j}^{N} \delta(\mathbf{r} - \mathbf{r}_i(t) + \hat{\mathbf{r}}_j(0)) \right\rangle \quad . \tag{2.17}$$

We now examine the static case to compare to the RDF described previously. Inserting $t = 0$ into equation 2.15 and simplifying gives,

$$G(\mathbf{r}, 0) = \delta(\mathbf{r}) + \rho g(\mathbf{r}) \quad . \tag{2.18}$$

Here, the first term is simply the probability of finding the same particle at a given position, r, away from its initial location, which reduces to a delta function. The

second term, represents the probability of finding a different particle at a distance, r, given that there is a particle at the origin. This is simply another statement of the RDF, so our new function may be thought of as a time-dependent radial distribution function.

The next step is to take the Fourier transform of this quantity. This makes it, in a way, less intuitive: it can no longer be directly thought of as the probability of finding a particle at some particular distance away from another particle. On the other hand, the Fourier transform is directly measurable in scattering experiments, thus making it a useful quantity. As we are dealing with dynamic variables, we need to perform the transform in both space and time. We start with the spatial Fourier transform of the van Hove function,

$$F(\mathbf{k},t) = \int_{-\infty}^{\infty} G(\mathbf{r},t)\exp(-i\mathbf{k}\cdot\mathbf{r})d\mathbf{r} \quad , \tag{2.19}$$

which is a quantity known as the intermediate scattering function (ISF). The temporal Fourier transform of this is then the dynamic structure factor (DSF),

$$S(\mathbf{k},\omega) = \int_{-\infty}^{\infty} F(\mathbf{k},t)\exp(-i\omega t)d\mathbf{t} \quad , \tag{2.20}$$

an experimentally measurable quantity, which is described further in section 2.5. We now introduce the static structure factor (SSF) denoted by the symbol, $S(\mathbf{k})$, a quantity closely related to the radial distribution function but whereas the latter is in real space, the SSF is in Fourier space. Formally, the SSF is simply the frequency integral of the DSF,

$$S(\mathbf{k}) = \frac{1}{N}\int_{-\infty}^{\infty} S(\mathbf{k},\omega)d\omega \quad . \tag{2.21}$$

The SSF is, along with the DSF, also an experimentally measurable quantity, making them both very important measures of dense plasmas. As the phases of matter

considered in this thesis are generally radially isotropic (liquids, plasmas etc.), one may drop the directional dependence of the quantities above in these cases. The DSF in relation to this work, will be considered in greater detail in chapters 5 and 6.

2.3 Laser-matter interactions

In the experiments described in this work, high energy density states of matter are created through the interaction of a high-power laser with a solid target. Additionally, in chapter 3, X-rays, produced with laser sources, are used to diagnose the state of matter under investigation, while in chapter 4 a potential improvement on this method of diagnosis is proposed.

In this section, we first discuss the interaction of a high intensity laser with a solid target and the relevant processes involved. It is important to make the distinction between laser-matter interactions performed with either a *long* or *short* pulse laser beam, as this dictates some of the processes involved in the interaction as well as the timescales in the experiment. Short pulse lasers typically have a pulse length in the region of picoseconds or femtoseconds, with intensities touching 10^{23} W cm^{-2}. Long pulse lasers, on the other hand, have pulse lengths on the order of nanoseconds and generally the intensity does not exceed 10^{16} or 10^{17} W cm^{-2}. The difference in energy between the two types of lasers is also marked, with long pulse lasers often carrying an order of magnitude or more energy than their short pulse counterparts. For this reason, long pulse lasers are often the preferred means of driving samples to high temperatures and pressures. On the other hand, short pulse lasers are often used for probing dynamically evolving systems, due to their shorter pulse length.

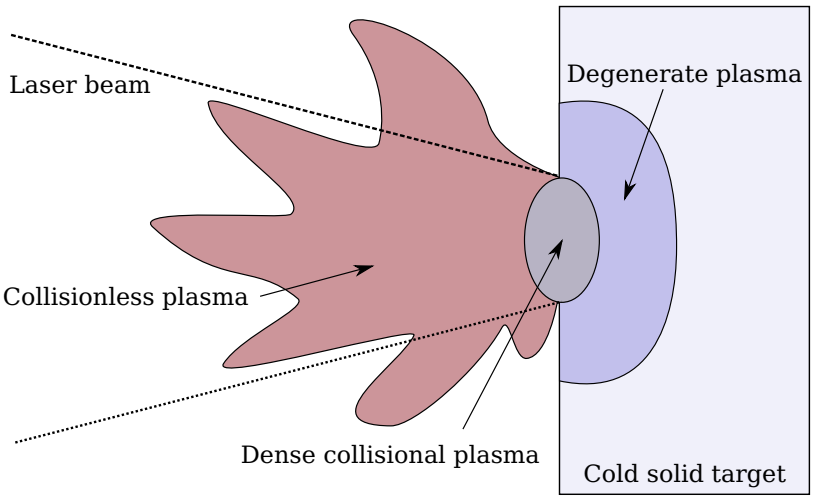

Figure 2.2: A high intensity laser beam (incident from the left) interacts with a cold solid target. Three distinct regions are setup: a classical collisionless coronal plasma away from the front surface of the target; a dense collisional plasma at the point of the laser interaction and an even more dense, degenerate plasma within the target.

2.3.1 Laser energy absorption in matter

Upon interaction with a cold solid target, a laser with an intensity above about 10^{13} W cm^{-2} (the high-intensity regime) may create several states of matter that have a wide range of conditions. Figure 2.2 shows the three different regions typically found in these interactions. These lasers deposit their energy into the target material on a very short timescale (i.e. less than the pulse duration of the laser), after which the beam primarily acts on the collisionless coronal plasma, with various energy deposition processes involved.

2.3.1.1 Inverse bremsstrahlung absorption

The coronal plasma here generally consists of material that is partially or fully ionised, and since the photon energy is generally much smaller than the ionisation potentials, the interaction of the laser beam with the plasma is dominated by interactions between the laser photons and free electrons. This phenomenon is the inverse of the well-known bremsstrahlung process [74, 75, 76]. Photos accelerate electrons in the vicinity of

ions and thus the energy of the laser beam is transferred to the free electrons in free-free inverse bremsstrahlung transitions. Averaging over a Maxwell-Boltzmann thermal distribution of free electron energies, one can write the inverse bremsstrahlung coefficient, κ_{IB}, as,

$$\kappa_{IB} = \sqrt{2\pi}\,\frac{16\pi\, Z^2\, n_e n_i\, e^6 \ln(\Lambda_{ei})}{3\, c\, (m_e k_B T_e)^{3/2}\ \omega_0^2\ \sqrt{\epsilon}}\ , \tag{2.22}$$

where ω_0 is the angular frequency of the incident laser beam. The dielectric permittivity, ϵ, is given by,

$$\epsilon = 1 - \frac{\omega_e^2}{\omega_0^2}\ , \tag{2.23}$$

and the Coulomb logarithm, $\ln(\Lambda_{ei})$, is given by [77],

$$\ln(\Lambda_{ei}) = 18 - \ln\left(\frac{(n_e[10^{19}\mathrm{m}^{-3}])^{0.5}}{(k_B T_e[1\mathrm{keV}])^{1.5}}\right)\ . \tag{2.24}$$

The inverse bremsstrahlung coefficient is proportional to $T_e^{-3/2}$, which means that as electron temperature decreases, absorption by this process increases. Therefore, lower energy electrons are preferentially heated, keeping the plasma close to a thermodynamic equilibrium. It should also be noted that the inverse bremsstrahlung coefficient is a real number if, and only if, the laser light has a frequency greater than the electron plasma frequency. In practical terms, this means that laser light can only propagate and be absorbed in plasma that is less dense than some critical density. This density, n_c is dependent on the wavelength of the laser beam, λ, and can be written as,

$$n_c(\mathrm{cm}^{-3}) = 8.8 \times 10^{20}/[\lambda(\mu\mathrm{m})]^2\ . \tag{2.25}$$

Finally, one must also be aware that if the laser beam intensity is sufficiently high, the electric field can become strong enough to distort the electron distribution, thus making the inverse bremsstrahlung coefficient dependent on intensity, although this

does not apply in this work.

2.3.1.2 Resonance absorption

Energy that is left in the beam when it reaches the critical density surface may be absorbed in a process known as resonance absorption, where the electromagnetic wave couples with a longitudinal electron plasma wave, with frequency ω_e [78]. The oscillation of the electric field component of the electromagnetic wave is in resonance with the oscillation of the electrons in the electron plasma wave. This coupling, however, can only happen if there is some component of the electric field vector in the direction of the plasma density gradient. Therefore, the angle at which the laser beam is incident on the target must be oblique to its surface. It is also necessary that the polarisation of the laser is not linearly polarised, parallel to the plasma surface, otherwise it will simply be specularly reflected.

An electromagnetic wave incident at an angle, θ, to the surface of a plasma does not reflect at the critical density surface, but rather at the lower density of $n_c\cos^2\theta$. Some of the energy in the beam reaches the critical density by the quantum-mechanical process of quantum tunneling, with the remainder being specularly reflected at the turning point. When the density gradient of the plasma is very steep, the turning point and the critical-density point are close together, and hence resonance absorption is an efficient process. This efficiency is a function of the angle of incidence of the laser and the density-gradient scale length, with the resonance absorption fraction f_{ra} able to be written as:

$$f_{ra} = \frac{1}{2}\phi^2(\tau) \ , \tag{2.26}$$

with

$$\phi(\tau) = 2.10\tau e^{-\frac{2}{3}\tau^3} \ , \tag{2.27}$$

and

$$\tau = (k_0 L)^{1/3} \sin(\theta) \quad , \tag{2.28}$$

where k_0 is the wavenumber of the incident laser beam and $L = n_e/\nabla n_e$ is the electron density gradient scale length. In designing experiments, one often maximises this fraction in order to deposit more energy into the target, usually by considering the laser angle of incidence. Too large and the beam will be reflected too far away from the critical density surface, whereas too small and the component of the electric field vector parallel to the density gradient is too small for coupling to occur. As with the case of inverse bremsstrahlung absorption, these formulae break down at very high laser intensities where relativistic effects become important.

The relative importance of these processes changes with intensity. Inverse bremsstrahlung absorption increases with target ionisation, plasma density, and the length of underdense plasma, and decreases at high plasma temperatures. It is thus strongest for lower laser intensities, shorter laser wavelengths, and longer laser pulses. Conversely, resonance absorption tends to dominate at higher laser intensities and shorter laser pulses.

2.3.1.3 Lower intensity lasers

When the laser intensity incident on target is very low, to the extent that very few atoms are ionised, one finds no, or very little, coronal plasma. This fundamentally changes the absorption mechanism by which the sample is heated. Rather than causing free-free transitions, the laser pulse instead interacts with the bound electrons in the sample. This interaction takes a different form for conducting materials and dielectrics, depending on the population of electrons in the conduction band.

In this work, we are only interested in metals, so we focus on the case of conducting materials here. An electromagnetic wave propagating into such a material can be shown to be damped as it passes through the medium. The scale length of this damping (the distance over which the the wave is attenuated by $1/e$) is called the skin depth, δ, and can be shown to be,

$$\delta \approx \frac{1}{\sqrt{2\pi\omega_0\mu\sigma}} \ , \tag{2.29}$$

where μ is the magnetic permeability and σ is the conductivity of the material. Very little laser energy penetrates into the conductor to any depth much greater than this. For many conducting metals, the skin depth is of the order of tens of nanometres in the case of optical laser light.

This prescription is only valid at very low laser intensities where the electrons only undergo bound-bound transitions. Naturally, there is a range of laser intensities between the two extremes described here, where bound-bound, bound-free and free-free electron transitions are all important. A general theoretical analysis describing all interactions is beyond the scope of this work but simulations and experiments have led to empirical relations being formed [79].

2.3.2 Shocks

Laser-produced shock waves are generally caused by high intensity, long pulse lasers. The coronal plasma produced in such an interaction continues to be heated and expand. This expansion causes a reaction force on the target, creating a shock wave that propagates through the target away from the front surface. Lasers with shorter pulse lengths do not generally produce shock waves because the time during which the coronal plasma is heated and expands, is much shorter, leading to a much weaker reaction force on the target and hence a much weaker shock wave (or indeed none at all).

Although in this work we will only discuss laser-produced shocks as a method of creating a high energy density state of matter, other techniques, such as gas guns [80, 81] or pulsed power machines [82] have also been employed in recent years.

In order to describe this process, we first consider a plasma at rest in an infinitely long cylinder. At the left hand edge, we place a piston, representing the reaction force caused by the expansion of the coronal plasma in the laser interaction. At time, t_0, there is no plasma to the left of this piston, whereas to the right, the plasma is at rest. We now move the piston to the right, driving a compression wave in the plasma, propagating to the right at the plasma sound speed, c_s. The particles at and near the piston are also set into motion at the velocity of the piston, u_p. Additionally, the piston does work on the plasma, and hence both the kinetic energy and the internal energy of the plasma increase. Thus, at some time, t later, the piston is at the position, $x_p = x_0 + u_p t$ and the compression wavefront is at the position, $x_s = x_0 + c_s t$. There are now two regions within the plasma. The area to the right of the compression wave remains at rest and undisturbed, whereas the plasma between the piston and the wavefront is moving to the right and has a density, pressure and specific energy greater that that of the undisturbed plasma, as shown in figure 2.3

We now increase the speed of the piston with time, causing the speed of the resultant compression wave to increase as well. After some time, the later compression waves catch up to the earlier ones, causing a pile up effect, along with a narrowing of the region over which the thermodynamic variables change from the undisturbed state to the compressed state. As this region approaches zero, such that there is a discontinuity over these variables, a shock is formed.

The relationship between the material before and after the shock can be described

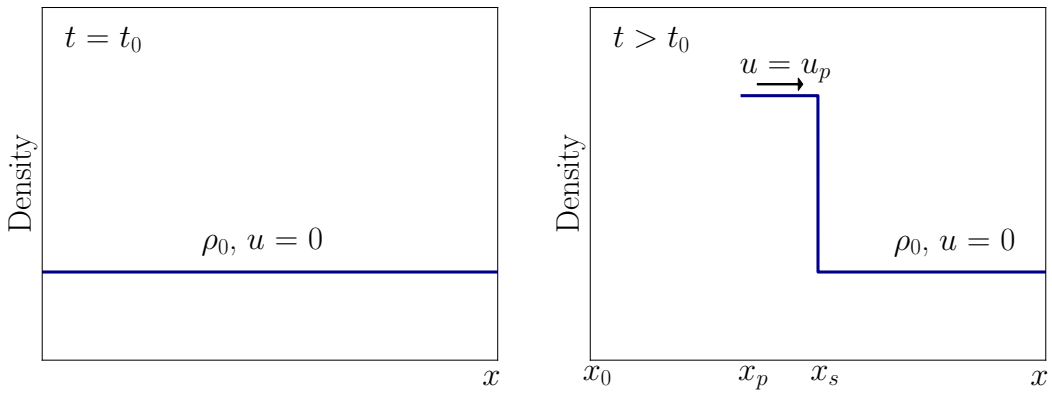

Figure 2.3: Two density profiles at t_0 and some time, t, later, in a 1-D plasma, with a compression driven by a piston of constant velocity from left to right.

by a set of equations known as the Rankine-Hugoniot relations. These equations are derived by considering mass, momentum and energy conservation across the shock front. They can be written as,

$$\rho_1 u_1 = \rho_0 u_0 \quad , \tag{2.30}$$

$$P_1 + \rho_1 u_1^2 = P_0 + \rho_0 u_0^2 \quad , \tag{2.31}$$

and

$$\epsilon_1 + \frac{P_1}{\rho_1} + \frac{u_1^2}{2} = \epsilon_0 + \frac{P_0}{\rho_0} + \frac{u_0^2}{2} \quad . \tag{2.32}$$

Together, they link the four flow variables behind the shock discontinuity - speed, u_1, density, ρ_1, pressure, P_1, and specific internal energy, ϵ_1 to those in front of it - u_0, ρ_0, P_0, ϵ_0. In order to close these relations, the functional form of ϵ_0 and ϵ_1, in terms of pressure and density, must be known. This is often referred to as the equation of state (EOS) of the material. Although there are many different prescriptions for the EOS, ranging from the simple ideal gas law to more sophisticated models such as the one proposed by Rose and Vinet [83], there is no complete analytical model

that applies under all conditions. Thus, there has been a great deal of work carried out in finding this functional form for different materials under varying conditions, especially in the WDM regime [14, 84, 85, 86].

In experiments, rather than having the front surface of the target open, such that the target is free to expand, a transparent material is sometimes used to confine the expanding plasma. This technique, known as adding an ablator or tamper to the target, typically allows the sample to reach higher pressures so is often preferable to leaving the target free to expand (see e.g. ref [87] for more details).

2.3.3 Laser-produced X-rays

The need for X-rays to probe high density plasmas rather than optical light should be obvious from equation 2.25: the critical density, above which electromagnetic waves cannot propagate through the medium, is inversely proportional to the wavelength. Therefore, X-rays can often penetrate sufficiently far into a sample when optical light cannot.

As introduced in section 1.2.2, the interaction of an intense laser beam with matter generates a large amount of X-rays, which can be used to probe the sample under investigation. The type of X-ray radiation produced is caused by a different process, depending on the pulse length of the incident laser. The interaction of a long pulse laser with a target creates a hot coronal plasma as shown in figure 2.2. This plasma is in a highly ionised state and, in particular, will contain many He-like ions. These ions spontaneously emit X-ray radiation from the 2p-1s electronic transition very efficiently, producing a significant amount of X-rays at a given wavelength. This type of line radiation is known as He-α radiation. While this technique is indeed quite efficient (around 0.1% of laser energy converted into X-ray radiation), it has several

drawbacks. The long pulse length of the laser means that studying any processes that happen on sub-nanosecond timescales is not possible. Additionally, the X-rays produced have a relatively large bandwidth and the spectrum may contain several other peaks relating to different electronic transitions.

The interaction of a short pulse laser with a target sets up a different process that also generates X-ray line radiation. The incident laser pulse causes a high intensity beam of electrons to travel at relativistic speeds into the target. As they travel through the target, inner shell electrons are collisionally excited. This leaves vacancies in the inner shells, leaving electrons from higher orbitals to drop down in energy levels to fill the shells. This process causes the emission of characteristic K-α radiation. This method has several advantages over He-α radiation in that it has a much shorter pulse length (around the order of the laser pulse length) and the spectrum is typically cleaner, with fewer satellite peaks. However there are also several disadvantages, the primary being that the conversion of optical light to X-ray radiation in this process is quite low (around 0.01%), added to the fact that short pulse laser systems generally have lower energy than their long pulse counterparts.

The two techniques also have several properties in common: they are both relatively simple to setup and carry out and the fact that they are both laser produced means that they work well in typical HEDP experiments where the sample to be studied is also laser produced. The main disadvantage, however, is that this type of X-ray radiation is a divergent rather than a collimated source, thus requiring detectors be placed very close to the laser-target interaction. This often creates signal-to-noise problems, given the amount of blackbody emission and fast electrons generated by high-intensity optical lasers. This drawback is addressed in detail in chapter 4.

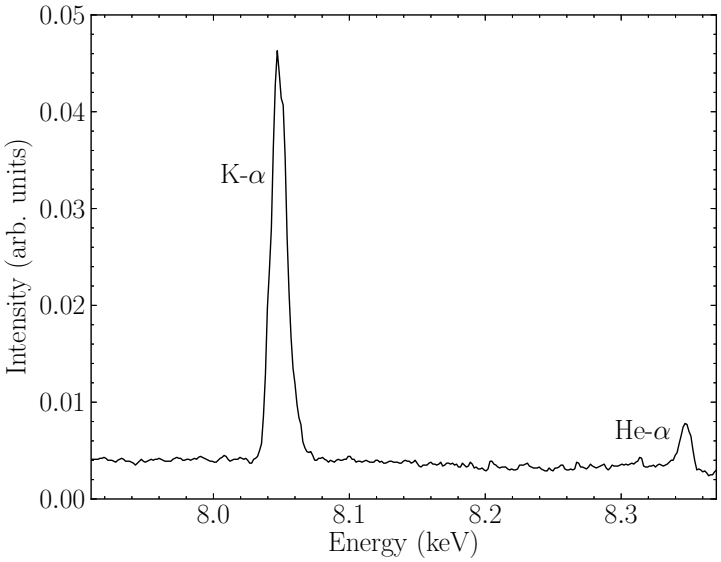

Figure 2.4: Example X-ray spectrum produced by the interaction of a high intensity, short pulse laser beam with a copper target.

Experiments involving laser-produced X-ray sources have had great success in recent years and they are now routinely used in HEDP experiments. Recent applications include measuring the compression and heating of shock-compressed matter [88, 89]; measurement of electron-ion temperature equilibration rates [59, 90]; and the observation of plasmons in warm dense matter [91]. Naturally, in any given experiment, one may observe both He-α and K-α radiation in the same X-ray spectrum, with the relative intensity of the peaks dependent on the laser pulse length. A typical spectrum is shown in figure 2.4.

2.4 Free-electron lasers

Another common method of X-ray radiation generation is based on particle accelerator technology. This thesis includes work carried out at so-called fourth generation light sources, known as free-electron lasers (FELs) and so this section will briefly outline the basic physical concepts behind their operation.

Despite their name, FELs are not, in the normal sense of the word, lasers. The beam does not draw energy from some gain medium and the method of stimulated emission is radically different to that used in optical lasers. The first part of an FEL consists of a particle accelerator that brings bunches of electrons to very high energies at nearly the speed of light. The electrons then pass through a periodic array of magnets with alternating poles, producing a side to side magnetic field across the beam path. This arrangement of magnets is called an undulator or wiggler, as the electrons are forced to follow a sinusoidal path due to the magnetic field produced. The electrons' acceleration along this path results in the release of photons (synchrotron radiation), which are monochromatic but incoherent. If this synchrotron radiation reaches a sufficient intensity, the transverse electric field of the radiation beam begins to interact with the transverse electron current created by the sinusoidal undulator motion, causing some electrons to gain or lose energy to the optical field. This energy modulation evolves into electron density modulations and thus the electrons become clumped into microbunches, with a spacing of one wavelength. The radiation emitted by these bunched electrons is now in phase, and so the fields are added together coherently. Further microbunching of the electrons occurs as the FEL radiation intensity increases. Eventually the electrons become completely microbunched, and the radiation reaches a saturated power several orders of magnitude higher than that of the undulator radiation [92].

An important measure of the usefulness of any X-ray source is its brilliance; a measure of the number of photons within a given spectral range, per second, per angular divergence, per cross sectional area. A higher brilliance means that a higher number of photons can be focused onto a single spot in a given amount of time. Figure 2.5 shows the brilliance of several X-ray sources worldwide today. The difference in brilliance between the newer free-electron lasers XFEL, LCLS and FLASH and the older

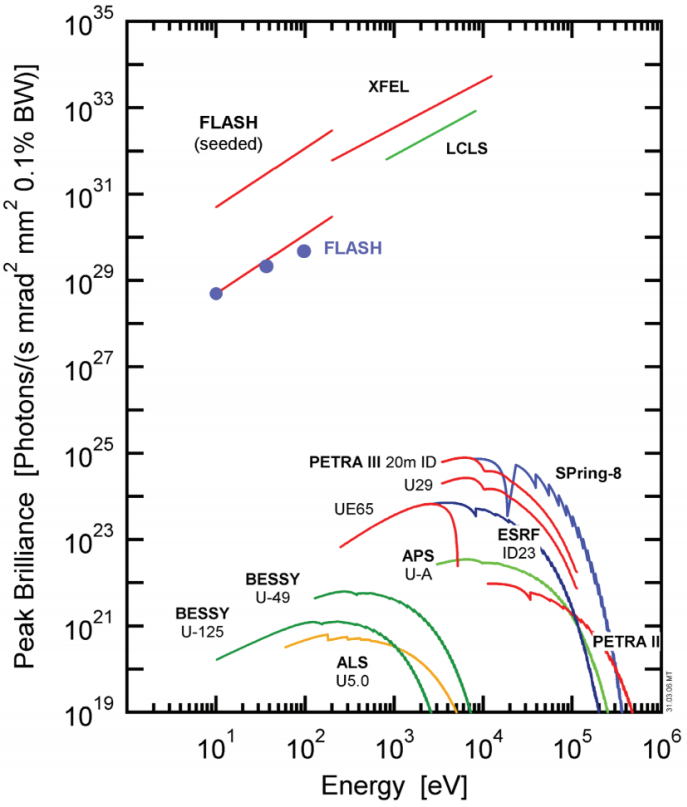

Figure 2.5: Comparison of peak brilliance of various X-ray sources worldwide (both free electron lasers and synchrotrons) as a function of photon energy (Reproduced from ref [93]).

synchrotron machines such as ESRF, PETRA III or SPring-8 is striking.

The radiation produced by free-electron lasers compared to laser produced X-ray sources is without doubt superior in many regards including bandwidth, brilliance and tunability. However, the amount of time, money, and space needed to construct these facilities is immense; at the time of writing, there are only a handful of such machines worldwide. On the other hand, conventional laser systems, ranging from table-top machines to large-scale national facilities, are widely available, and hence laser-produced X-ray sources will, for the foreseeable future, remain in widespread use due to their greater accessibility.

2.5 X-ray scattering

This section focuses on the fundamental theory of X-ray Thomson scattering (XRTS); a crucial diagnostic that has been used for many of the experiments reported on in this thesis. Figure 2.6 shows a simple schematic illustrating the relevant quantities in a typical scattering event. A beam of X-rays, with energy E_i and wavevector k_i, incident on a target, is scattered by an angle θ_s, changing its direction (wavevector) and energy to k_f and E_f respectively. The scattering process is therefore associated with some transfer of energy and momentum. This is given by,

$$E = \hbar\omega = E_f - E_i \ , \tag{2.33}$$

for the energy and

$$\hbar\mathbf{k} = \hbar(\mathbf{k_f} - \mathbf{k_i}) \ , \tag{2.34}$$

for the momentum [94]. In this work, we will solely consider the non-relativistic case, (the energy transfer being less than the photon energy), in which one can relate the momentum transfer to the scattering angle by the relation,

$$\hbar\mathbf{k} = 2\mathbf{k_i}\sin(\theta_s/2) \ . \tag{2.35}$$

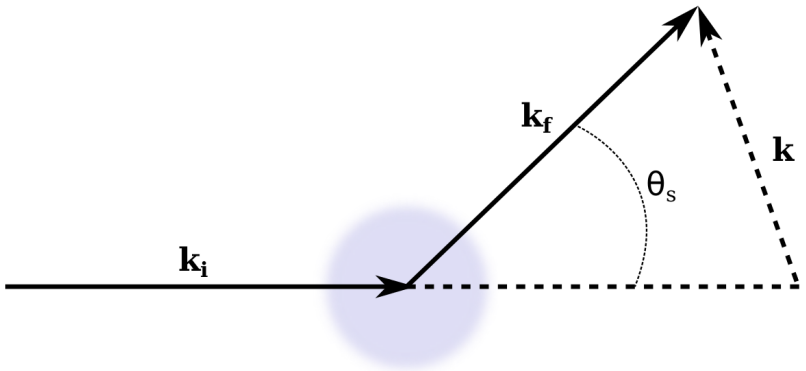

Figure 2.6: Simple diagram showing a typical X-ray scattering event.

Scattering events happen when an electron is accelerated by the electric field of an incoming photon. This causes it to oscillate back and forth and therefore emit light, with approximately the same energy. If the frequency of this incoming photon is much greater than any characteristic resonant frequencies of the electron in the atom, then the scattering cross section, σ_T, per unit solid angle, Ω, can be written as,

$$\frac{d\sigma_T}{d\Omega} = \left(\frac{e^2}{4\pi\epsilon_0 m_e c^2}\right)^2 \frac{1+\cos^2\theta_s}{2} \quad . \tag{2.36}$$

The value of the Thomson cross section is obtained by integrating over the solid angle,

$$\begin{aligned} \sigma_T &= \frac{8\pi}{3}\left(\frac{e^2}{4\pi\epsilon_0 m_e c^2}\right)^2 \\ &= 6.652... \times 10^{-25} \text{ cm}^2 \quad . \end{aligned} \tag{2.37}$$

The low value of this cross-section explains why the signal obtained in X-ray scattering experiments is typically very low and hence why there is currently a great deal of research being done on improving available X-ray sources.

2.5.1 Scattering from solids

We now consider the scattering of high energy X-rays (often called hard X-rays) from solids. The simplest case is that of a perfect single crystal, where the atoms are arranged into a periodic lattice. Here, the scattering from the electrons that are bound to the atoms, will interfere constructively at particular angular displacements, thus giving a very strong scattered signal. The simplest way of writing the criterion for constructive interference is that the path difference between the scattered light from one layer of a crystal, and that of the next layer, is,

$$n\lambda = 2d\sin(\theta_B) \quad , \tag{2.38}$$

where d denotes the lattice separation, λ the wavelength of the incoming X-rays and n the order of the diffraction. This formula is the well known Bragg's Law, with θ_B

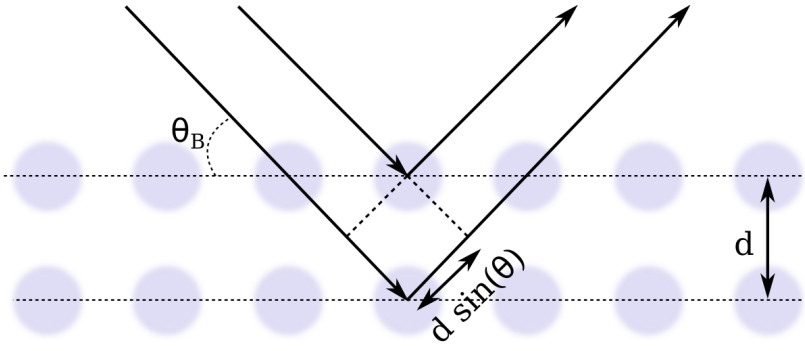

Figure 2.7: Simple representation of Bragg diffraction. For the scattered rays to interfere coherently, the paths must satisfy the Bragg relation.

being the Bragg angle [43]. Figure 2.7 illustrates this setup for a simple cubic lattice structure. Bragg's law provides yet another reason why X-rays rather than optical light are necessary for probing dense systems. For a given d spacing, the presence of the sin function means that the equation places an upper bound on the incoming photon wavelength; too long and there cannot be any constructive interference. Whereas the Bragg approach describes real space, it is the von Laue approach that is appropriate for reciprocal space [95]. The diffraction pattern from a crystal sample can be interpreted simply as a direct image of the underlying reciprocal lattice, and whilst this section has focused on solids, this result is in fact far more general and also applies to liquids or plasmas. A rigorous derivation of the Laue approach is not described here but can be found in ref [96] if the reader desires additional information. The conditions set out by Laue reduce to Bragg's law and so the two approaches are equivalent. In practice, the spatial extent of the crystal lattice and thermal vibrations both have an effect on the diffraction pattern, slightly complicating the simple picture outlined here. Several experiments have used exploited this fact to extract information about the system. For example ref [90] used the Doppler broadening of diffraction peaks to extract the temperature of the carbon ions in a graphite lattice.

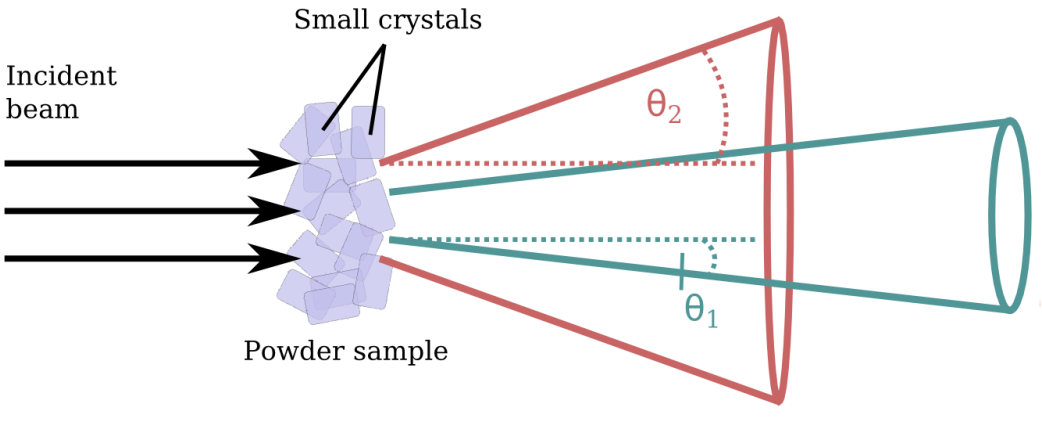

Figure 2.8: Schematic of powder diffraction. For a perfect powder sample, where the crystallite size is negligible compared to the target thickness, one observes a diffraction cone with a characteristic angle, θ, dependent on the lattice spacing.

2.5.2 Powder samples

Targets used in laser experiments are sometimes not perfect crystals, but rather powder samples, consisting of a large number of very small crystals. In the ideal case, these crystals are small compared to the bulk sample size and are completely randomly orientated. For any given lattice spacing between planes, d, there are many crystals oriented in such a way that their planes make the correct Bragg angle with the incident X-ray beam. The correctly oriented crystals have all possible orientations about the incident beam, hence the diffracted beams form a cone of half apex angle 2θ around the incident beam. For each different lattice spacing, d, there is a separate cone of angle 2θ. This is shown in figure 2.8. One therefore observes a ring, rather than a single point, on the detector, often known as a Debye-Scherrer ring. For samples that are not a perfect powder; that is the individual small crystals are not negligible in size to the bulk sample, or their orientation is in some way ordered rather than completely random, one observes a broken diffraction cone, where some possible crystal orientations are not present. The observed diffraction pattern from compressed, textured samples is rather complicated [97, 98] and will not be discussed here.

2.5.3 Scattering from liquids and plasmas

The dynamic and static structure factors of a system were introduced in section 2.2, primarily as a useful measurement from statistic mechanics that has important links to the thermodynamic properties of a system. These structure factors, however, are nothing other than the Fourier transform of the particle density within a system. Therefore, the intensity of photons scattered from a sample, I, can be related to the structure factor of that sample by the simple formula,

$$I \propto S(\mathbf{k}) \quad . \tag{2.39}$$

This can be written more generally as,

$$P_s(\mathbf{R}, \omega) d\Omega d\omega \propto \frac{P_0}{A} S_{ee}(\mathbf{k}, \omega) d\omega \quad , \tag{2.40}$$

for radiation measured at a position R, where ω is the frequency shift of the scattered photon, Ω is the solid angle, P_0 is the incident power and A is the inverse irradiated area.

Formally integrating this expression over all values of ω shows that the static structure factor is proportional to the scattered signal, for all systems. Therefore, in scattering experiments, one can easily measure the static structure factor for the system of interest when one does not attempt to energy resolve the scattered radiation [99, 100].

It should be noted here that the structure factor discussed here is the *electron-electron* structure factor (i.e. describing correlations between electrons). This due to the fact that the strength of scattering from a particle is inversely proportional to its mass, and so in this regard, the effect of the ions can be ignored. There appears to be some confusion then, as we had previously stated that the scattering pattern of solid is determined by its lattice structure (i.e. the ion-ion structure factor). This ap-

parent paradox is explained by the Chihara approximation, which decomposes the electron-electron structure factor into three separate terms [101, 102],

$$S_{ee}(k,\omega) = \mid f_1(k) + q(k) \mid^2 S_{ii}(k,\omega) \; + \; Z^* S^0_{ee}(k,\omega) \\ + \; Z_b \int S_{ce}(k,\omega-\omega') S_S(k,\omega') d\omega' \, . \tag{2.41}$$

The first term here describes electrons that are either bound or dynamically follow the ions' movement. Scattering from these electrons typically involves bound-bound transitions and hence is dominant in low temperature or weakly ionised systems. This explains the statements above: although the scattered radiation is proportional to the electron-electron structure factor, it is the ionic positions and the ion-ion structure factor, S_{ii} that determines the scattering pattern at low frequencies. This term also consists of the form factor, $f(k)$, which describes the reciprocal positions of the bound electrons around the nucleus, and the screening factor $q(k)$, which describes the effect of the screening cloud.

The second term consists of the dynamic structure factor of free electrons in the system, S^0_{ee}, multiplied by the factor Z^*, the average ionisation state of the ions in the system. The main features of this structure factor are high-frequency collective oscillations, known as plasmons.

The final term describes transitions between bound states and the free electrons; the term Z_b being the average number of electrons bound to each ion. This term is often ignored in XRTS experiments, as it is typically (but not always) much smaller than the first two terms [104]. It can roughly be thought of as electron-hole pair creation by the incident X-ray photons. In much denser plasmas, and, in particular, systems with heavier ions, this term might become more significant as it depends on the extent of continuum lowering within the system. This phenomenon, has been

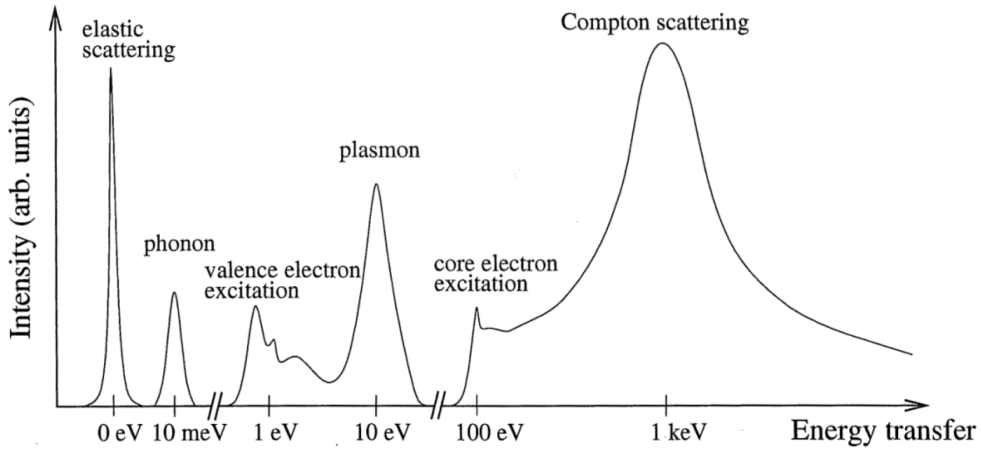

Figure 2.9: Inelastic scattering processes possible with interactions of X-rays and matter, along with the typical energy scales associated with them, reproduced from ref [103].

studied theoretically and although it is not yet fully understood, recent X-ray experiments have been able to measure its effect [105, 106].

Calculations invoking the Chihara approximation have shown good agreement with experimental scattering data in recent years [91, 104, 107, 108]. Nevertheless, the distinction between bound and free electrons in WDM is sometimes unclear and hence there is some interest in going beyond this approximation in order to predict scattering results [109]. Currently, only very small simulations are possible when not employing this decomposition, with initial results not suggesting large deviations from previous calculations [110].

We have been assuming scattering to be an entirely elastic process up to this point. Equation 2.41, however, describes terms related to inelastic scattering processes, where the X-ray photon either gains or loses energy. Figure 2.9 shows the range of inelastic scattering processes possible in X-ray-matter interactions, together with their characteristic energy. By energy resolving the radiation spectrum scattered from

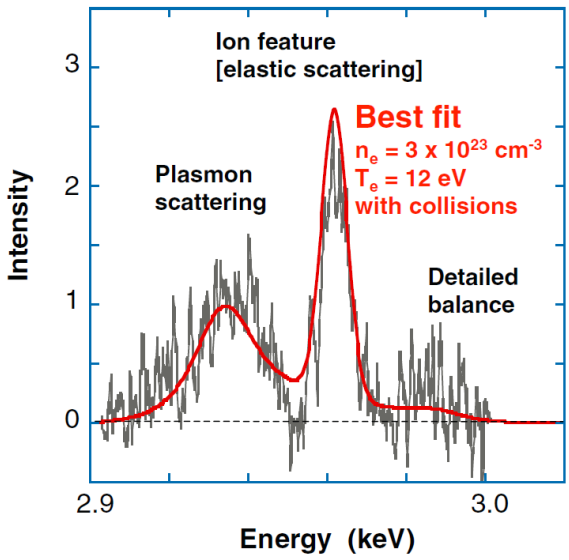

Figure 2.10: X-ray Thomson scattering spectrum showing the upshifted and downshifted plasmon peaks, with the latter being favoured due to detailed balance. The energy resolution in this experiment was too low to detect splitting due to bound electrons. Reproduced from ref [91].

the sample, one can determine both the structure and dynamics of the system. This is simply a restatement of equation 2.40, which states that the scattered radiation at a given position is proportional to the total electron-electron structure factor. An example of this type of spectrum is given in figure 2.10, which shows the first observation of plasmons in the warm dense matter regime. The incident photon energy in this case is 2.96 keV and hence the pronounced central peak corresponds to elastic scattering, with the broadening caused by thermal fluctuations. The two smaller side peaks are due to interactions with collective free electron oscillations (the second term in equation 2.41). Here, the downshifted peak is much stronger than the upshifted one as the photons are far more likely to lose energy to the electrons than they are to gain it. The ratio of these peaks is a function of the plasma parameters, often called the principle of detailed balance.

One should also expect to see splitting corresponding to scattering from bound elec-

trons, also called phonons, ion acoustic waves or ion modes (the first term in equation 2.41) in this spectrum [111]. Their characteristic energy, however, is several orders of magnitude lower than plasmons as shown in figure 2.9. In this particular experiment, the energy resolution was not high enough to detect this splitting and hence the broad middle peak around the incident X-ray photon energy. Chapter 5 looks at modelling the ionic motion and calculating $S_{ii}(k, \omega)$ from simulations, while chapter 6 will concentrate on the difficulty of measuring these small energy shifts experimentally.

Finally, one often separates the scattering from a system into a coherent and an incoherent part. This distinguishes between collective scattering and scattering from single particles. This separation is related to section 2.2, where the density-density correlation function was itself split into the self correlation and the pair correlation terms. A comparison of the length scale associated with the system, the Wigner-Seitz radius, a, and the wavenumber of the probe X-ray beam, k, can be used to estimate the relative importance of these two terms to the scattering process. Single-particle processes like Compton scattering become important for $ka > 1$, while the collective effects of plasmons and phonons dominate when $ka < 1$.

XRTS is used today to provide an accurate, non-invasive characterization of high energy density plasmas, including the measurement of temperature, density and average ionisation state [104, 107, 108]. It also represents one means of directly measuring the dynamic structure factor of a system, thus giving a complete picture of the structure and dynamics of both the electrons and ions.

2.6 Molecular dynamics

The term molecular dynamics (MD) refers to a computer simulation method for solving the equations of motions that describe the microscopic behaviour of particles such as atoms, molecules or ions, within a given system. Recent technological advances in computer hardware, together with the development of massively parallel MD software, has meant that systems with a huge number of particles may now be simulated [112]. Although it started out in the domain of theoretical physics, MD is now also used throughout the field, as well as in chemistry and biology, to simulate systems of gases [113], liquids [114], solids [115], surfaces [116], clusters [117], and, most recently, plasmas [72, 118]. As it is not possible to describe such complex systems with analytical methods, MD has become a very important and widely used tool. MD is used in this work in chapter 3 to model the interaction of a short pulse laser with a gold target and in chapter 5 to calculate the structure factors of a warm dense aluminium plasma.

2.6.1 Particle trajectories

An MD simulation consists of solving the Newtonian equations of motion for a given number of particles with defined masses and a given interaction potential between particles. For an N-body system, with masses, m_i, the equations of motion can be written as,

$$\begin{aligned} m_i \, \ddot{\mathbf{r}}_\mathbf{i} \; &= \; \mathbf{F}_\mathbf{i} \left(t \right) \;\; , \\ i &= \{1 \; ... \; N\} \;\; , \end{aligned} \tag{2.42}$$

with the force dependent on the positions of all the other particles in the system and given by,

$$\mathbf{F}_\mathbf{i} \left(t \right) = -\nabla_i \sum_{i \neq j}^{N} v \left(r_{ij} \right) \;\; , \tag{2.43}$$

where $v(r_{ij})$ is the interaction potential between the ith and jth particles. The basis for the simulation is very simple: first, a set of initial conditions are defined and the subsequent forces on the particles are calculated using equations 2.42 and 2.43. The particle positions are then evolved, causing the force on them on to change. Hence, the process of calculating forces and evolving positions continues until some set end-point is reached.

To evolve the particle positions computationally, a discretised form of equation 2.42 must be solved iteratively with an integration algorithm. The simplest possible example of this is the Euler method,

$$\begin{aligned} \mathbf{r_i}(t+\Delta t) &= \mathbf{r_i}(t) + \mathbf{v_i}(t)\Delta t \\ \mathbf{v_i}(t+\Delta t) &= \mathbf{v_i}(t) + \frac{\mathbf{F_i}(t)}{m}\Delta t \quad . \end{aligned} \tag{2.44}$$

This a first order method which means that while the algorithm is incredibly simple, the associated error scales with Δt, rendering it completely unsuitable for large-scale simulations with large numbers of timesteps. The leapfrog method, a second order method, represents a significant improvement, with the error scaling as $(\Delta t)^2$. It is given by,

$$\begin{aligned} \mathbf{r_i}(t) &= \mathbf{r_i}(t+\Delta t) + \mathbf{v_i}(t-\Delta t/2)\Delta t \\ \mathbf{v_i}(t+\Delta t/2) &= \mathbf{v_i}(t-\Delta t/2) + \frac{\mathbf{F_i}(t)}{m}\Delta t \quad . \end{aligned} \tag{2.45}$$

This is still not accurate enough for our needs and is more suited to oscillatory simulations. By considering a Taylor expansion forwards and backwards in time around the particle position, we obtain,

$$\begin{aligned} \mathbf{r_i}(t+\Delta t) &= \mathbf{r_i}(t) + \mathbf{v_i}(t)\Delta t + \frac{\mathbf{F_i}(t)}{2m}\Delta t^2 + \frac{\dddot{\mathbf{r}}_\mathbf{i}(t)}{3!}\Delta t^3 + \mathcal{O}(\Delta t^4) \\ \mathbf{r_i}(t-\Delta t) &= \mathbf{r_i}(t) - \mathbf{v_i}(t)\Delta t + \frac{\mathbf{F_i}(t)}{2m}\Delta t^2 - \frac{\dddot{\mathbf{r}}_\mathbf{i}(t)}{3!}\Delta t^3 + \mathcal{O}(\Delta t^4) \quad . \end{aligned} \tag{2.46}$$

Summing these two equations gives,

$$\mathbf{r_i}(t+\Delta t) \approx 2\mathbf{r_i}(t) - \mathbf{r_i}(t-\Delta t) + \frac{\mathbf{F_i}(t)}{m}\Delta t^2 \quad . \tag{2.47}$$

which is the Verlet algorithm [119]. The associated error is on the order of Δt^4, and hence this method is often used as a balance between speed of computation and fidelity to real systems. It is therefore this method that we use in this work. As this approach requires the particle positions at two time-steps, care must be taken when initialising the simulation. Here, we first allow the simulation to reach an equilibrium state before taking data, however, and hence this additional source of error is not important.

It is necessary at this stage to consider the choice of the timestep used in our simulations. One crucial requirement is that it is small enough such that the trajectories of the particles do not diverge from their true trajectory. Too large and they can travel a very large distance in a single timestep and therefore find themselves unphysically close to another particle. This causes a change in the potential and hence total energy of the system, which is strongly undesirable. Naturally the velocity of the particles determines how likely this situation is to happen and hence changing the temperature of a simulation often necessitates changing the timestep as well. On the other hand, the timestep must be large enough such that the simulation does not take too long to exhibit the physical process under investigation. This balance plays a crucial role in many large computer simulations and is important throughout this thesis. Typical timesteps used in this work are of the order of a femtosecond.

2.6.2 Ensembles and thermostats

While MD simulates the microscopic behaviour of individual particles within a system, one is typically most interested in extracting the macroscopic properties of the

system, such as pressure or the DSF, which can then be compared to experimental data. Thermodynamic properties are, however, an ensemble average over all the different microstates of the system. The weighting factor used to determine this average is dependent on the ensemble used. MD simulations simply applying Newton's equations of motion with a suitable integrator are a representation of the microcanonical or NVE ensemble, where the number of particles (N), the volume of the system (V) and the total energy (E) remain constant. This equates to averaging over all the microstates that have a total energy, E. Although initially, one might think that running a simulation in this ensemble is both obvious and necessary, it in fact makes for a poorer model in most cases. This is partly because many of the systems that are modelled using MD are not, in themselves, isolated systems. Instead they can exchange energy, and sometimes mass as well, with their surroundings. Consequently, a system at constant temperature, rather than energy, is frequently more appropriate. This is known as the canonical ensemble or NVT. Additionally, while the total energy is conserved, simulations that are run in NVE often exhibit a drift in temperature over time. As one is generally interested in determining the properties of a material at a given temperature, density, or pressure this often makes NVE an unsuitable choice. Experimentally, when the number of atoms is very large, the system is in the thermodynamic limit and the results from each of these ensembles can be shown to be equal. In practice, MD simulations approximate the NVT ensemble by applying a thermostat to keep the mean velocity constant, while running in the NVE ensemble. The simplest way to do this is by simple velocity scaling, where the velocities of each particle at each timestep are altered such that the temperature of the system is maintained at some value. This method is quite common, despite being unphysical and not-reproducing any statistical ensemble. More sophisticated methods of keeping a constant temperature include the Nosé-Hoover [120, 121], Gaussian [122] and Langevin [123] thermostats, which are designed to more formally approximate the

NVT ensemble. The relative merits of these approaches are discussed in detail in chapter 5.

2.6.3 Ergodicity

A typical MD simulation, will, after a sufficiently long time, reach some equilibrium macrostate. Quantities such as pressure or viscosity will reach some constant value and while they may fluctuate around this point, there is no downward or upward trend. If one then calculates a thermodynamic property from this simulation by averaging over different timesteps, each corresponding to a different microstate, one obtains a time average rather than the desired ensemble average. Over long periods of time, the time spent by a system in some region of the phase space of microstates with the same energy is proportional to the volume of this region. In other words, all accessible microstates of a particular system are equally as probable over a long period of time [124]. This is known as the Ergodic hypothesis and can be written formally as,

$$\langle ... \rangle = \lim_{t \to \infty} \frac{1}{t} \int_0^t ...dt \ , \tag{2.48}$$

with the left hand side representing the ensemble average and the right hand side the time average. While this hypothesis has never been rigorously proven, it is in widespread use in the field of computational physics [125, 126]. Strictly speaking, MD simulations can only ever produce an approximation of the ensemble average as the integral in equation 2.48 is in fact a summation over a discrete, finite number of timesteps, although a longer simulation with shorter timesteps naturally produces better results (and takes much more computational power). Typically, as is the case in this work, the results are checked for convergence with an increasing number of timesteps to assess their accuracy.

2.6.4 Finite simulation size

Extracting thermodynamic properties from MD simulations also often requires that one take the limit $N \to \infty$ in addition to $t \to \infty$. This is clearly impossible, and while computers today are able to simulate several cubic microns of material, this is nowhere near enough to avoid edge effects. Instead one typically employs periodic boundary conditions (PBCs) around a unit cell of reasonable size. The key idea here is that any particle that leaves the simulation cell at one side re-enters at the other, with the same velocity. If one also transmits forces between particles across the boundary, one, in effect, is able to simulate a system of infinite size. As was the case with simulations of a finite time, a convergence study must be performed to study the effects of increasing the spatial size of the simulation. A suitably large unit cell must then be chosen in order to produce accurate results.

2.6.5 Interatomic forces

The most significant source of error in MD simulations does not typically stem from the approximations described previously, but rather the potential used to describe the force between the particles. Most MD potentials are constructed in an empirical manner and frequently contain arbitrary fitting parameters used to match simulations to experiments [127]. An appropriate choice of potential is then crucial in obtaining high accuracy simulation results. In this work, we use three different methods to calculate the forces between atoms.

The first, and simplest type of potentials are pair-wise interactions, where the potential is a function only of the distance between two atoms [118]. One example of this type is the Yukawa potential as described by equation 2.2. This is rather simple, and a noticeable improvement is made by introducing a short range repulsion (SRR) term, with the total effective potential given by,

$$v(r) = \left(\frac{Z^{*2}e^2}{r} + \frac{(Z^2 - Z^{*2})e^2}{r} e^{-br} \right) e^{-\lambda_{TF} r} \quad , \tag{2.49}$$

where Z is the atomic number of the element in question and b is a parameter that represents the effect of increased nuclear repulsion when the bound electron charge clouds around each nucleus overlap. This parameter determines the effect of the short range repulsive term in the potential and in the limiting case of $b \to \infty$ one can easily show that this potential reduces to the simple Yukawa case. This type of potential is used in chapter 5 to model a dense aluminium plasma.

The second type of potential used in this work is based on the embedded atom model or EAM approach [128]. Here, the potential energy of each atom is a function of a sum of functions of the separation between an atom and its neighbors. This makes it a multibody rather than a simple pairwise potential like the Yukawa model. The main advantage EAM potentials have over pairwise ones is that they deal with bonding more accurately. Pairwise potentials tend to maximise the number of nearest neighbours whereas in reality this does not always happen. An EAM potential is used, in this work, in chapter 3 to model a crystalline gold structure.

One must also consider, however, that an MD simulation based on fully classical mechanics may not be able to accurately describe a system in the warm dense matter regime, where electron degeneracy plays a non-negligible role. Although solving the Schrödinger equation directly from first principles at every timestep is not practical, there are several methods of performing an MD simulation based on quantum mechanical methods. Path-integral Monte Carlo simulations have recently been employed to determine the thermodynamic properties of dense hydrogen [129], and water and carbon plasmas [130]. Bohm trajectories have also been suggested as a way to calculate forces quantum mechanically [131]. In this work, however, we focus on

density functional theory coupled with molecular dynamics (DFT-MD), a method which has become popular in the community, being used to simulate the conditions found in cores of large planets [132], calculate equations of state [133], describe phase transitions [134], and to benchmark theoretical other models [135]. DFT-MD is an approach which calculates the potential between the ions from first principles at every timestep of the simulation. This method therefore effectively removes the main source of error in classical MD simulations: the choice of the potential. The details of the method are left to chapter 5 where this method is used to calculate the dynamic structure factor a warm dense aluminium plasma.

Chapter 3

Temperature relaxation in laser-heated matter

This chapter details the experimental measurement of electron-ion coupling in a laser-illuminated gold sample. The relaxation rate is derived using state-of-the-art molecular dynamics simulations and compared to theoretical predictions as well as other experimental data. The experiment and subsequent analysis provide a proof-of-principal method of determining the relaxation rate of laser-heated solids using laser systems of modest size.

3.1 Introduction

In general, over a sufficiently short time-scale, a high energy density state of matter, produced in the laboratory will not necessarily be in thermal equilibrium. The various methods of heating a sample, be that an electron or proton beam or the direct interaction of an optical laser, will preferentially heat either the electron or the ion subsystem. The two subsystems then exchange energy in order to reach an equilibrium state. At the same time, states created experimentally are generally assumed to represent long-lived states, such as those found in celestial bodies [136, 137]. There-

fore it is absolutely necessary for the system to be allowed sufficient time to reach a thermal equilibrium before probing it. There is only limited experimental data for the timescale over which this relaxation occurs, meaning there is a possibility that results obtained from a system which is assumed to be in equilibrium, may well not be [60]. Subsequently, there has been recent interest in experimentally measuring temperature relaxation rates of various different types of systems, from laser-heated solids to strongly coupled plasmas [90, 138, 139, 140, 141]. However, the process is complex and indeed different data sets do not generally agree with each other [59, 138, 142]. While experiments near equilibrium show reasonable agreement with standard theoretical predictions [143, 144], other experiments, with high excitation densities or a more complex material structure, exhibit large deviations, with equilibration times far longer than predicted [59, 145]. Deviations such as these are somewhat expected for strongly heated, fluid systems [140, 146, 147, 148], where the energy transfer evolves through direct two-particle scattering or ion acoustic modes rather than electron-phonon coupling. And indeed, although theoretical models that include the collective behavior of such coupled systems do show similar effects, the predictions do not agree with the small amount of experimental data currently available [149, 150, 151].

The properties of these non-equilibrium systems are interesting in their own right. Subsequently, many theoretical and computational methods have been developed to model them [152, 153, 154]. Some show abnormal phase transition behaviour [155] and have significantly different thermodynamic [156] and electrical properties [140, 157] compared to equilibrium systems. The electron-phonon coupling may also determine or modify other properties, such as the magnetic susceptibility or the available electron energies, and thus, the equation of state [158]. Therefore, aside from gaining a more fundamental understanding of high energy density states of matter, this field has important consequences for laboratory astrophysics [139], material science [159],

nanotechnology [160], laser ablation [161] and inertial confinement fusion [162].

3.2 Two-temperature model

In this work, the energy relaxation behaviour has been described with the two-temperature model (TTM) [163]. This approach treats the electrons and ions as separate subsystems, linked only by an energy exchange term. It can be summarised by the coupled equations,

$$C_e \frac{\partial T_e}{\partial t} = \nabla \cdot (K_e \nabla T_e) - g(T_e - T_i) + S_e(\mathbf{r}, t) \ , \tag{3.1a}$$

$$C_i \frac{\partial T_i}{\partial t} = \nabla \cdot (K_i \nabla T_i) - g(T_e - T_i), \tag{3.1b}$$

where C_e (C_p) is the electron (phonon) specific heat capacity, K_e (K_p) is the electron (phonon) thermal conductivity and S_e is the source term due to the heating by the laser incident on the sample. The coupling constant, g, controls the evolution of the electron and ion temperatures, a complex process which depends on many factors such as initial temperatures, crystal structure, defects and the scattering properties of the sample [144, 164]. By using the TTM, the complexity of the system can be described by a single parameter. This approach assumes that the two subsystems are themselves in a local equilibrium, both having a well defined temperature. This implies that the particles have had a sufficient amount of time to exchange energy with each other and reach an equilibrium distribution (be that Maxwellian, Fermi-Dirac or Bose-Einstein etc) [165].

The use of this approach to model rapidly heated, out-of-equilibrium systems, such as laser-illuminated samples [166], has been common for some time now. Its use is not constrained to this method of heating, however [90, 138]. For example, it has been applied to the electron-phonon relaxation process during the high-energy ion bombardment of metal targets. In this case, the source term in equation 3.1a ac-

counts for the energy transfer between the incident energetic ions to the electronic excitations within the ion track [167, 168]. Various effects and physical processes that are not described by the standard TTM may still be included within its general framework. Among the most recent developments are the inclusion of the description of the surface/grain boundary scattering [169, 170] as well as the energy transfer by ballistic electrons [171]. The TTM has also been combined with thermoeleasticity [172] equations as well as extended to incorporate a description of the transient non-thermal electron dynamics immediately after ultra-short laser pulse excitation [173]. Furthermore, studies on the microscopic mechanisms of laser-induced phase transitions and changes in the microscopic structure of target materials have been enabled by the developments in hybrid models, where the TTM is combined with classical MD [174, 175, 176].

3.3 Measuring temperature relaxation

The most direct direct way of investigating electron-phonon coupling is to create a system that is out of equilibrium and to then observe its subsequent evolution towards a state with a common temperature. In order to measure the temperature relaxation rate of a material though, one must measure the temperature of either the electron

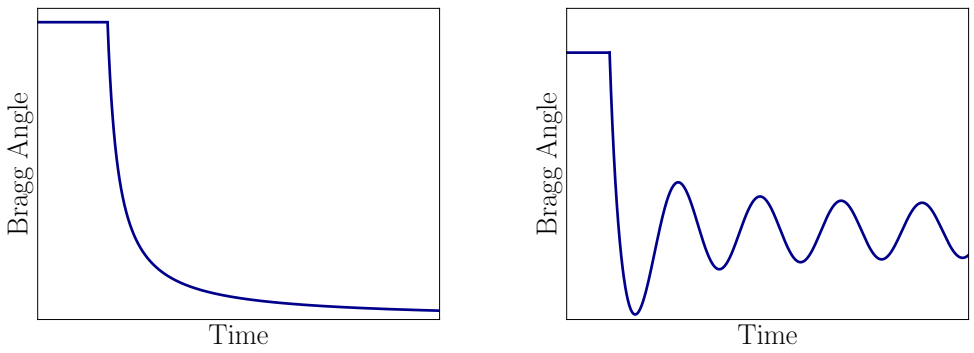

Figure 3.1: Evolution of predicted Bragg diffraction angle with time of single crystal, after being heated. Left hand panel: gradual heating. Right hand panel: fast heating.

or the ion subsystem within the sample. While this task is not straightforward for laser-heated systems, it is by no means impossible. The method preferred here is through the use of time-resolved X-ray diffraction. Section 2.2.1 introduced the idea that the diffraction pattern of a sample is proportional to its static structure factor, the Fourier transform of the atomic positions. Figure 2.1 showed that an infinitely large, perfect crystal leads to a set of distinct delta functions in the SSF, and hence the diffraction pattern. As the temperature of the crystal is increased, it begins to expand. Assuming an isotropic, volumetric expansion, one can write the thermal expansion coefficient, α, as,

$$\alpha = \frac{1}{V}\frac{dV}{dT} \quad , \tag{3.2}$$

where V is the volume of the material and $\frac{dV}{dT}$ is the rate of change of said volume with temperature. This expansion therefore causes the lattice spacing to increase and hence, from Bragg's Law, the resultant diffraction angle from photons of a given wavelength will decrease. The diffraction line is therefore translated spatially across the CCD chip, thus tracking the ionic temperature over time. Additionally, as the random motion of the ions increases with temperature, the intensity of the well-defined Bragg peaks drops; a phenomenon known as the Debye-Waller effect. Conversely the level of diffuse scattering increases. This does not affect the peak position, however, which is the main focus of the current work.

Depending on the rate at which the ions are heated, the crystal may respond in two distinct manners. The first corresponds to a gradual heating where the ions reach their equilibrium positions over a long period of time, after which the lattice constant remains the same. The second regime, corresponding to fast heating, is characterised by a rapid expansion of the crystal and subsequent oscillation around some new mean lattice constant [177]. The subsequent evolution of the Bragg angle

in the two regimes is displayed in figure 3.1, for an arbitrary crystal.

3.4 Temperature relaxation in gold

Here, we used the well-established procedure of the interaction of a short-pulse laser with a solid target to create a system that is out of equilibrium. The free electrons in the sample are excited by the laser pulse, creating an initial high temperature electron subsystem while the phonon subsystem remains cold [143]. The electron subsystem quickly thermalises [178] and energy then flows into the lattice through the excitation of phonons, and afterwards ion-acoustic waves, heating the background ions [143]. This process is relatively slow, meaning that the electrons and ions may be at different temperatures for times much greater than the laser pulse duration [59]. The electron and ion subsystems therefore cannot be represented by Fermi-Dirac distributions *with equal temperatures*.

3.4.1 Experimental details

Here, we describe an experiment that was carried out at the University of Oxford in the High Energy Density Physics laboratory. The experimental results presented here are the first obtained from the new table top Ti:sapphire laser. It is necessary to finely tune the laser alignment on a regular basis to maintain a high energy output, as well as a smooth beam profile. The laser was used in single shot mode throughout the experiment, with the pulse being split equally with a 50/50 beamsplitter. One arm was focused to a spot size of approximately 3 mm onto a 200 nm thick gold nanofoil in order to heat it, creating the out-of-equilibrium state. The goil foil used is commercially available from PHASIS (Switzerland). The gold foil was a single crystal, orientated with the (111) plane of the fcc lattic structure parallel to the target surface. Due to the very thin nature of the target, it was necessary for it to be grown onto a mica muscovite substrate in order to increase its rigidity. Although a

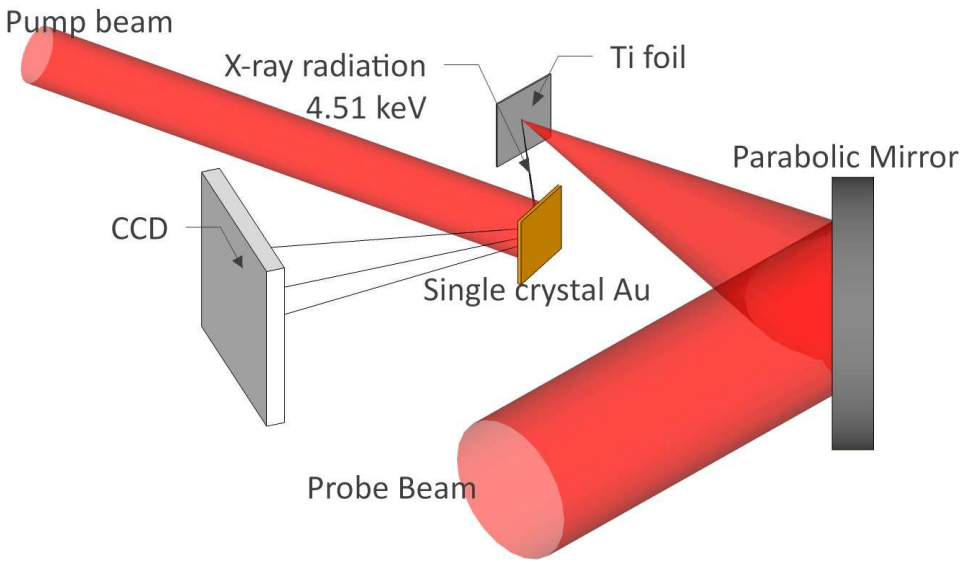

Figure 3.2: Schematic of experimental setup. The Ti:sapphire laser is split into two arms to achieve pump-probe geometry. The probe beam is focused onto a titanium foil to generate X-rays, while the pump beam is incident directly on the gold sample to create the desired out of equilibrium state.

pure target would, in theory, be preferable, such a target would be far too fragile and breakable to work with experimentally. The other arm of the laser was used to create X-rays, thus achieving pump-probe geometry. It was sent through a delay stage with a range of $\Delta t = 5$ to $\Delta t = 250$ ps, where negative values mean that the probe beam arrived at the target before the pump beam. The error in this timing was estimated to be $\pm$ 1 ps, which corresponds to an error of $\pm$ 0.3 mm on the delay stage. The probe beam was then focused by a f/10 parabola to a spot size of 50 µm onto a thin 12.5 µm Ti-foil to generate short-pulse line radiation at 4.51 keV. The pump beam was incident normal to the gold foil while the X-rays intercepted the sample at the Bragg angle ($\theta_B = 35.9°$). The X-rays incident on the gold sample and the pump laser spot were overlapped spatially, with the laser spot size (3 mm) much larger than the area of the sample exposed to X-rays ($<$ 1 mm), so as to ensure that no cold matter was probed during the experiment. Neither the X-ray target, nor the gold sample were destroyed in single shots, so multiple data points could be taken

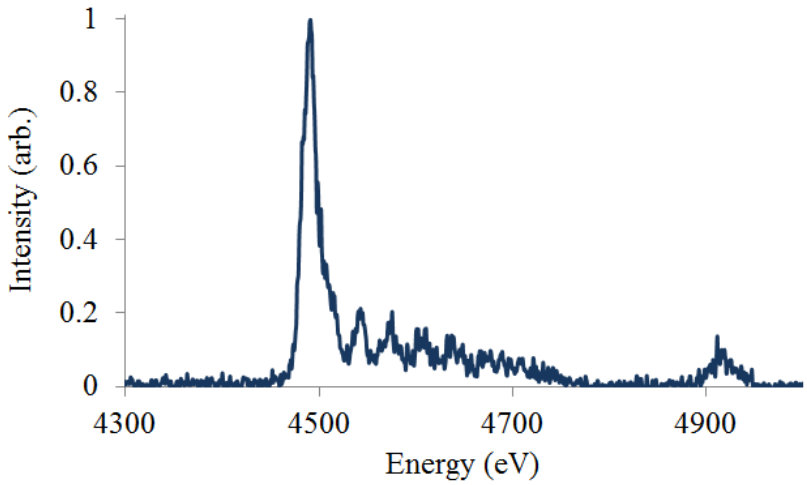

Figure 3.3: X-ray spectrum produced by interaction of short pulse-laser with titanium foil target, resolved by a highly-orientated pyrolytic graphite spectrometer. Ti K-α line is clearly present at 4.51 keV, in addition to several satellite peaks.

with one pump-down / let-up cycle of the vacuum chamber. The foils were relatively large compared with the laser spot sizes and hence by translating in the horizontal or vertical directions, around 8-10 shots were possible each time the vacuum chamber was sealed. A schematic of the experimental setup is shown in figure 3.2. The X-ray line radiation was scattered coherently from the gold nanofoil and imaged onto a 2 cm $\times$ 2 cm CCD chip, at a distance of 10 cm from the sample. As the diffraction angle, and hence the position of the line on the chip, is related to the lattice spacing of the gold through Bragg's law, the thermal expansion of the ions can be detected through translation of the diffraction line.

Prior to heating the sample, the first task was to characterise the probe beam and optimise the number of X-ray photons produced. The X-rays produced by the interaction of the laser with the titanium target were spectrally resolved using a highly-orientated pyrolytic graphite (HOPG) crystal and detected by a CCD. A typical spectrum is given by figure 3.3. The strongest peak, at 4.51 keV, corresponds to the characteristic titanium K-α line, arising from the 2p-1s transition, while the peak at

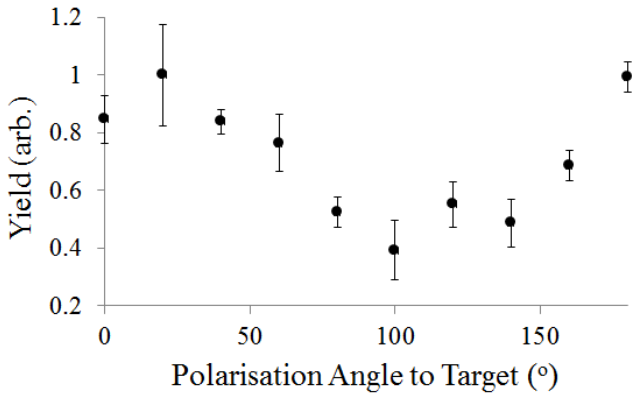

Figure 3.4: Integrated X-ray yield produced by interaction of short pulse-laser with titanium foil target, as a function of laser polarisation angle. Optimum yield is obtained with P-polarisation.

4.93 corresponds to the titanium K-β line, coming from the 3p-1s transition. There are also smaller satellite peaks between 4.5 keV and 4.7 keV arising from the 2p-1s transitions titanium ions containing different numbers of electrons. The highest energy of these comes from the helium-like ion, containing two electrons. The area under this spectrum is related to the X-ray yield and can be plotted against the laser parameters in order to find the peak number of X-ray photons. This was done for the case of the laser polarisation, as shown in figure 3.4, with peaks found at around 0 and 180 °, corresponding to P-polarisation. The observation of a peak at these angles may be due to two processes: The first is an enhanced laser energy absorption fraction for P-polarisation compared with the S-polarisation, possibly with more efficient resonance absorption. The second is that, the electric field direction associated with P-polarisation causes electrons to move in and out of the target surface, rather than parallel to it, as is the case with S-polarisation. As a result, more fast electrons may be generated, enhancing excitation and ionisation rates and hence increasing the X-ray yield. The laser parameters chosen for this work were: a wavelength, λ centered at 800 nm, with a pulse duration of 50 fs, an average energy per pulse of 40 mJ and a P-polarisation state.

Taking account of the 50/50 beamsplitter, the laser fluence incident on the gold sample was calculated to be 0.28 J cm^{-2}. After multiplying by the reflectivity of gold at 800 nm, we calculated the energy flux on the target to be $\sim$ 0.01 J cm^{-2}. This corresponds to an overall increase in the energy of the sample to be $\sim$ 1 eV nm^{-3}. The thin gold foil was mounted onto a mica substrate on the side opposite to the laser beam, whereas the laser-facing side of the gold film was open to the vacuum and could expand freely.

For each delay time, multiple shots were taken and added together in order to give a reasonable diffraction signal. A Gaussian was fitted to the middle portion of a lineout of the diffraction line using a least squares fit. The position of the centre of this Gaussian was used as the diffraction peak position for each delay time and hence used to calculate the diffraction angle. Although a radial lineout over the whole diffraction line would be expected to give better results than simply using the central portion, this was not found to be the case here. Possible reasons for this could be due to the anisotropy of the X-ray source or deviations from a perfect crystal in the gold sample, which could both cause intensity variations along the length of the diffraction line. To ensure the gradient of the initial expansion was determined with a high precision, for delays between -5 ps and 40 ps the conditions were repeated 12 times and for all other delays, 6 shots were used. Error bars were estimated using one standard deviation from the mean. Figure 3.5 shows the diffraction signal on the CCD chip both before and after laser irradiation. The curvature of the diffraction line is caused by the geometry of the experimental setup. Because the X-ray source is divergent and the gold sample is a single crystal, the Bragg condition is satisfied by photons that are incident on the gold foil at different locations, with the resultant shape being an arc, which is seen by the CCD chip. The translation of this arc in the vertical direction is of the same order as its width ($\sim$ 50 µm). The shift is therefore

large enough to be measured with a reasonable degree of accuracy. Improvements could be made by attempting to reduce the width of the diffraction peak, for example by decreasing the divergence of the X-ray source. This would decrease the overall number of photons available, however, which would in turn increase the error due to lack of signal. It is also worth noting that the noise levels on both images are similar. This is due to the fact that the drive beam has a very low intensity due to its large focal spot, whereas the probe beam is tightly focused. Almost all of the background X-rays are therefore created by the probe beam's interaction with the titanium foil. Additionally, the weak laser drive means that the temperature of the lattice does not increase by a large amount and hence the diffraction peak does not decrease significantly in intensity. Also shown in figure 3.5 is the experimentally obtained change in diffraction angle as a function of time, including standard deviation in the error bars. Note the qualitative behaviour follows that predicted in figure 3.1, as would be expected with a fast laser heating method [177].

3.5 Modelling the lattice dynamics

This work differs from previous experiments, where a similar experimental technique was employed, through the utilisation of large-scale non-equilibrium molecular dynamics simulations to analyse the lattice response, and ultimately to determine the electron-ion coupling parameter, g. MD is a powerful tool that has had significant success in modelling lattice dynamics in numerous laser-solid interactions [179, 180, 181]. The simulations here contain up to $\sim$ 300 000 atoms and are able to model the full depth of the gold foils. Being able to fully capture the acoustic modes of the system, MD is a method that is ideally suited to model systems with higher excitation densities than the ones presented here.

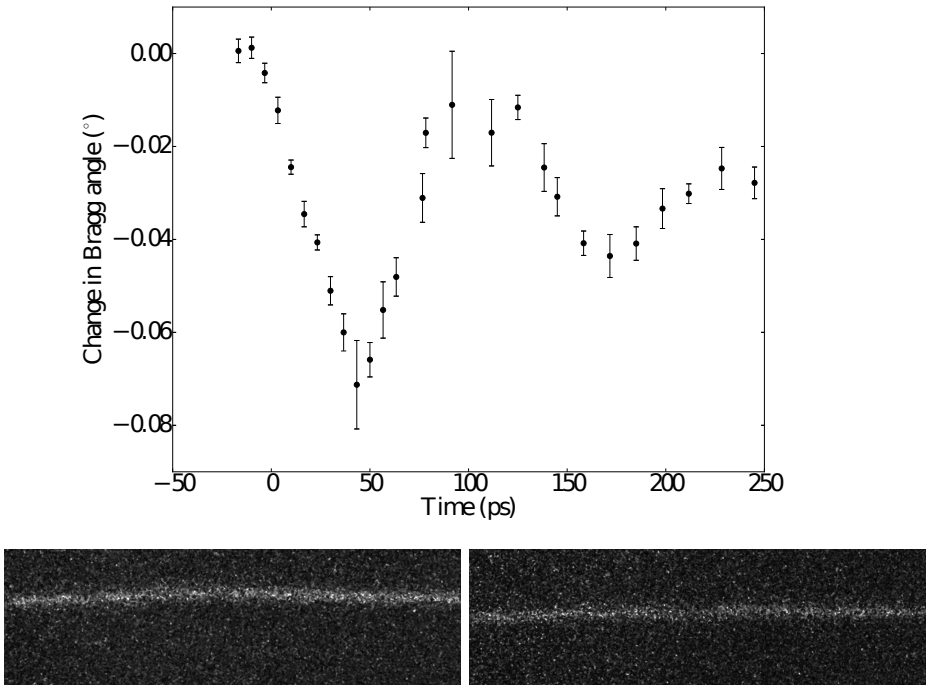

Figure 3.5: Top: Change in diffraction angle from the gold nanofoil plotted against delay time. The data have been shifted in time to approximate the position of $t = 0$ ps as this was unable to be measured experimentally. Bottom: Example images of diffraction line, as seen by the CCD chip. Both images are the sum of 12 individual shots at two different delay times. Left: Probe beam arrives 5 ps before laser heating. Right: Probe beam arrives 40 ps after heating.

3.5.1 Employing the two-temperature model

The validity of the TTM must be assessed before incorporating it into the simulations. Although good agreement with experimental data has been found in previous work using this model, the much shorter timescales involved here necessitate a more thorough check of the relevant approximations. Firstly, The TTM requires that both the electron and phonon subsystems are themselves in a local equilibrium; that is the electron-electron scattering maintains a Fermi-Dirac distribution with a well-defined temperature, T_e, and the phonon-phonon scattering maintains a Bose-Einstein distribution with a well-defined temperature, T_i [165]. The rate at which electron-electron

thermalisation occurs, τ_e, can be estimated from the relation [166],

$$\tau_e \approx \frac{\hbar E_F}{2\langle E \rangle^2} \ , \tag{3.3}$$

where E_F is the Fermi energy and $\langle E \rangle$ is the mean electron energy. For the gold nanofoil used in this experiment, $E_F = 5.53$ eV and based on the laser used in this experiment, we expect electron temperatures on the order of 1000 K to be comfortably attainable. This corresponds to an average electron energy of $\langle E \rangle = 0.086$ eV, thus giving an approximate electron-electron thermalisaton time of 0.25 ps. In previous experiments on gold films of a similar thickness to those used here, the electron distribution was found to be Fermi-Dirac-like after 0.8 ps [182] or even ~ 0.05 ps [178]. Our calculation, together with both previous measurements, indicate that this process is much faster than the electron-phonon equilibration timescale and hence the thermalisation process can be considered instantaneous in the simulations. A complete non-equilibrium treatment of the electron subsystem, which has previously been shown to affect the energy transfer to the lattice [178], is therefore not necessary in this case. Furthermore, given the relatively large laser spot size compared to the thickness of the gold foil, the heating of the sample may be treated as a one-dimensional problem. The ballistic nature of the hot electrons causes the target to equilibrate spatially across its depth within a picosecond after the initial laser interaction [183, 184]. This means that the source term in equation 3.1a does not depend on the spatial coordinate. Considering these two arguments, together with the very short pulse duration (50 fs), the source term may therefore be approximated as $S_e(\mathbf{r}, t) \approx S_e \delta(t)$.

However, the thermalisation time for the phonon subsystem is much longer, with theoretical studies estimating it to be on the order of tens of picoseconds. On the timescales probed here, the phonon subsystem is therefore expected to be out of local-equilibrium. In our experiment, the change in phonon temperature remains relatively

small, with a $\sim$ 10% increase from 300 K to $\sim$ 330 K. The phonon subsystem can therefore be described with a Bose-Einstein distribution at 300 K with the addition of a small number of out-of-equilibirum phonons [166]. The additional excitation of the subsystem is assumed to have a negligible effect on the energy transfer during the relaxation process.

Finally, it is necessary to estimate the importance of the thermal conductivity term in equation 3.1b, by calculating the time it takes for the temperature to equilibrate throughout the spatial extent of the gold sample. The characteristic timescale associated with the equation $dE/dT = K \nabla T^2$ can be approximated by [185],

$$t \approx \left(\frac{K\Delta T}{L^2 E_{in}}\right)^{-1} , \tag{3.4}$$

where L is the thickness of the sample and E_{in} is the energy density. For the 200 nm thick gold foil, with a ΔT of $\sim$ 30 K, $E_{in} = 5$ eV nm^{-3} and $K = 310$ W m^{-1} K^{-1}, we find this time to be $\sim$ 3.5 ns. This result makes the thermal conductivity negligible on the timescales considered in these simulations and hence can be assumed to be zero. The evolution of the electron and ion temperatures in the sample is therefore solely dominated by the electron-phonon coupling constant, g, whose value we expect to be constant with temperature under the small range of conditions found in our experiment [144]. The timescale of the relaxation rate is therefore expected to be on the order of several picoseconds.

3.5.2 Simulation details

The aim of the simulations is to use equation 3.1b, varying the rate at which energy is transferred to the ions, to find the best match to the experimental data. The simulations were performed in the LAMMPS package [112], using the 30Sep13 version on an Ubuntu 12.04 operating system. The simulations employed a microcanonical

ensemble and used 114 916 atoms in a 3.98 nm × 2.30 nm × 218 nm box, which is equal in size to 3 × 3 × 300 gold crystal unit cells. The small cross-section used here replicates the one-dimensional nature of the problem. The simulation box was divided into 7 nm of vacuum and 211 nm of gold with the crystal lattice orientated along the (111) plane. Each simulation was run with a 1 fs time step and the total number of timesteps in each simulation was 300 000. The simulations were run for 50 000 timesteps before heating to ensure that the crystal was initially at rest. A viscous damping factor, γ, was applied to the gold lattice to model the energy loss to the mica substrate on the back surface of the target. This factor allowed the speed with which the gold loses energy to be adjusted.

The forces between the gold atoms were calculated using an embedded atom model potential [186]. This choice of this potential was based on its accurate predictions of both the lattice constant and the bulk modulus of gold, which directly affect the diffraction angle and sound speed respectively. We therefore expect to be able to accurately capture the acoustic dynamics of the system. An exponential function was used as an approximate solution to equations 3.1a and 3.1b for a given initial electron temperature. Energy was deposited into the ion subsystem by exponentially decreasing amounts, with a time constant equal to $\tau = C_e/g$ [187], where $C_e = 67.6\ T_e$ J m^{-3} K^{-2} [144]. This solution accounts for the energy relaxation between the electrons and the ions via the TTM. Finally, the predicted diffraction line was calculated from the Fourier transform of the atomic positions at each time step. The peak position in reciprocal space is related to the diffraction angle by,

$$k = 4\pi(E_0/hc)\sin(\theta/2) \ , \tag{3.5}$$

where E_0 is the energy of the diffracted X-rays and k, the scattering wavenumber. A shock wave is launched into the bulk sample as the electrons are initially heated

by the laser. The subsequent oscillations shown in the diffraction peak position for delay times greater than 40 ps are caused by the reverberation of the sound wave between the front and back surfaces of the gold foil (see figure 3.5). The timescale of this process is much longer than that of the energy relaxation between the electrons and the ions (which happens in less than 10 ps), and it can therefore be used to infer the long-term mechanical behaviour of the gold foil in response to the short-time perturbation caused by the laser interaction.

3.5.3 Fitting parameters

The simulations leave four free parameters which must be varied in order to fit the data for $t > 40$ ps. These parameters are the total energy absorbed into the gold target, E_{in}, the final temperature of the lattice, T_f, the damping coefficient γ, and the thickness of the gold nanofoil, l. Although the quoted thickness of the foil is 200 nm, this is only known within a $\pm$ 20 % degree of accuracy, and hence, since it strongly affects the oscillation period, it must be varied in order to find good agreement. The predicted behaviour associated with changing each of these parameters is displayed in figures 3.6 and 3.7. The choice of the final temperature of the lattice affects the equilibrium lattice spacing at late times, while the damping coefficient determines the timescale over which the lattice attains this new spacing. The total energy absorbed is related to the depth of the first trough in the oscillatory motion, as well as the amplitude of the subsequent ringing motion. Finally, the gold thickness, as already stated, alters the period of these oscillations. These parameters all affect the simulation results in different ways and hence, their effects are considered independently. Good agreement was found for $T_f = 320 \pm 10$ K, $\gamma = 90 \pm 30$ ps, $E_{in} = 5.2 \pm 1.6$ eV nm^{-3} and $l = 210 \pm 20$ nm. A least squares best fitting algorithm was found to give poor qualitative agreement to the data and hence such a method has not been used in this case. Instead, each of the parameters has been varied by hand in order to reproduce

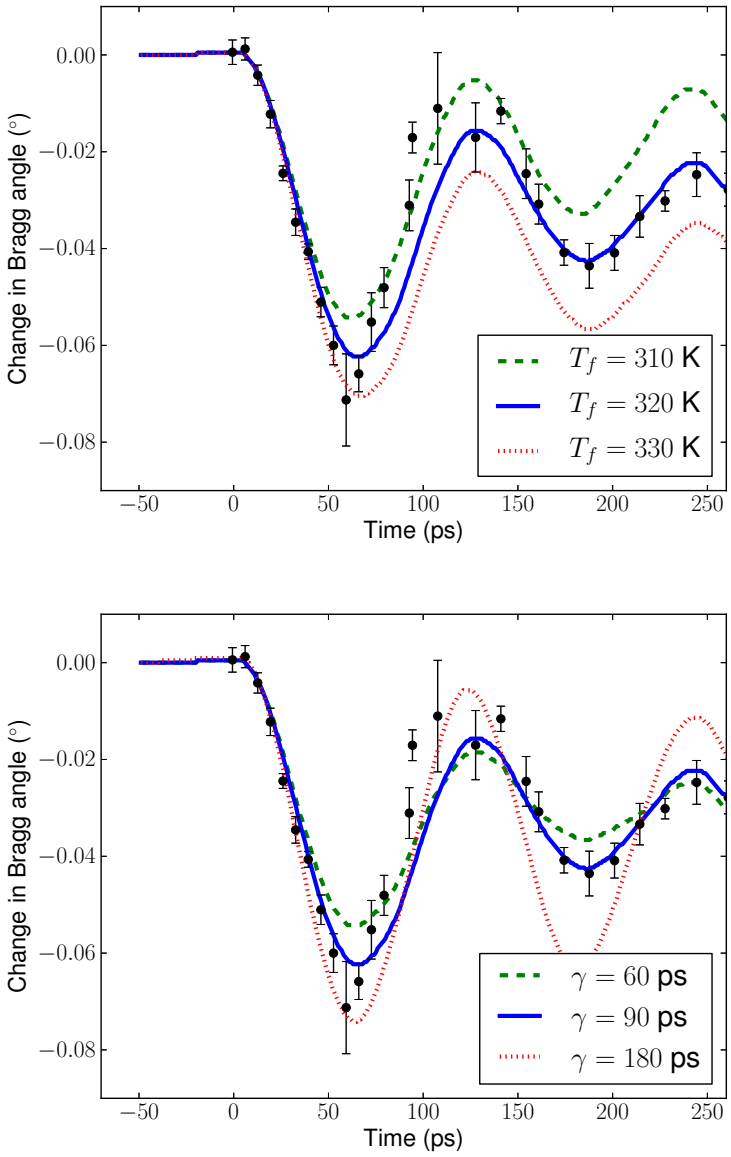

Figure 3.6: Change in diffraction angle from the gold nanofoil, overlayed with results from molecular dynamics simulations. The effect of changing the final temperature of the lattice and the damping coefficient is shown. The solid line represents the value chosen by hand for best agreement, while the dashed and dotted lines show the effect of varying the parameter in question.

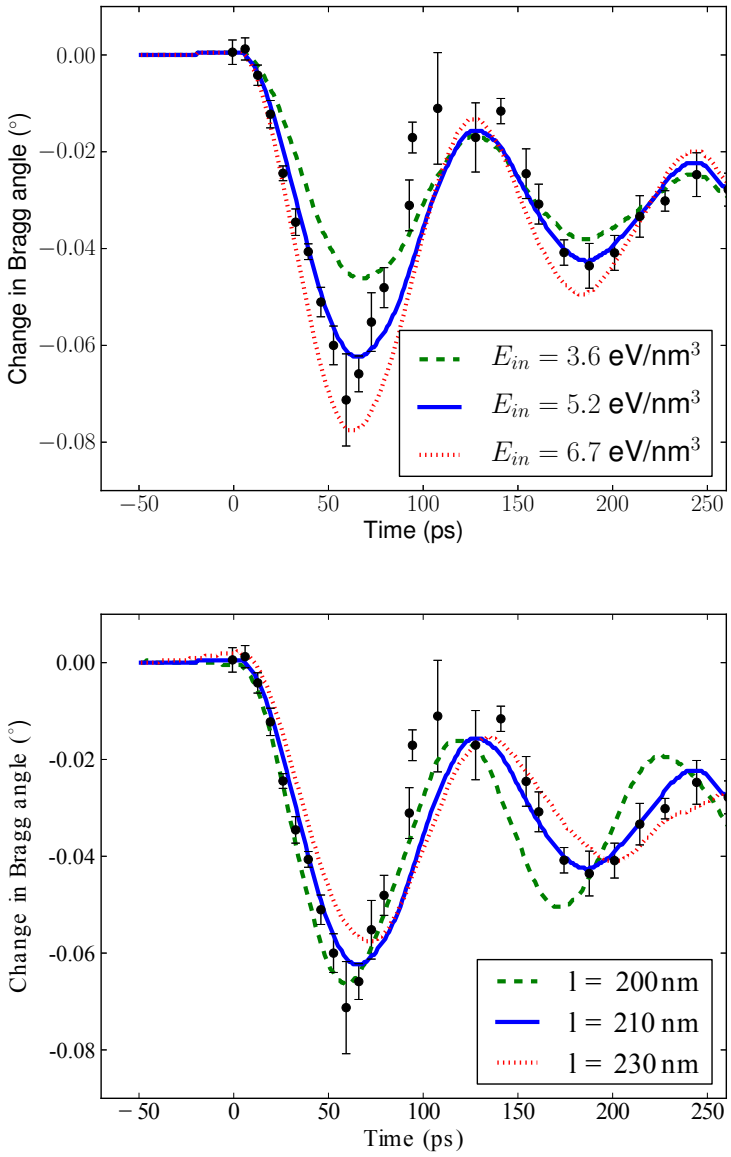

Figure 3.7: Change in diffraction angle from the gold nanofoil, overlayed with results from molecular dynamics simulations. The effect of changing the energy absorbed by the lattice per nanometre cube and the thickness of the gold is shown. The solid line represents the value chosen by hand for best agreement, while the dashed and dotted lines show the effect of varying the parameter in question.

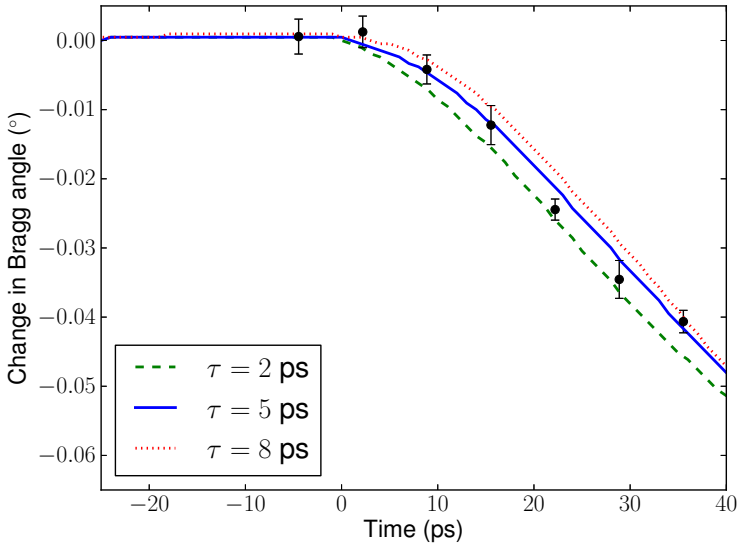

Figure 3.8: The variation of the time constant, τ, in the simulations. The solid line represents the best fit ($\tau = 5$ ps) while the dashed and dotted lines are under and over-estimates ($\tau = 2$ ps, 8 ps) respectively.

the experimental data. The confidence intervals quoted here are estimated using the same method, with each individual parameter being varied until poor agreement with the data is observed. The upper and lower curves in figures 3.6 and 3.7 show how simulation results vary within the quoted confidence intervals.

3.6 Results

Once these parameters were determined, and the long-time behaviour well described, the value of the energy relaxation time, τ was varied in order to fit the short-time behaviour of the system (t $<$ 40 ps). At these times, the behaviour of the gold atoms is strongly determined by the electron-phonon coupling parameter, g. This is shown in figure 3.8. It was found that a relaxation time of $\tau = 5 \pm 3$ ps finds good agreement with the experimental data. This leads to an electron-phonon equilibration constant of $g = 2 \pm 1 \times 10^{16}$ W m^3 K^{-1}, which closely agrees with previous studies [143]. A summary of various measured electron-phonon coupling constants, based on several

Method	τ (ps)	g ($\times 10^{16}$ W m^{-3} K^{-1})	Ref.
Bragg peak shift (MD)	5 ± 3	2 ± 1	this work
Bragg peak shift (acoustic)	5.0 ± 0.3	1.6 ± 0.1	[143]
Bragg peak intensity	4.7 ± 0.6	1.8 ± 0.2	[188]
Surface expansion	1.5 ± 1.0	1.6 ± 0.6	[189]
Surface reflectivity	4.0 ± 1.0	2.2 ± 0.3	[187]
Ab initio calculation		2.5	[144]

Table 3.1: Electron-phonon coupling time in gold measured in this work, compared to various values reported in the literature, taken from both experimental and theoretical studies.

different experimental and theoretical techniques, is presented in table 3.1.

3.7 Conclusions

The electron-phonon coupling time obtained in this work agrees with the reported data in a similar experiment [143], where it was determined by observing the shift in position of the peaks due to acoustic reverberation within the gold sample. Our analysis, however, indicates that other factors may also determine the position of these peaks, which are not directly related to the energy relaxation time. Figure 3.8 demonstrates that the energy loss to the mica substrate, in particular, plays a significant role in determining these peak positions. We therefore argue that the results displayed here give a more reliable estimate of the temperature relaxation time than previous work. The results do agree well with previous values, confirming that the energy relaxation process in gold is a fast process in the bulk as well as on the surface of the sample. On the other hand, the error quoted in this work is higher than others in the literature. This is most likely down to the way in which the simulation parameters were varied and compared to the experimental data. A simple best fit algorithm was found to be incapable at selecting appropriate values of these parameters. As such they were varied by hand in order to find good agreement with a cautious es-

timation of the confidence intervals. This fact, coupled with the overall insensitivity of the MD system to the relaxation time, explains the difference between the work presented here and in the literature. A more comprehensive automated fitting procedure would be able to determine the temperature relaxation rate with a higher precision. Nevertheless, the agreement of various different experimental methods for determining the electron-phonon coupling parameter strongly raises the confidence in this result at low excitation values. Combined with the discrepancies for higher energy input both for solids and fluids, this finding further points towards changes to the relaxation behavior in strongly driven systems. This work highlights the possibility to study energy relaxation processes in non-equilibrium systems through large-scale MD simulations. This could be a particularly successful method at describing highly correlated systems where the complex ion-ion interactions render experiments on this regime difficult to describe [190, 191].

Chapter 4

Characterisation of an X-ray lens for use as a diagnostic tool

This chapter demonstrates the ability of an X-ray polycapillary lens to focus divergent laser-produced X-ray sources to sufficient intensities such that they can probe dense plasma physics phenomena that would otherwise have been inaccessible. Previous work has shown the potential of such lenses using small-sized lasers with fast repetition rates ($\sim$ 10 Hz) [192]. Here, the possibility to use them with far more intense laser beams requiring minutes to hours between shots is discussed.

4.1 Introduction

The study of dense plasmas is relevant to many fields including laboratory astrophysics [193, 194], inertial confinement fusion research [69, 195], and more broadly in the high energy density physics community [104]. In order to understand and model experiments in this regime, accurate measurements of plasma conditions such as temperature, density and ionization state are required. Optical scattering techniques have been employed for many years in the study of low density plasmas with much success [196, 197, 198]. Dense plasmas, on the other hand, are opaque to pho-

tons in the optical range and so X-ray sources rather than optical lasers must be used in order to probe such states. X-ray Thomson scattering has subsequently been developed in order to apply these methods to the field of dense plasmas [199, 200, 91].

High power optical lasers are routinely used to produce intense X-ray pulses by driving metal foils [201, 202, 203]. This provides the ability to pump and probe samples at solid densities and above, with time resolution of picoseconds [204] or femtoseconds [1]. Recent applications include the study of shock-compressed matter [205], the characterization of fundamental thermodynamic properties including phase transitions [84, 206], the measurement of electron-ion temperature equilibration rates [1, 59, 138, 90], and the observation of plasmons [91].

The X-ray source used to obtain these results must fulfill stringent requirements on photon number, bandwidth and divergence in single shot experiments [207]. These requirements often necessitate a very small separation (a few mm) between the backlighter target used to produce X-rays and the main sample to be driven. This inevitably leads to signal-to-noise problems with detectors such as CCDs or image plates. As a result, the number of X-ray photons is often insufficient to arrive at meaningful conclusions. The problem is worsened as progress is made towards probing matter at ever higher densities and pressures. With recent reports of pressures as high as 800 GPa in solid material produced by laser compression experiments, achieving further improvements to the quality of X-ray diagnostics is becoming increasingly important [208]. Novel techniques for extracting meaningful data from background noise have been proposed but are not always applicable [209]. In addition to this, the geometry of many pump-probe experiments is restricted due to the need to shield detectors sufficiently from background noise.

The work described here opens up the possibility of using X-ray lenses in the high energy density physics community. One key advantage of this type of optic is that the backlighter and sample targets may be placed at a separation of 10s of cm, thus drastically increasing the signal-to-noise ratio. Additionally, this approach also has the potential to enable smaller-sized laser facilities to conduct cutting edge research that has previously been solely the remit of large-scale lasers, by increasing the overall number of X-ray photons available in an experiment.

4.2 Experimental setup

4.2.1 X-ray polycapillary lens

A polycapillary lens consists of an array of thin hollow glass tubes or capillaries that act to guide x-rays along its length. It can be used to collect divergent X-rays emitted from an X-ray source in a large solid angle and to transmit them with high efficiency by multiple total reflections in the individual capillaries, thus forming an intense focused beam. The capillary array is tapered so that one end of the capillaries point at the X-ray source and the other at the sample. As only X-rays entering the capillaries within a certain angle will be reflected, only X-rays coming from a small source size will be transmitted through the optic. Polycapillary optics cannot image more than one point to another, so they are used for illumination and collection of X-rays. This type of optic is achromatic, collecting X-rays efficiently for photon energies of 0.1 to 30 keV. The lens used in this experiment as manufactured in Germany by ifG - Institute for Scientific Instruments GmbH. The capillaries are aligned to refocus a source of several hundreds of microns, 51.0 mm away from one end of the lens, to a spot of approximately equal diameter, 50.0 mm away from the other side of the lens. The lens itself measures 141.3 mm in length and so in effect (minus throughput losses) the lens acts to move the X-ray source 242.3 mm away from the laser-target interaction. The lens has an output aperture of 10.3 mm and so has a theoretical

angular divergence of 6°.

The ray paths through the lens are different depending on which capillary the ray has travelled through. The total propagation time difference, Δt, between the outermost ray and the central, unreflected one is given simply by the geometry of the lens. This can be approximated by the formula [192],

$$\Delta t = (f_1 + f_2 + l + L)(\cos(\phi)^{-1} - 1)/c \ , \tag{4.1}$$

where the symbols are defined in figure 4.1 and L is the distance between the focus of the X-rays and the detector (in the diagram shown the detector is *at* the focus of the X-rays hence $L = 0$). Here, we find Δt to be $\sim$ 1 ps. Therefore the use of this lens would not be suitable for probing phenomena that take place on timescales shorter than this, such as electron-electron equilibration.

4.2.2 Method

The work presented here was carried out on the Vulcan laser at the Central Laser Facility (UK). The experiment was carried out in two parts. The first part consisted of the production and subsequent focusing of 8.05 keV Cu K-α radiation using the polycapillary lens. The K-α radiation was produced in the usual manner with the interaction of a short pulse laser beam and a metal foil, as described in section 2.3.3. The hot electrons generated at the front plasma surface interact with the solid target itself, producing bremsstrahlung radiation and line emission. In the case of mid-Z materials, K-α emission is found to dominate the spectrum [210]. Here, we illuminated a 2 µm thick copper foil with a 10 ps short pulse laser beam operating at the fundamental wavelength ($\lambda_0 = 1054$ nm). The laser pulse energy was $\sim$ 200 J and the beam was focused by an f-15 parabola to a focal spot of 300 µm. These parameters were chosen in order to maximise the K-α production of the copper sample. The

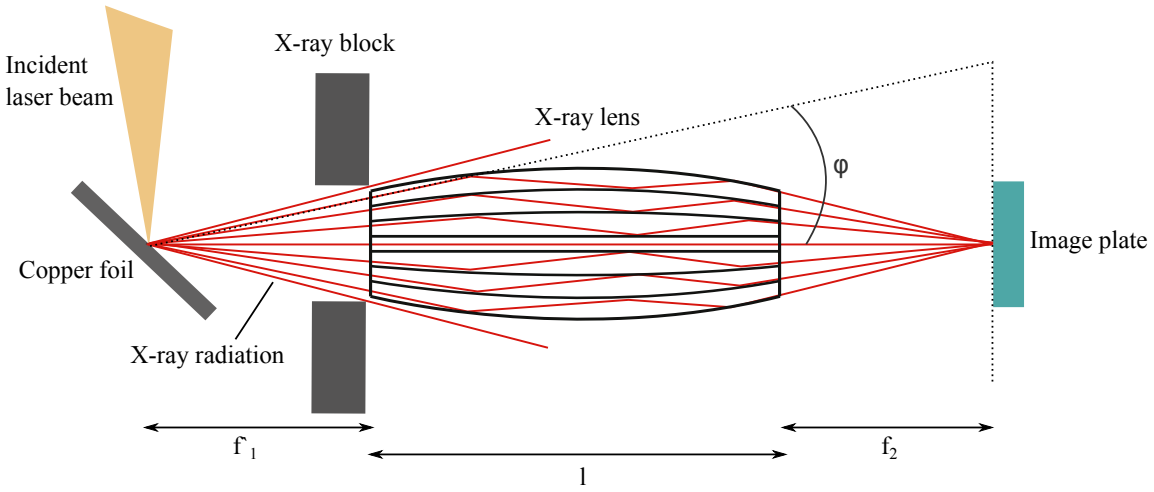

Figure 4.1: Top-down view of experimental setup. The laser beam incident from the top drives the K-α transition in the copper foil. The resulting line radiation is focused by the X-ray polycapillary lens onto an image plate 242.3 mm away. A lead block shields the image plate from direct line of site to the copper foil such that all X-rays incident on the image plate have travelled through the lens. $f_1 = 50.0$ mm, $f_2 = 51.0$ mm, $l = 141.3$ mm and $\phi = 6^{\circ}$.

X-rays are emitted roughly isotropically with those directed towards the lens focused down to a spot on the image plate detector as shown in figure 4.1. A lead shield was used to prevent any X-rays travelling directly from the copper foil to the image plate. The lens was optimised and the X-ray spot was characterised for future use. The image plates used (Fujifilm BAS-SR) require scanning after each shot taken, thus the target chamber could not remain at vacuum but instead had to be let-up and pumped down between shots. Additionally, in order to minimise fading effects, all image plates were shielded from ambient optical light using metallic filters and scanned at a set time after exposure.

In order to characterise the X-ray spot output from the polycapillary, it was first necessary to align the lens to a high degree of precision. Initially, two counter-propagating He-Ne lasers were used to define an axis running from the focal spot of the laser on the metal foil to a point in the plane of the image plate. The lens

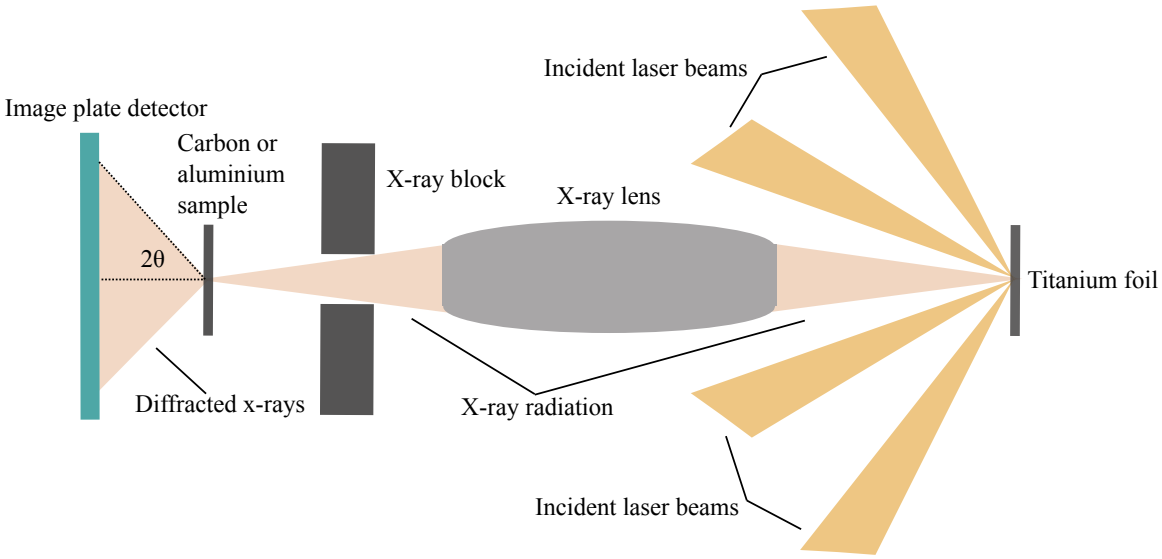

Figure 4.2: Top-down view of experimental setup. The incident laser beams drive the He-α transition in the titanium foil on the right hand side of the diagram. The resulting line radiation is focused by the X-ray polycapillary lens onto a target (both pyrolytic graphite and polycrystalline aluminium were used) 242.3 mm away. The X-rays are diffracted according to Bragg's law and are detected by the image plate. Direct line of site from the titanium foil to the image plate is blocked with a lead shield.

was then placed on this axis between the metal foil target and the image plate (see figure 4.1). The short pulse beam was then fired to generate short pulse Cu K-α line radiation at 8.05 keV, which was focused by the lens onto a spot on the image plate. The lens was then translated both horizontally and vertically to optimise the intensity of the X-ray spot on the image plate. During this process, the lens was not moved in the focal direction nor was it rotated around its axis. Ten shots were required on average to align the lens. Once the lens was aligned, the X-ray spot was characterised by measuring the peak intensity, the total number of photons contained within, the spot size, the angular divergence and the brilliance, in order to compare to other X-ray sources.

In the second part of the experiment, four 1.5 ns long-pulse beams, frequency doubled to $\lambda_0 = 527$ nm, were used to drive the He-α transition in titanium. A total of ~ 400 J

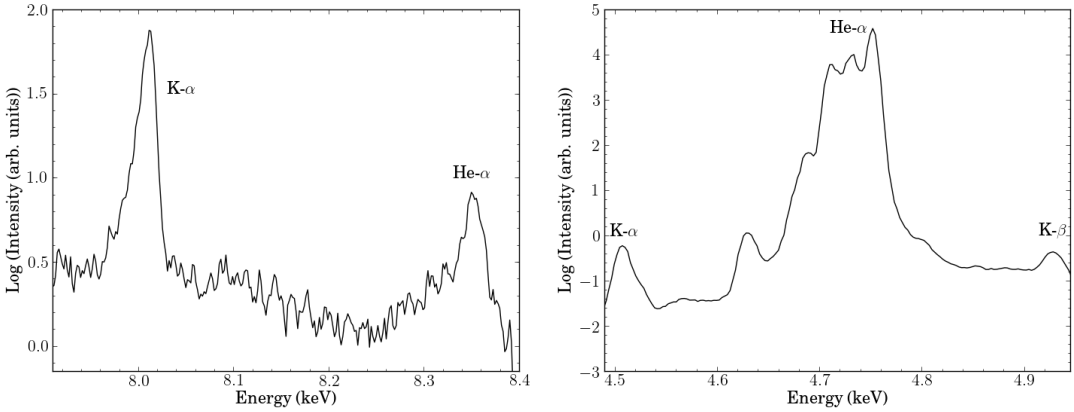

Figure 4.3: (Left) X-ray spectra produced by interaction of 200 J, 10 ps laser beam with 2 µm thick copper foil. The peaks correspond to K-α and He-α transitions respectively. (Right) X-ray spectra produced by interaction of four 100 J, 1.5 ns laser beams with 10 µm thick titanium foil. The three central peaks correspond to the three characteristic He-α transitions. Also seen are several satellite peaks including K-α and K-β. As expected, it is found that the long pulse laser beams primarily drive the He-α transition, while the short pulse beam favours the K-α transition.

was incident on the titanium target within a focal spot of 50 µm. The X-rays were again focused by the polycapillary lens onto an image plate and the lens was aligned in the same manner. Once this was completed, a target was placed at the focus of the X-rays as shown in figure 4.2. The X-rays diffract from the sample by Bragg's law and were incident on the image plate detector situated behind the sample.

4.3 Results

A flat HOPG (highly ordered pyrolytic graphite) spectrometer was placed 20 cm away from the backlighter target in order to capture the X-ray spectrum generated. Initially the HOPG crystal was aligned such that the Cu K-α peak was diffracted from the (004) plane of the crystal onto an image plate detector. For the titanium targets, the setup was changed such that the Ti He-α radiation was diffracted from the (002) plane of the HOPG crystal onto the image plate. The He-α line is separated into three distinct peaks as is expected [211]. Also present are several satellite peaks

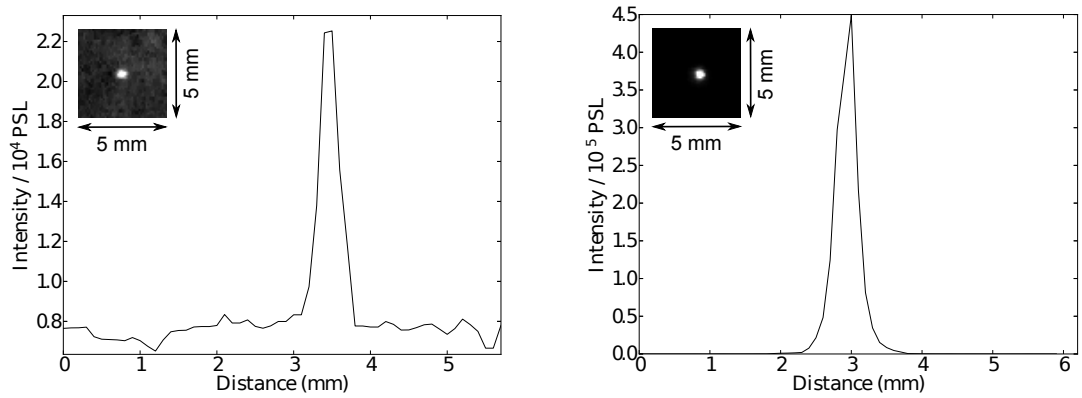

Figure 4.4: Lineouts of X-ray spot output from polycapillary lens. (Left) X-ray source produced by interaction of 200 J, 10 ps laser beam with 2 µm thick copper foil. X-ray spot has a FWHM diameter of 403 ± 16 µm. (Right) X-ray source produced by interaction of four 100 J, 1.5 ns laser beams with 10 µm thick titanium foil. The FWHM diameter is 400 ± 20 µm. Insets show the 2-D image of the measured focal spot. Both cases are found to have area of 0.13 ± 0.1 mm^2. The background level fluctuates no more than within ± 25 %, and hence all pixels which have an intensity appreciably higher than the level of these fluctuations can be considered as part of the X-ray spot. Hence the area of the spot is calculated by summing the area covered by all pixels within the spot that have an intensity equal to at least 1.25 times the background level.

whose intensity is several orders of magnitude weaker than the He-α line [212]. Results are shown in figure 4.3 for the two cases.

4.3.1 X-ray spot characterization

It was found that the FWHM diameter was 403 ± 16 µm for the Cu He-α X-ray spot and 400 ± 20 µm for the Ti K-α X-ray spot. These values were taken from the scans of an image plate placed at the focus of the lens as shown in figure 4.1, and averaged over three shots, with the data displayed in figure 4.4.

The absolute number of X-ray photons in each spot is calculable from the intensity read-out of the image plates. Firstly, since the IP scanner digitizes the plate readout using a logarithmic amplifier, the measured pixel data were converted between this

	Copper K-α	Titanium He-α
Spot size	0.13 ± 0.1 mm^2	0.13 ± 0.1 mm^2
Peak intensity (PSL/pixel)	$2.2 \pm 0.3 \times 10^4$	$4.5 \pm 0.2 \times 10^5$
Peak intensity (photons/pixel)	$\sim 2.2 \times 10^7$	$\sim 4.5 \times 10^8$
Total PSL	$2.9 \pm 0.4 \times 10^5$	$6.3 \pm 0.3 \times 10^6$
Total photons	$\sim 2.9 \times 10^8$	$\sim 6.3 \times 10^9$
Brilliance (photons s^{-1} mrad^{-2} mm^{-2})	$\sim 10^{16}$	$\sim 10^{15}$

Table 4.1: Results of X-ray spot characterisation from both copper K-α sources and titanium He-α.

logarithmic value, or quantum level (QL), to a linear photo-stimulated luminescence (PSL) scale [213],

$$PSL = \left(\frac{R}{100}\right)^2 \times 10^{5(QL/G-0.5)} \quad , \tag{4.2}$$

where R is the scanning resolution in microns and G is the gradation. In this case, $R = 100$ µm and $G = 65536$, which corresponds to a 16 bit digitisation. The relationship between PSL and number of X-ray photons has been shown to be linear [213], with a PSL of 1 corresponding to $\sim$ 1000 photons. The total number of photons within the X-ray spot are then found by integrating the total PSL count and using this conversion factor.

Since the polycapillary lens focuses X-rays of all energies above $\sim$ 1 keV, the energy spectrum of the lens output is very similar to the original laser-produced X-ray source. Therefore, the lens has minimal effect on how monochromatic the source is, compared to a conventional setup. The divergence of the X-rays output from the lens was also calculated by moving the image plate detector behind the focus of the lens and measuring the subsequent increase in size of the X-ray spot. The angle of the X-ray cone is measured to be 6 ± 1^o. This result agrees with the expected value of angular divergence given the geometry of the polycapillary lens, as mentioned in section 4.2.1. Using this information, one may calculate the peak brilliance of the

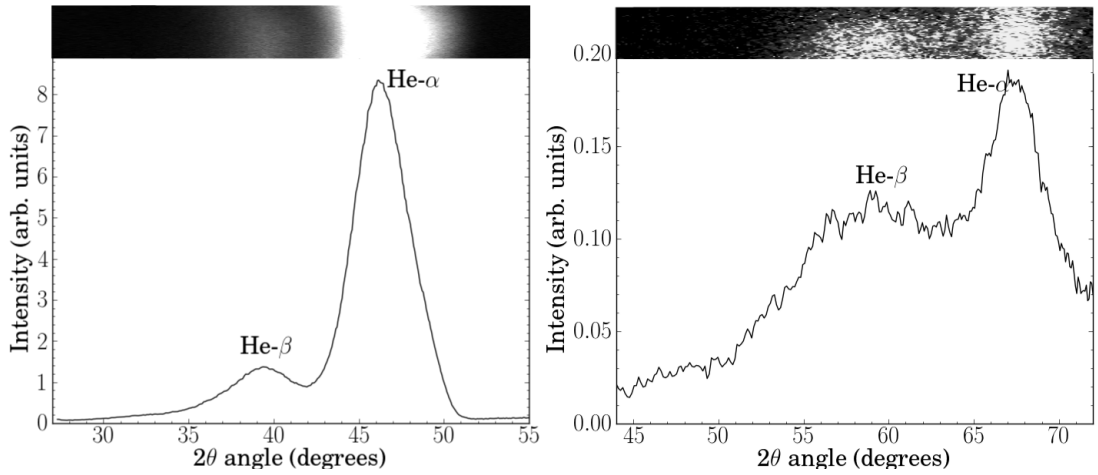

Figure 4.5: Plots of the diffraction from (left) the (002) plane in pyrolytic graphite and (right) the (111) plane in polycrystalline aluminium. The X-ray source used is titanium He-α focused by the polycapillary lens. Also visible is the satellite peak: the He-β line at 5.57 keV. Insets show part of diffraction line taken from image plate scan of single shot (Both 2-D image and lineouts share common x-axis.)

X-ray source in both cases.

Table 4.1 displays the photometric information for both sources, with the He-α source containing a greater overall number of photons, as expected. Although the brilliance of both compares poorly to dedicated X-ray sources such as synchrotrons or FELs, this is to be expected. A more appropriate comparison is with commonly-used laser produced X-ray sources: in order to attain the peak photon intensities reported here, one would have to place the backlighter target just ~ 6 mm away from the sample[1]. The lens therefore allows for a great deal more flexibility in experimental design and provides the opportunity to greatly improve the signal-to-noise ratio on detectors.

4.3.2 X-ray diffraction

The lens-focused Ti He-α X-ray source was then used to study the structure of two materials: pyrolytic graphite and polycrystalline aluminium. The setup used is depicted

[1]This result was calculated assuming typical He-α and K-α conversion efficiencies [214] and that the X-ray source can be described as isotropic and point-like.

in figure 4.2 with a distance of 40 mm from the graphite or aluminium sample to the image plate. Pyrolytic graphite is characterised by its ordered nature; it comprises many graphite layers in a hexagonal close packed structure, which have a relatively small angular spread. For this reason, it is essential that the X-rays are incident onto the sample at an angle which satisfies the Bragg condition. In this case the incident angle of X-rays onto the sample was 23^o, which represents the Bragg angle for the diffraction of 4.75 keV X-rays from the (002) plane in graphite. The diffraction angle is calculated simply from the ratio of horizontal and vertical distances travelled by the X-rays between the sample and the image plate.

The process was then repeated for a polycrystalline aluminium sample. In this scenario the incident angle of the X-rays is unimportant due to the polycrystalline structure of the sample: there will always be some crystal structures orientated such that the Bragg condition is met regardless of incident angle. A diffraction ring was seen on the image plate and a lineout was taken in order to determine the angle in the same way as before. The results of both aluminium and graphite are displayed in figure 4.5.

4.4 Conclusions

This work has shown the ability of X-ray polycapillary lenses to focus laser-produced X-ray sources to high intensities. Assuming typical He-α and K-α conversion efficiencies of 10^{-4} and 10^{-5} respectively, one would have to place the backlighter target just $\sim$ 6 mm away from the sample, to attain the peak photon intensities reported here. However, with the setup outlined here, one is able to separate these two targets to a distance of 242.3 mm, greatly improving the signal-to-noise ratio. This is demonstrated by two simple diffraction experiments using pyrolytic graphite and polycrystalline aluminium. The diffracted He-α and He-β lines were seen with a good

signal-to-noise ratio in both cases. Future experiments to study high energy density states of matter could achieve better X-ray scattering or diffraction results using this type of X-ray optic.

Chapter 5

Molecular dynamics calculations of dynamic structure factors

This chapter presents molecular dynamics calculations of the ionic component of the dynamic structure factor, as well as the ion mode dispersion relation, for the example case of warm dense aluminum.

5.1 Introduction

The state and evolution of planets, brown dwarfs and neutron star crusts is determined by the properties of dense and compressed matter, such as the equation of state, viscosity and thermal conductivity [6, 13, 132, 215]. Modelling matter in this regime is very challenging as one often encounters systems with strong interactions, as well as electrons that exhibit distinct quantum behaviour. Thus, either first principle simulations or reduced models are applied to determine the system properties. Investigating the ion dynamics is particularly challenging as the pure Coulomb interactions between the ions are modified by electron structure, i.e., the bound state properties and screening [190, 216]. In turn, this behaviour makes the ion modes very interesting as they encode almost the entire system behaviour, including elec-

tron properties [217]. Due to the inherent difficulties in modelling strongly coupled plasmas, current predictions of transport coefficients differ by many orders of magnitude [12]. This deficiency not only affects our ability to understand planets and stars, but also impacts predictions for the implosion characteristics in inertial confinement fusion experiments [69, 162], as well as material modifications by lasers [161].

The prominent collective modes found in the dynamic structure factor, introduced in section 2.5.3, serve as an important tool to validate theoretical predictions for dense matter. Until recently, however, only electron modes could be measured experimentally [91, 99, 218]. With the recent advances in free electron laser technology, X-rays with bandwidth small enough to allow the investigation of the low-frequency ion modes in dense matter have become available as well [111]. Nevertheless, the experimental possibilities to diagnose dense matter are still rather limited and a thorough comparison of simulations and data is often the only way to reveal the microscopic behaviour.

5.2 Density functional theory

The general method to extract the dynamic structure factor from an MD simulation is to take the spatial and temporal Fourier transform of the particle positions over a large number of timesteps; in itself, a relatveily simple task. In practice, this is complicated by the non-negligible electron degeneracy in the warm dense matter regime, making a fully-classical treatment of such a system, with typical pair-potentials, inappropriate.

Here we make use of the density function theory (DFT) method to calculate the

inter-atomic potential on-the-fly, thus going beyond simple classical mechanics. The success of DFT is clearly demonstrated by the overwhelming number of previously published articles [154, 125, 126, 219, 220]. We now outline some of the fundamental physics which underpins this technique. For a more complete picture see e.g. ref [221]. The first step is to find the solution to the ground state energy of a many body system through solving the Schrödinger equation,

$$\hat{H}\phi = E\phi \quad . \tag{5.1}$$

DFT attempts to solve the time-independent non-relativistic form of this equation, and while time-dependent versions do now exist their relatively high computational cost limits their use to specific cases such as electronic transitions. The total energy operator can be written in terms of the kinetic energy, electron-nucleus and electron-electron energy operators respectively,

$$\hat{H} = \hat{T} + \hat{V}_{en} + \hat{V}_{ee} \quad . \tag{5.2}$$

In equation 5.2, the Born-Oppenheimer (BO) approximation has been used to simplify the problem by assuming that the motion of ions and electrons can be separated. The success of this approximation is due to the difference between nuclear and electronic masses, which allows the wavefunction of a molecule to be broken into its electronic and nuclear components. The BO approximation is ubiquitous in quantum chemical calculations of molecular wavefunctions and in other molecular dynamics studies of dense plasmas [125, 126, 222, 223].

While solving this equation is possible, it is exceptionally difficult for all but the simplest of systems. DFT, on the other hand, is a theory which allows the complex many electron wavefunction to be replaced with a simple function of the electron density. DFT relies on two fundamental theorems that were first proved by Hohen-

berg and Kohn in their 1964 paper [224]. The first states that the ground state properties of a many-electron system are uniquely determined by an electron density that depends on only 3 spatial coordinates. It lays the groundwork for reducing the many-body problem of N electrons with $3N$ spatial coordinates to just 3 spatial coordinates, through the use of functionals of the electron density. In other words, the electron density, $\rho(\mathbf{r})$, can uniquely define the external potential, $v(\mathbf{r})$, for any system (within an additive constant).

The proof of this theorem is quite simple and is demonstrated here. We begin by considering two systems with different potentials v_1 and v_2 but with the same ground-state electron density, ρ. We must then have two different Hamiltonians, $\hat{H}_1$ and $\hat{H}_2$, with two different ground-state wavefunctions, ϕ_1 and ϕ_2. Given that $E_0 = \min(\phi)\ E[\phi]$, it follows that $E[\phi] \geq E_0$. By inserting the wavefunction, ϕ_2 into the Hamiltonian for system 1, this inequality may be written as,

$$E_{01} < \langle \phi_2 \mid \hat{H}_1 \mid \phi_2 \rangle = \langle \phi_2 \mid \hat{H}_2 \mid \phi_2 \rangle + \langle \phi_2 \mid \hat{H}_1 - \hat{H}_2 \mid \phi_2 \rangle \quad . \tag{5.3}$$

Similarly, inserting the wavefunction ϕ_1 into the Hamilton for system 2 gives,

$$E_{02} < \langle \phi_1 \mid \hat{H}_2 \mid \phi_1 \rangle = \langle \phi_1 \mid \hat{H}_1 \mid \phi_1 \rangle + \langle \phi_1 \mid \hat{H}_2 - \hat{H}_1 \mid \phi_1 \rangle \quad . \tag{5.4}$$

Adding these two equations together, and recognising that $\langle \phi_{1,2} \mid \hat{H}_{1,2} \mid \phi_{1,2} \rangle = E_{01,02}$ gives,

$$E_{01} + E_{02} > E_{02} + E_{01} \quad , \tag{5.5}$$

which is obviously a contradictory statement. Thus there cannot be two different potentials that give the same ground-state electron density. Hence, for a given electron density, a unique Hamiltonian is also defined. From this Hamiltonian, it is then possible to find all the wavefunctions describing the electronic density and thus the

material properties of the sample. Equivalently, this can be written as, $E = E[\rho]$.

The second theorem states that for any positive density, such that $\int \rho dr = N$, then $E[\rho] \geq E_0$. Together, the two statements define a constrained minimisation problem, which can be represented through the Kohn-Sham equation,

$$\left[\frac{-\nabla^2}{2} + v_{KS}[\rho](\mathbf{r})\right]\phi(\mathbf{r}) = E\phi(\mathbf{r}) \quad . \tag{5.6}$$

The notation $v_{KS}[\rho]$ means that the Kohn-Sham potential has a functional dependence on the electronic density, which is defined in terms of the Kohn-Sham wavefunctions by,

$$\rho(\mathbf{r}) = \sum_i \mid \phi_i(\mathbf{r}) \mid^2 \quad . \tag{5.7}$$

The Kohn-Sham potential, v_{KS}, is defined as the the sum of the external potential (normally that generated by the ions), the Hartree term and the exchange-correlation (xc) potential,

$$v_{KS}[\rho](\mathbf{r}) = v_{ext}(\mathbf{r}) + v_{Hartree}[\rho](\mathbf{r}) + v_{xc}[\rho](\mathbf{r}) \quad . \tag{5.8}$$

Due to the functional dependence on density, these equations form a set of nonlinear coupled equations. The standard procedure to solve them is by iterating until self-consistency is achieved. A schematic of this procedure is shown in figure 5.1. Usually one supplies some model density, $\rho_0(\mathbf{r})$, to start the iterative procedure. In principle, any positive function, normalized to the total number of electrons would work, but using an educated guess can speed-up convergence dramatically.

The Kohn-Sham potential is then evaluated using this density. Each of the components in equation 5.8 poses a different numerical problem and so is calculated separately. The external potential is typically a sum of nuclear potentials centered at

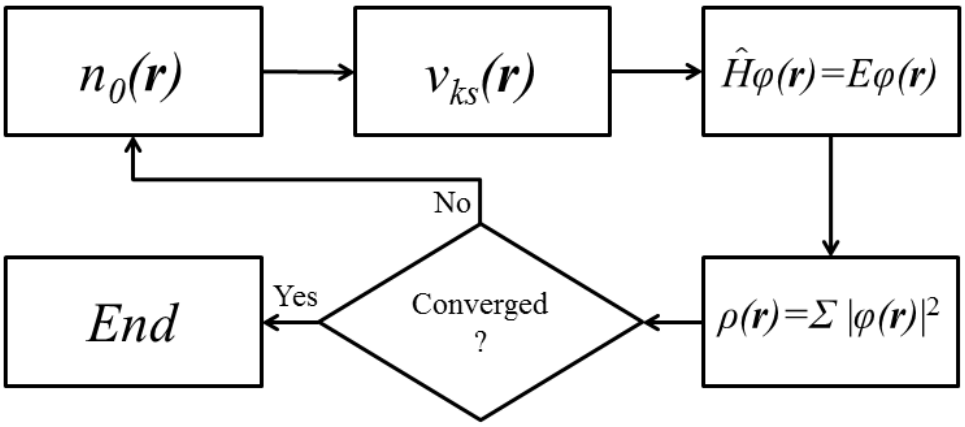

Figure 5.1: Schematic of steps involved in a typical Kohn-Sham calculation. An initial electron density is provided, which is then used to calculate the Kohn-Sham potential. Wavefunctions are subsequently calculated, which are compared to the original electron density input. This cycle is repeated until good agreement is found.

the atomic positions,

$$v_{ext}(\mathbf{r}) = \sum_{\alpha} v_{\alpha}(\mathbf{r} - \mathbf{R}_{\alpha}) \quad , \tag{5.9}$$

where v_α is often described using a pseudopotential, a concept that will be discussed in section 5.3.1. The second term in equation 5.8 is the Hartree potential,

$$v_{Hartree}(\mathbf{r}) = \int d^3r' \, \frac{\rho(\mathbf{r}')}{\mid \mathbf{r} - \mathbf{r}' \mid} \quad . \tag{5.10}$$

The evaluation of this integral is straightforward, if time-consuming, and is achieved either by direct integration, or by solving the equivalent differential equation. Finally, there is the exchange-correlation term, which is formally defined through the functional derivative of the xc energy,

$$v_{xc}(\mathbf{r}) = \frac{\delta E_{xc}}{\delta \rho(\mathbf{r})} \quad . \tag{5.11}$$

Although the Hohenberg and Kohm theorems prove the existence of this function, its general form is, at present, unknown. Hence, the success of DFT often relies on the parameterisation of this term. Numerous approximate xc functionals have appeared in the literature over the past number of years, with two of the most successful ap-

proaches being the local density approximation (LDA) and the generalised gradient approximation (GGA), with the latter being used in this work.

Having established the form of the Kohn-Sham potential, we can solve the Kohn-Sham equation (5.6). The aim is to obtain the n lowest eigenstates of the Hamiltonian $\hat{H}_{KS}$, where n is equal to half the number of electrons in the system. The electronic density can then be obtained from equation 5.7. This value is checked against the input test density for self-consistency. The cycle is stopped when some convergence criterion is reached. The two most common of these are based on the difference of total energies or densities from iteration i and $i-1$. At the end of the calculation, the total energy can be evaluated, from which one can obtain, equilibrium geometries, phonon dispersion curves, or ionization potentials.

5.3 Density functional theory with molecular dynamics

Thus far, we have outlined the fundamental principles of density functional theory and discussed how to calculate the electron density distribution based on an arbitrary ionic configuration. We have not, however, explained how this links to molecular dynamics and how to evolve the total system with time. The coupling of density functional theory with molecular dynamics is typically referred to as DFT-MD.

A typical simulation is initialised by defining an ionic configuration which provides the initial external potential used to calculate the electron density through DFT. The size of the simulation box is defined, which, when coupled with the use of periodic boundary conditions, sets the density of the system. The ions are then given a 'kick', with their velocities being described by a Maxwell-Boltzmann distribution at some chosen temperature. The ionic positions are then updated using a velocity integrator

with a pre-defined timestep. The ions experience forces from the electronic density profile as well as from each other. The new ionic configuration is then used as the external potential for a new DFT electron density configuration. This cycle is then repeated for the desired number of timesteps. Measurements are not taken from the first timesteps, so as to ensure that the system has truly reached an equilibrium state before any information is extracted. This method employs the Born-Oppenheimer approximation, separating the motions of the electrons and the ions and thus neglecting the dynamics of the electron-ion interactions.

5.3.1 Non-local psuedopotentials

DFT may be simplified if electrons are divided into valence electrons and inner core electrons. The electrons in the inner shells are strongly bound to the ions and do not play a significant role in the chemical binding of atoms, thus forming, with the nucleus, an inert core. Since most atomic processes and binding only involve the outer shell of electrons, especially in metals and semiconductors, the physics of most systems can still easily be captured by only considering the outermost electrons, ignoring the inner electrons for a large number of cases. The system is thereby reduced to an ionic core that interacts with the valence electrons. The use of an effective interaction, a pseudopotential, that approximates the potential felt by the valence electrons, was first proposed by Fermi in 1934. The pseudopotential concept was used in 1970 by V. Heine to remove the core states from the Hamiltonian and construct a pseudo-Hamiltonian containing only the outer shell of electrons. Using a simple Coulombic potential term for the core electron states produces strong oscillations in the resultant wavefunction as $r \to \infty$. This leads to a large number of Fourier components needed to describe the wavefunction and subsequently a high computational cost. Softer potentials; that is potentials which include a larger number of electrons within the ionic core, therefore lead to a smoother wavefunction at small r, and hence a lower

computational cost. These potentials also reduce the total number of electrons in the calculation, lowering simulation times further. Pseudopotentials for most elements are now commonly available and give the potentials for these atoms in terms of atomic orbitals (s,p,d,f etc.) and hence are given the name 'non-local'.

5.3.2 Orbital-free density functional theory

An accurate calculation of the dynamic structure factor in the warm dense matter regime requires an ensemble average over many particles and long timescales, and as the DFT method outlined above (often referred to as Kohn-Sham DFT or KS-DFT) is computationally expensive and intractable at temperatures above some tens of eV, it is often ill-suited to large scale MD calculations. The computational cost comes from the finite temperature treatment of the electronic orbitals, with the Fermi-Dirac distribution used to fill them, becoming broader and smoother at higher temperatures. This means that to fully describe the behaviour of all the thermally excited electrons, a large number of partially filled states must be orthogonalised; an exercise that increases with the cube of the number of particles in the system. Therefore, to use the largest system size possible, one may instead adopt an *orbital-free* density functional theory (OF-DFT) approach [225]. This method describes the electron energy functional entirely in terms of the electron density and forgoes the need to solve for the wavefunctions of the system. Both Kohn-Sham and orbital-free DFT calculations are possible within most modern day DFT codes and this functionality exists in the ABINIT software used for this work. The pseudopotential required for an orbital-free calculation must, however, be solely a function of the density and not of the orbitals. This renders typical non-local potentials used in Kohn-Sham calculations unsuitable and hence bespoke potentials must be created [226]. The orbital free method has been tested against the more comprehensive Kohn-Sham approach and good agreement has been found at temperatures of a few eV and higher [125].

5.3.3 Ionic trajectories

In general, ions in the WDM regime are *not* degenerate and hence can be treated fully classically in simulations, vastly reducing the computational cost. Therefore, as discussed in section 2.6.2, simulations typically employ Newtonian equations of motion, with a thermostat to keep a constant temperature.

One such technique is the Gaussian thermostat (sometimes referred to as the isokinetic ensemble), derived by using Gauss' principle of least constraint. It produces the canonical ensemble in the coordinate part of phase space [122] by employing time-reversible and deterministic equations of motion [227],

$$\dot{\boldsymbol{r}}_i = \boldsymbol{p}_i/m_i, \quad \dot{\boldsymbol{p}}_i = -\frac{\partial U(\boldsymbol{r}^N)}{\partial \boldsymbol{r}_i} + \zeta \boldsymbol{p}_i \,. \tag{5.12}$$

Here, m_i, $\boldsymbol{r}_i$ and $\boldsymbol{p}_i$ are the mass, position and momentum of the i-th particle respectively, $-\partial U(\boldsymbol{r}^N)/\partial \boldsymbol{r}_i$ is the force on the particle, and,

$$\zeta = \frac{1}{K_0}\left[\sum_{j=1}^{N} \frac{p_j(t)}{m_j}\frac{\partial U(\boldsymbol{r}^N)}{\partial \boldsymbol{r}_j}\right],\; K_0 = \sum_{j=1}^{N}\frac{p_j^2(0)}{m_j}. \tag{5.13}$$

One drawback associated with this thermostat is that a conventional ODE solver exhibits kinetic energy drifting and thus one has to introduce a method of *ad hoc* velocity scaling such as that proposed by ref. [228].

Another widely used approach was proposed by Nosé and Hoover [120, 121]. The Nosé-Hoover thermostat is based on the use of an extended Lagrangian containing additional artificial coordinates and velocities. The equations of motion are the same as for the Gaussian thermostat but with ζ replaced by ξ, the time derivative of which is given by,

$$\dot{\xi} = \frac{1}{W_T}\left(\sum_{j=1}^{N}\frac{p_j^2}{m_j} - 3Nk_BT\right), \tag{5.14}$$

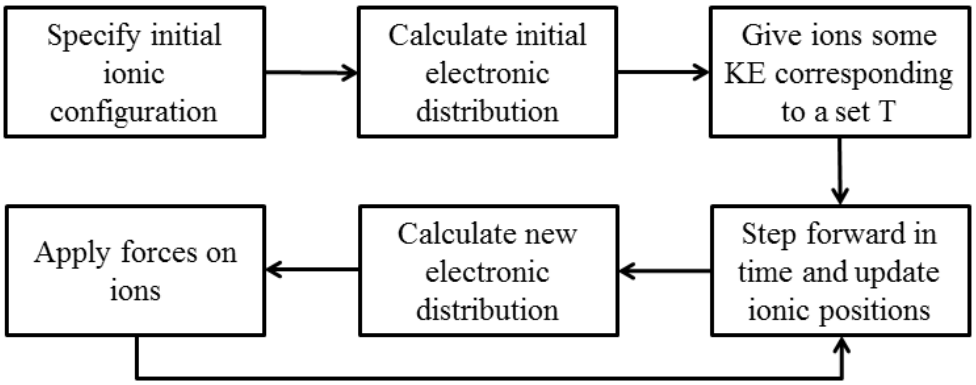

Figure 5.2: Schematic of steps involved in typical density functional theory molecular dynamics calculations. Electron density is calculated within the framework of density functional theory, while ions are propagated using classical equations of motion. The use of the Born-Oppenheimer approximation, separating the timescales for electronic and ionic motion, ignores dynamical electron-ion effects.

where W_T is the inertia factor of the thermostat.

5.3.4 Summary

Bringing together the various concepts discussed above, figure 5.2 summarises how a typical DFT-MD simulation is carried out. Although DFT results are often described as *ab initio*, several approximations are made throughout this process. It has already been shown that the xc functional and the pseudopotential chosen both have an influence on simulation results, yet there has been little work on the equations of motion governing the ionic trajectories and the possibility of including dynamical electron-ion interactions. This will be the primary focus of this chapter.

5.4 Langevin dynamics

In the last few years, collective ion modes in warm dense matter have been investigated using simulations with increasing complexity: molecular dynamics simula-

tions using model potentials [229] and potentials extracted from *ab initio* simulations [118, 230, 231, 232], orbital-free density functional theory [125], and most recently full Kohn-Sham density functional theory [126] have all been applied. These simulations are typically run with constant particle number, volume and temperature (the NVT ensemble), using either the Nosé-Hoover or the Gaussian thermostat. While some efforts have been made to include electron-ion relaxation effects with classical MD at very high temperatures [233, 234], DFT-MD simulations, required for coupled electron-ion systems in the WDM regime, always employ the Born-Oppenheimer approximation, neglecting the dynamics of the electron-ion interactions.

However, these effects may not be negligible [235, 236] and an alternative approach is to use the Langevin equation (LE) [123],

$$\dot{\boldsymbol{r}}_i = \boldsymbol{p}_i/m_i, \quad \dot{\boldsymbol{p}}_i = -\frac{\partial U(\boldsymbol{r}^N)}{\partial \boldsymbol{r}_i} - \sigma \boldsymbol{p}_i + \boldsymbol{G}_i\,, \tag{5.15}$$

where U denotes the interaction potential between the ions. The second term describes the thermostat that sets a specific temperature in the ion system by re-scaling the momenta, where σ controls the time scale of reaching the required temperature. Often applied thermostats, like the isokinetic (Gaussian) [122] or the Nosé-Hoover [120, 121] descriptions, contain only this term ($\boldsymbol{G}_i = 0$).

Within the Langevin dynamics, the additional third term, $\boldsymbol{G}_i$, describes a Gaussian random force randomizing the one-particle dynamics. This force is set to have a zero average and variance of $2\sigma k_B T$. The magnitude of the random force applied to the ions is set using the fluctuation-dissipation relation such that the ions follow a Maxwell-Boltzmann distribution with a specified temperature. Thus, the parameters σ and $\boldsymbol{G}_i$ are connected and there is only one free parameter as in the other schemes.

The Langevin approach was introduced to describe, in a stochastic manner, damping in the one-particle dynamics originating from omitted degrees of freedom. A typical example is Brownian motion where random weak collisions between particles and the background gas or fluid cannot be treated explicitly. The resulting diffusive process creates a zero-frequency mode and its strength may thus serve as an estimate of the effects of randomisation processes. This approach has previously been successfully implemented in the field of dusty plasmas to model the effects of neutral species on the diffusion coefficient [237, 238, 239]. In the case of dense ionised matter, Langevin dynamics may mimic processes like dynamic electron-ion collisions [240] usually excluded from standard simulations.

5.5 Simulation results

Here, we investigated the relative strength of the central diffusive peak, often referred to as the Rayleigh line, and the acoustic modes in the ion-ion structure factor with OF-DFT simulations employing the three different thermostats as described above. Tests against simulations applying the more detailed KS-DFT method have shown that the efficient OF-DFT yields excellent agreement for the examples studied here [125]. To illustrate effects purely related to the thermostat, we also include results from fully classical MD simulations using a Yukawa potential with a short range repulsion (SRR) term [125]. As an example, we consider a warm dense aluminium plasma, compressed to twice solid density: $T = 3.5\,\mathrm{eV}$ and $\rho = 5.2\,\mathrm{g\ cm^{-3}}$.

Classical MD simulations were performed using the LAMMPS code, version 30Sep13, on an Ubuntu 12.04 operating system. Convergence tests on box size and timestep for the DFT-MD simulations were carried out using the open-source ABINIT software, version 7.4.2 on an Ubuntu 12.04 operating system. Due to the computational power required to run these simulations for long periods of time, final calculations

were performed using the supercomputer at AWE in Aldermaston, using a Linux-based operating system. ABINIT version 7.8.2 was used to perform the OF-DFT simulations while VASP 5.4.1 was used to carry out the KS-DFT simulations due to its increased computational speed.

5.5.1 Structure factors

For the conditions above, all simulations, yield very similar static structure factors, regardless of the thermostats employed, as shown by Figure 5.3a. Thus, static properties, including the equation of states being derived from it, are insensitive to the choice of the thermostat, validating standard simulations employing a Nosé-Hoover thermostat. This is to be expected: static properties of plasmas in equilibrium, such as the SSF, should indeed be insensitive to the choice of thermostat and the kinetic coefficients. Figure 5.3b demonstrates that the DSF is, on the contrary, very sensitive to the choice made for the thermostat. While the results calculated with the Nosé-Hoover and Gaussian thermostats are very similar, the DSF extracted from the Langevin simulation clearly shows a different mode structure: the two peaks representing the ion acoustic modes, symmetric around the origin, are strongly damped when the additional damping in the Langevin formalism is introduced. Moreover, the central part around zero frequency is strongly enhanced. This central feature is often referred to as the Rayleigh line and arises from entropy (temperature) fluctuations at constant pressure [241]. The occurrence of this diffusive mode is directly caused by the inclusion of the random force term, $\boldsymbol{G}_i$, in the Langevin approach.

It is obvious that selecting the correct value of σ is crucial in order to obtain accurate results. We initially used a value of $\sigma = 6 \times 10^{13}\,\mathrm{s}^{-1}$ from ref. [240], that has been calculated using the Rayleigh model [242]. In the Rayleigh model, a heavy particle of mass, M, is immersed in an ideal gas of molecules of mass $m \ll M$, and

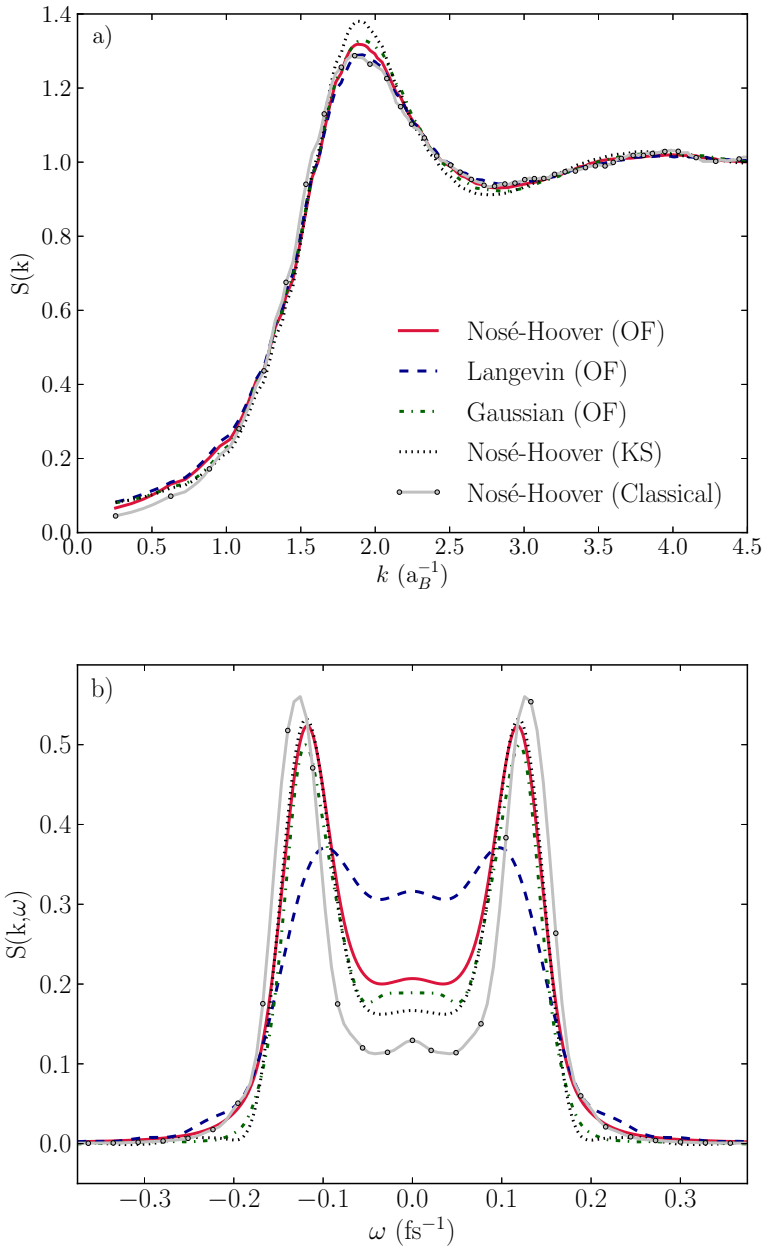

Figure 5.3: Static and dynamic structure factors of warm dense aluminium. (a) The ion-ion static structure factor. (b) The ion-ion dynamic structure factor at $k = 0.51$ a_B^{-1}. The structure factors ($T_e = T_i = 3.5$ eV and $\rho = 5.2$ g cm^{-3}) are calculated from orbital free simulations in a canonical ensemble with a Nosé-Hoover, Langevin and Gaussian thermostat. The Langevin thermostat uses a collision induced friction, σ, of 6 x 10^{13} s^{-1}. Results from a Kohn-Sham density functional theory simulation and a fully classical simulation using a screened Coulomb potential with an added short-range repulsion, both in a canonical ensemble with a Nosé-Hoover thermostat, are also included.

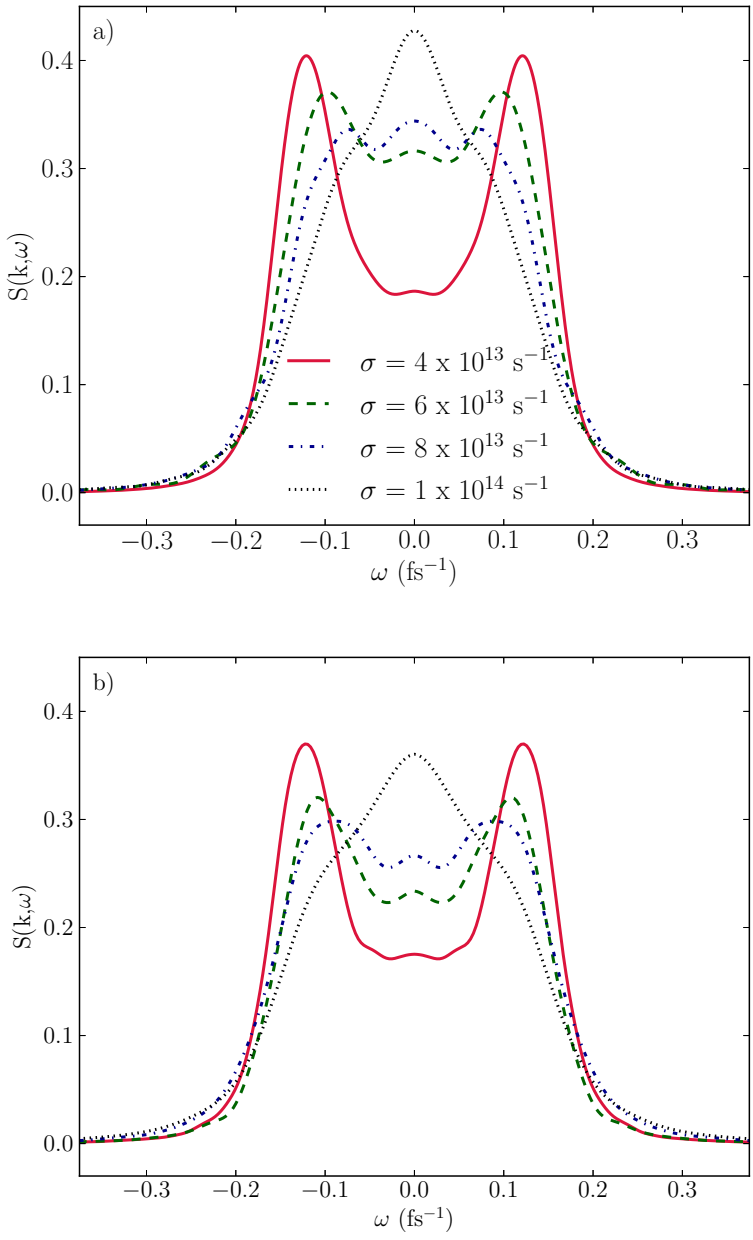

Figure 5.4: Sensitivity of the dynamic ion-ion structure factor on the Langevin friction parameter, σ. Data were obtained from orbital free simulations (a) and fully classical simulations (b) for warm dense aluminium at $T_e = T_i = 3.5$ eV and $\rho = 5.2$ g cm^{-3}. The classical and orbital-free approaches both exhibit the same trend; that is, the central Rayleigh line dominates the acoustic peaks at the largest value of σ considered, whereas the central peak disappears altogether at lower values.

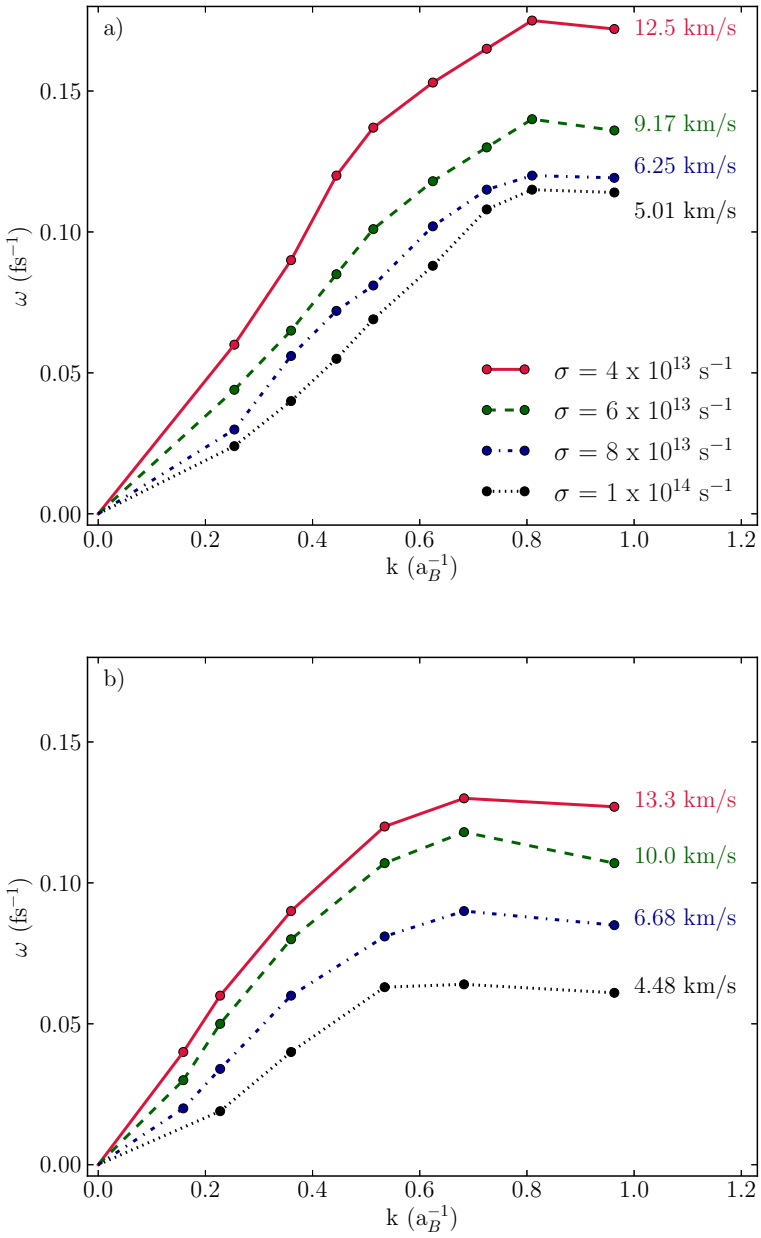

Figure 5.5: Dispersion relations of the ion acoustic modes for warm dense aluminium with varying friction values. a) shows data from orbtial free simulations, whereas b) shows data from fully classical simulations. Both were run in the canonical ensemble at $T_e = T_i = 3.5$ eV and $\rho = 5.2$ g cm^{-3}, employing a Langevin thermostat with different friction values, σ. Annotated numbers show the sound speeds of the ion acoustic waves in the system, obtained from the constant gradient at small wavenumbers, k.

interacts with them through instantaneous elastic collisions. The gas is assumed to be so rarefied that collisions of its molecules with the particle do not affect the distribution of incident molecules, and also re-collisions can be neglected. The value of σ was then varied to investigate the sensitivity of the mode structure on the value of the collision induced friction.

Figure 5.4 demonstrates that the central peak dominates the acoustic peaks at the largest σ considered, whereas the central peak disappears altogether at lower values. In the latter case, the DSF simply reduces to that produced by either of the conventional thermostats, suggesting that the effects of electron-ion dynamics are negligible in this scenario. The different considered values of σ here span the transition region from a highly diffusive system to one dominated by acoustic modes. One can consider the value of σ here as the importance of dynamical electron-ion effects on the system. Therefore the calculations here show the case where these effects are unimportant (low σ) and the intensity of the acoustic modes is much higher than that of the central peak (acoustic mode dominated), through to the highly diffusive case, where these effects strongly affect the dynamics of the system and the intensity of the central peak is much higher than those of the acoustic modes (high σ). It should also be noted that the corresponding SSFs for each friction value remain the same, as expected.

We also see that the sound speed of the system is significantly modified by the collision induced friction value within Langevin dynamics. Figure 5.5 displays the respective dispersion relations for the acoustic peaks explicitly. Moreover, it shows that this trend can be found in both quantum simulations of coupled electron-ion systems and classical simulations of the effective ionic systems. This shows that the trend is not related to the inter-ionic potentials used for the simulation, or a lack of including

quantum effects, but rather the collision induced friction included in Langevin dynamics. It is also very clear that the commonly used expression for the sound speed in a classical, low density plasma does not hold. The relation is typically written as,

$$v_s = \sqrt{\frac{\gamma_e Z^* k_B T_e + \gamma_i k_B T_i}{m_i}} \ , \tag{5.16}$$

where $\gamma_{e,i}$ represent the ratio of specific heat capacities for the electrons and the ion species respectively. The relation shows that the sound speed, and hence also the ion acoustic peak position, ought to be solely dependent on temperature. In dense plasmas, the approximation made in deriving this expression, that collisions are unimportant, does not hold. Indeed, the simulations show that increased electron-ion collisional effects decrease the sound speed. Appendix A shows the change in the dynamic structure of warm dense aluminium across a range of temperatures and densities in this regime. Here, one also observes that the density of the system affects the sound speed thus providing further evidence that equation 5.16 is not appropriate for systems in the WDM state.

Since the simulations are very sensitive to the choice of σ within the range of predicted values, taking the correct value is essential to predict the dynamic ion properties. Besides the DSF, large effects can be expected for particle diffusion, and energy transfer between species. Measurements have found discrepancies between various predictions for the time scale of electron-ion equilibration [59, 138, 243]. Moreover, this choice may impact on the calculated value of transport properties like the stopping power, a parameter that can provide an alternate experimental verification of the method [63]. Although a theoretical prediction of the most appropriate value of the collision induced friction proves to be relatively difficult, the relation of the DSF to the scattering spectrum of X-ray photons can be used to determine its value.

The physical meaning of the third term in the Langevin equation is not uniquely defined. This approach has been implemented, for example, in the field of dusty plasmas to mimic the effects of neutral species, showing significant changes in both the diffusion constant [237, 238] and the intermediate scattering function [239]. For dense ionised matter, electron-ion collisions have long been discussed as an additional source of ionic energy fluctuations. This type of matter can be seen as classical ions embedded in a background of an degenerate electron fluid. Examples of implementations are numerous: refs. [244, 245] proposed applying a damping force to the ions to mimic electron-ion interactions in MD simulations, a stochastic force was included to represent the energy fed into the ionic system by the electrons [246], the authors of ref. [247] noted that electrons could act as a heat sink or a heat bath, depending on the various timescales of the system.

Once one identifies the random force with dynamic electron-ion collisions, the changes in the DSF we report here also allow for assessing the strength of such collisions determining many transport and relaxation phenomena, a long standing problem in the WDM regime.

5.5.2 Sum rules

Before concluding this chapter, it is necessary to check the quality of the simulations in order to assure their results are valid. One method of assessing the validity of the dynamic structure factors calculated from simulations, or indeed any approximate analytical theory, involves invoking the sum rules [248]. The first of these is simply a definition of the static structure factor,

$$\int_{-\infty}^{\infty} S(k,\omega)d\omega = NS(k) \ , \tag{5.17}$$

k values (Å^{-1})	**1.0**	**1.3**	**1.5**	**1.7**	**1.9**
OF-DFT Langevin ($\sigma = 4 \times 10^{13}\,\text{s}^{-1}$)	0.17	0.20	0.18	0.06	0.01
OF-DFT Langevin ($\sigma = 6 \times 10^{13}\,\text{s}^{-1}$)	0.22	0.07	0.12	0.10	0.11
OF-DFT Langevin ($\sigma = 8 \times 10^{13}\,\text{s}^{-1}$)	0.18	0.21	0.19	0.23	0.19
OF-DFT Langevin ($\sigma = 1 \times 10^{14}\,\text{s}^{-1}$)	0.35	0.26	0.26	0.28	0.25
OF-DFT Nosé-Hoover	0.47	0.73	0.12	0.10	1.62
OF-DFT Gaussian	0.12	0.13	0.13	0.12	0.16
Classical Langevin ($\sigma = 4 \times 10^{13}\,\text{s}^{-1}$)	0.58	0.45	0.68	0.61	0.77
Classical Langevin ($\sigma = 6 \times 10^{13}\,\text{s}^{-1}$)	0.70	0.61	0.71	0.67	1.02
Classical Langevin ($\sigma = 8 \times 10^{13}\,\text{s}^{-1}$)	0.21	0.75	0.78	0.91	1.00
Classical Langevin ($\sigma = 1 \times 10^{14}\,\text{s}^{-1}$)	1.12	0.83	0.85	1.18	1.04
Classical Nosé-Hoover	0.67	0.51	0.79	0.78	1.02
KS-DFT Nosé-Hoover	0.30	0.72	0.20	0.15	0.22

Table 5.1: Comparison of percentage errors between left hand side and right hand side of first sum rule (equation 5.17). Headings in bold along the top indicate at which k value, in Å^{-1}, the errors were calculated, while headings in bold along the left indicate which simulation method was used, including the Langevin friction parameter, where applicable. The lowest and highest errors calculated are highlighted in green and red respectively.

where N is the total number of particles. The second sum rule, also known as the f-sum rule is a direct consequence of particle conservation in the system and represents a statement of the conservation law. It is obtained by taking the first moment of the dynamic structure factor,

$$\int_{-\infty}^{\infty} \omega S(k,\omega) d\omega = \frac{Nk^2}{2m} \quad . \tag{5.18}$$

Together these two sum rules are used to assess the quality of the structure factors calculated from the simulations. The percentage error between the left hand side and the right hand side of equation 5.17 for all simulations at numerous k values is shown in table 5.1. The highest error calculated here is 1.62 %, with the mean being only 0.44 %.

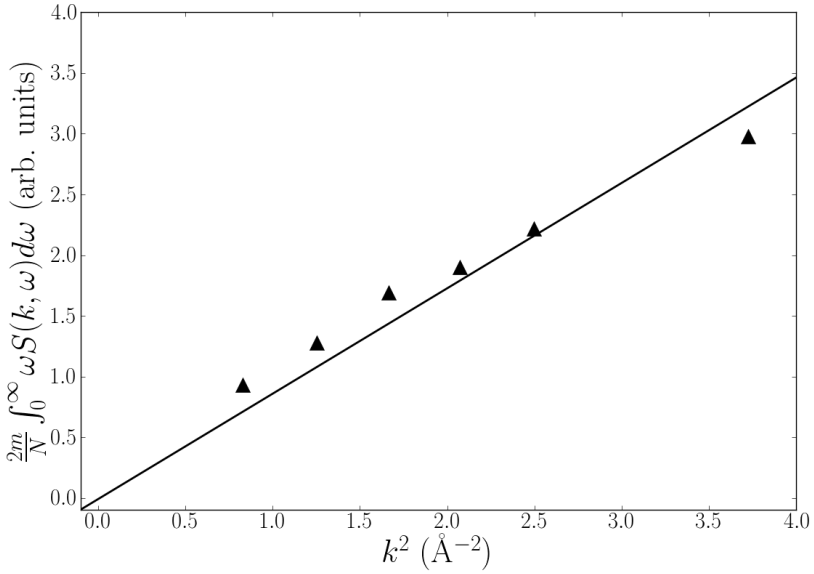

Figure 5.6: The first moment of the dynamic structure factor, calculated from the orbital free simulations employing Langevin dynamics with a collision induced friction of $\sigma = 4 \times 10^{13}\,\mathrm{s}^{-1}$, is plotted against k^2, with a linear dependence expected. A linear regression line is subsequently fit to the data at different k points using the method of least squares. The regression line is forced to pass through the origin as predicted by equation 5.18. Good correlation is observed, implying the second sum rule (equation 5.18), is observed.

The degree to which the second sum rule (equation 5.18) holds within the simulations can be displayed graphically by plotting the left hand side of the equation against k^2. This has been done for the example of the OF-DFT simulation applying Langevin dynamics with a collision induced friction of $\sigma = 4 \times 10^{13}\,\mathrm{s}^{-1}$, and is shown in figure 5.6. There is a linear dependence between the first moment of the structure factor and k^2, clearly demonstrated by the applied least squares fit regression line. The R^2 coefficient of this fit describes the degree to which the data fall on a straight line, hence measuring how well the sum rule holds and therefore the quality of the simulations. For the case, shown in figure 5.6 this value is 0.992. This method is applied to all simulations, with the R^2 values from each simulation method being

Simulation Method	R^2 value
OF-DFT Langevin ($\sigma = 4 \times 10^{13}\,\mathrm{s}^{-1}$)	0.96
OF-DFT Langevin ($\sigma = 6 \times 10^{13}\,\mathrm{s}^{-1}$)	0.96
OF-DFT Langevin ($\sigma = 8 \times 10^{13}\,\mathrm{s}^{-1}$)	0.95
OF-DFT Langevin ($\sigma = 1 \times 10^{14}\,\mathrm{s}^{-1}$)	0.96
OF-DFT Nosé-Hoover	0.96
OF-DFT Gaussian	0.96
Classical Langevin ($\sigma = 4 \times 10^{13}\,\mathrm{s}^{-1}$)	0.96
Classical Langevin ($\sigma = 6 \times 10^{13}\,\mathrm{s}^{-1}$)	0.96
Classical Langevin ($\sigma = 8 \times 10^{13}\,\mathrm{s}^{-1}$)	0.97
Classical Langevin ($\sigma = 1 \times 10^{14}\,\mathrm{s}^{-1}$)	0.96
Classical Nosé-Hoover	0.95
KS-DFT Nosé-Hoover	0.96

Table 5.2: The degree to which each simulation adheres to the second sum rule (equation 5.18). The first moment of the dynamic structure factor is plotted against k^2, with a linear dependence expected. A linear regression line is subsequently fit to the data at different k points using the method of least squares. The regression line is forced to pass through the origin as predicted by equation 5.18. The R^2 coefficient of this regression line is plotted against simulation method. A higher value subsequently corresponds to a better quality simulation; the highest values are highlighted in green and the lowest in red.

displayed in table 5.2. For both sum rules, no correlation is found between the simulation method and the associated error.

5.6 Conclusions

Our results demonstrate the importance of properly including all effects randomising the ionic motion when considering dynamic properties with MD simulations in the WDM regime. Significant changes arise for systems with strong damping, where a strong diffusive peak can be found in the DSF. Moreover, the strength and dispersion

of the ion acoustic peaks change, which in turn is associated with changes in the diffusivity and other transport coefficients. While these effects, could, to some extent, be predicted by the theory of electromagnetic fluctuations in plasmas [249, 250] or by considering other simpler damped oscillatory systems, this work represents the first time they have been observed in in classical MD as well as orbital free DFT-MD simulations of dense plasmas. We have clearly demonstrated that standard *ab initio* simulations employing the Born-Oppenheimer approximation and the conventional Gaussian or Nosé-Hoover thermostats should only be used to obtain static properties like the equation of state. To assess the dynamics of the ionic system a proper description of all interactions within the system is required. The work also illustrates the wealth of information contained in the dynamic ion structure and the difficulties of modelling this quantity with the same accuracy and predictive power as with *ab initio* simulations of static or thermodynamic properties of warm dense matter.

Chapter 6

Determining the dynamic structure factor analytically and experimentally

Chapter 5 introduced the idea of employing a Langevin approach in the context of molecular dynamics simulations for calculating the dynamic structure factor of dense plasmas. This chapter describes an experiment carried out at the Linac Coherent Light Source, one of the world's leading free electron lasers, with the goal of measuring the ionic part of the DSF experimentally. The experimental data are used to evaluate the extent to which dissipative processes, such as electron-ion collisions, included in Langevin dynamics, are important in the WDM regime. An alternative approach to calculate the DSF analytically by using hydrodynamic theory is also introduced, and this simple approach is compared to the more time-consuming molecular dynamics methods.

6.1 Experimental method

The Linac Coherent Light Source (LCLS), based at Stanford University, California is a free electron laser (or FEL, see section 2.4) that has one of the highest X-ray

brilliances of any in current operation [251]. Coupled with its very low bandwidth of $\sim$ 1 eV, the LCLS is the only location capable of measuring ion acoustic waves in warm dense matter, at the current time.

The experimental setup itself, shown in figure 6.1, was quite straightforward. Two 5 J, 3 ns, optical lasers were focused to a spotsize of 50 µm onto a target to create two converging shocks. The target was made of aluminium with a thickness of 50 µm. Both sides of the target were coated with a 2 µm thick layer of plastic to act as a tamper for the shock [87]. The laser pulses were given a spatial top-hat profile through the use of continuous phase plates. The predicted convergence time of the two shock-waves was determined to be 1.5 ns, using the simple commercially available 1-D hydrodynamic code, Helios [252]. Although such codes are known to slightly over-estimate shock speeds, this timescale was used as an estimate to enable the true shock convergence time to be determined. The X-ray beam was delayed with respect to the optical lasers by 2 ns and was focused by a beryllium compound refractive lens to a spotsize of several microns. The X-ray spot was positioned at the centre of the much larger heated region, ensuring that no cold unheated matter was probed during the experiment. The X-ray beam contained 10^{12} photons of energy 8 keV, with a spectral resolution of $\Delta E/E = 10^{-4}$ and a temporal resolution of approximately 50 fs [253]. This spectral bandwidth, however, was still too large to able to resolve ion waves in the scattered spectrum. Therefore, the bandwidth of the beam had to be reduced further using a high resolution crystal monochromator, used at a Bragg angle near 90°, with the narrow rocking curve of the crystal enabling the bandwidth to be reduced down to $\sim$ 50 meV. The drawback of using the monochromator, was that the number of X-ray photons incident on the target was reduced by approximately an order of magnitude. Coupled with the very low cross section for Thomson scattering, it was necessary to use a large area detector in order obtain a sufficiently high X-ray

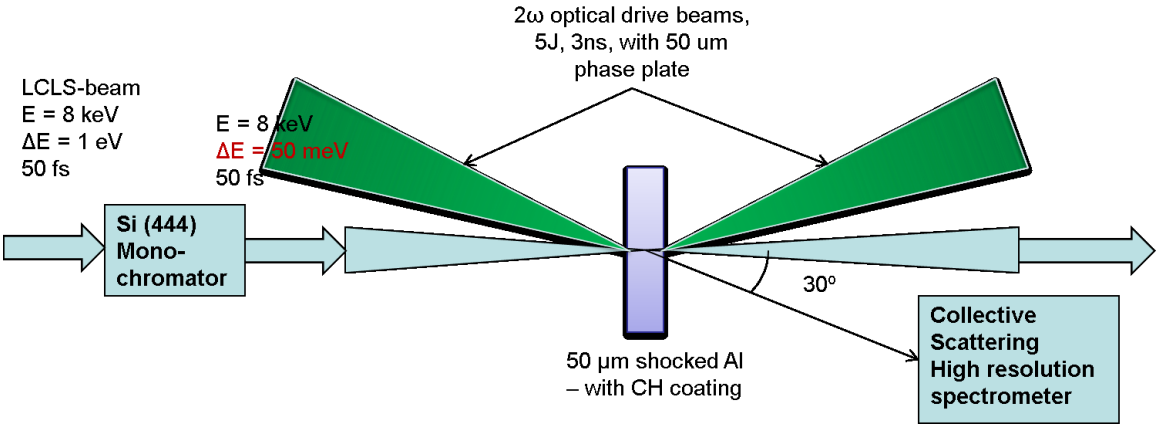

Figure 6.1: Schematic of the experimental set-up at LCLS Two long-pulse optical lasers, working at 532 nm with 5 J of energy and a pulse length of 3 ns, are focused to a spot size of 50 µm diameter onto an aluminium target coated with a plastic tamper. The seeded X-ray beam is delayed with respect to the optical beam and passed through monochromator to reduce the bandwidth of the incoming X-rays, before being incident onto the sample. The scattered X-rays are collected by a high resolution crystal spectrometer. Image reproduced from ref [185].

signal. This approach caused an increased k-vector blurring, arising from the fact that collected scattered X-rays came from a large spread of scattering angles. A spherical diced crystal was placed 1 m away from the aluminium sample and the detector as shown in figure 6.2 [254]. As the maximum bandwidth that could be measured in any given shot was 300 meV, it was necessary to rotate the crystal through the X-ray axis to cover both the upshifted and downshifted parts of the spectra, with the two halves being combined in post-processing. The instrumentation function was determined by scattering from a cold plastic target at the sample location and integrating over 5000 shots. The total instrumentation function of this setup was found to be $\sim$ 100 meV, and thus was small enough to expect the resolution of the ion acoustic peaks to be possible.

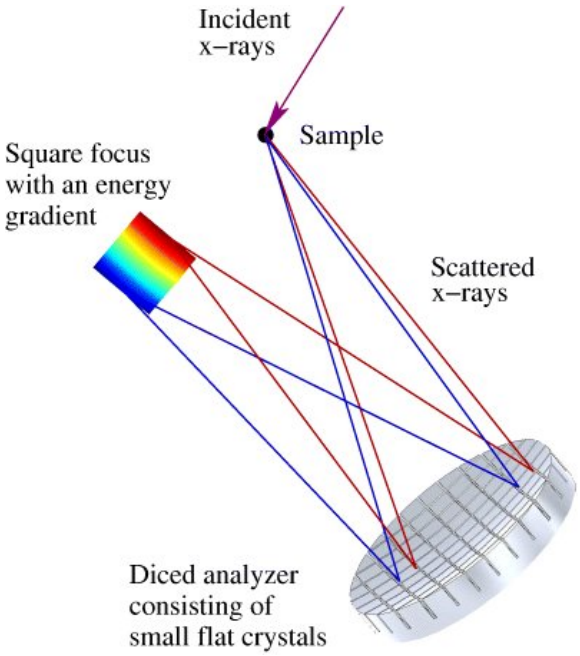

Figure 6.2: The diced crystal analyzer projects a point source into a square which is an image of an individual dice magnified by a factor of two. Due to an energy gradient within the focus, it is possible to measure the photon energy using the information on its position. Image reproduced from ref [254].

6.2 Experimental results

The collected spectrum is displayed in figure 6.3. It is plotted against change in photon energy, with zero indicating the energy of the incident X-ray beam. The intensity scale on the y-axis contains arbitray units as the detector was not absolutely calibrated. The spectrum represents the summation of sixteen individual shots, each reaching the same plasma conditions. Eight of these contained the upshifted and eight contained the downshifted parts of the spectra, with the two being combined to give the final result. The two ion acoustic peaks, seen at $\pm$ 150 meV, represent the first such measurement in the warm dense matter regime. These data therefore provide an excellent opportunity to assess the Langevin model, described in the previous chapter. Without such data, it would not be possible to determine whether dynamic electron-ion effects are important in WDM, and hence the extent to which

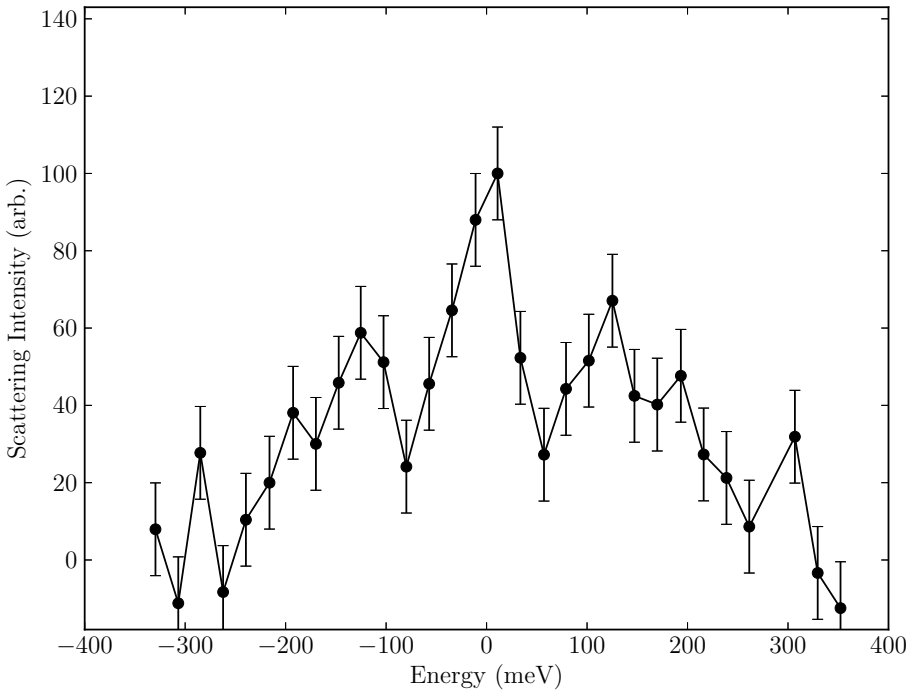

Figure 6.3: Energy resolved scattered X-rays for warm dense aluminium, measured using the diced crystal analyser. The two halves of the spectrum were measured independently and then stitched together in post-processing.

conventional simulation techniques must be improved upon. The importance of this data set should therefore not be under-estimated.

6.2.1 Analysis with molecular dynamics

The scattered spectrum was compared to the dynamic structure factor predicted by the orbital free molecular dynamics technique described in chapter 5. The data are used to determine whether dissipative processes, such as dynamical electron-ion interactions, are important in WDM. Simulations were run using the conventional Nosé-Hoover approach as well as with the Langevin method, described in chapter 5. However, the plasma conditions were not measured experimentally on each shot. The temperature and density, necessary inputs for the simulations, were therefore taken from the hydrodynamic predictions, giving 5 eV and 7 g cm^{-3}. Although there are

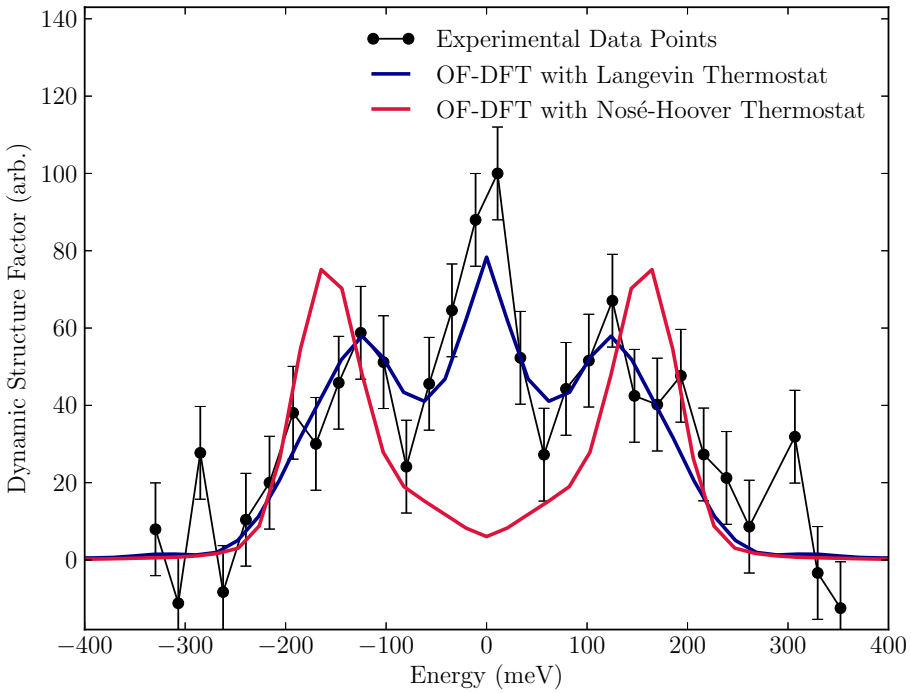

Figure 6.4: A comparison between the inelastic scattering data obtained from the LCLS scattering experiment and the dynamic structure factor for aluminium at a temperature of 5 eV and a density of 7 g cm^{-3}, taken at the corresponding k point. Results from orbtial-free density functional theory employing Langevin dynamics as well as a Nosé-Hoover thermostat are shown. The simulated structure factors have been scaled to match the experimental data.

doubts surrounding the validity of 1-D hydrodynamic simulations, there is good reason to trust them in this case. Firstly, a similar experiment using identical laser parameters and targets was performed at the facility two months prior to this one, determined the conditions reached to be 2 eV and 6.3 g cm^3 [99]. Although these conditions differ slightly from those assumed here, they do fall within reasonable limits of error. Secondly, the simulations themselves are quite sensitive to both temperature and density. In particular, the simulation results are a good match to the position of the ion acoustic peaks, which are strongly dependent on density (see Appendix A for further details). The friction parameter in the Langevin method was varied in order to find the best fit to the experimental data, with a value of $\sigma = 1.2 \times 10^{14}\,\mathrm{s}^{-1}$ found

to be the most appropriate.

Because the ion dynamics in the simulations are treated purely classically, the principal of detailed balance is not included. This phenomenon, already observed in plasmon peaks in the dynamic structure factor [91], causes the upshifted peak to be suppressed at lower temperatures. One can multiply the dynamic structure factor from the simulations by a prefactor, to take this effect into account,

$$S(k,\omega) \;\rightarrow\; \frac{\hbar\omega/k_B T_i}{1-\exp(\hbar\omega/k_B T_i)}\, S(k,\omega) \quad , \tag{6.1}$$

For the temperature of 5 eV considered here, however, this implies a ratio between the downshifted and upshifted peaks of 1.03. This is far too small to be noticeable in the data, given the size of the error bars, and hence detailed balance is ignored in this case. It should be noted though, that at lower temperatures (or higher peak separation), where the ratio in intensity between the two peaks would be expected to be larger, this approach could be used to estimate the temperature of the plasma. This method has been used successfully with electron plasmon peaks [89], but further experiments would be necessary to demonstrate its applicability to ion acoustic peaks.

6.2.2 Analysis with hydrodynamics

There has been a great deal of work in attempting to describe the DSF in a purely analytical manner. The benefit of a continuous approach such as this, rather than a molecular dynamics simulation, is obvious: the time required to make a calculation is drastically reduced. Moreover, the origin the shape of the DSF can be more easily related to particular properties of the system. The downside, however, is that many approximations must be made in order to treat the system analytically, particularly in the WDM regime. Two methods have achieved particular attention: memory functions [255, 256] and hydrodynamics [241], with the latter being the focus of this

section. As well as potentially providing a different insight into the origin of the central diffuse peak in the form of the DSF not seen in conventional MD simulations, hydrodynamics offers a route to gather information about many thermodynamic and transport coefficients.

It has been shown that a pure hydrodynamic approach is appropriate only for scattering vectors, k, less than 0.43λ [257]. For the plasma conditions here (7 g cm^{-3}, 5 eV, $Z^* = 1.5$), the screening length λ is calculated as ~ 2.14 Å^{-1} using the Thomas-Fermi approach described in section 2.1. Given the scattering vector in the experiment was 2.1 Å^{-1}, this gives a ratio of k/λ of around unity. A pure hydrodynamic approach in this case would thus not be suitable. Instead we use a generalised hydrodynamic model based on the Yukawa form of the potential, including the effects of the electrons on the ions through the use of a screening parameter. This method has been shown to be applicable over a much larger range of conditions compared with the pure hydrodynamic model [258].

The hydrodynamic prescription for the dynamic structure factor is obtained through the linearisation of the Navier-Stokes fluid equations, for the case of small fluctuations. There has been significant effort in recent times to provide a more complete picture of the DSF. Ref [259] extended the classical hydrodynamics formalism to include non-local quantum behavior via the phenomenological Bohm potential, while more recently ref [260] included radiative effects in both optically thick and thin fluids. The former approach describes the DSF as,

$$\begin{aligned}\frac{S(k,\omega)}{S(k)} = 2\pi\frac{\gamma-1}{\gamma}\frac{v_s^2k^2}{v_s^2k^2+\omega_{pscr}^2}\frac{2\epsilon_Q ak^2}{\omega^2+(\epsilon_Q ak^2)^2} \\ + \frac{\gamma^{-1}v_s^2k^2+\omega_{pscr}^2}{v_s^2k^2+\omega_{pscr}^2}\left[\frac{\Gamma k^2}{(\omega+c_q)^2+\Gamma^2k^4}+\frac{\Gamma k^2}{(\omega-c_q)^2+\Gamma^2k^4}\right].\end{aligned} \tag{6.2}$$

where γ is the ratio of specific heats, and all terms directly proportional to $\hbar^2/m^2$ have been ignored for the ions. Additionally we have the screened plasma frequency, ω_{pscr}, written as,

$$\omega_{pscr} = \omega_p \times \frac{k^2}{k^2 + \lambda^2} \quad . \tag{6.3}$$

The peak position, defined by c_q, is given as,

$$\omega_{pscr}^2 + v_s k^2 - \frac{\omega_p k^2}{\lambda^2} \quad . \tag{6.4}$$

Additionally, the width of the side peaks are related to ϵ_q,

$$\epsilon_q = (\omega_{pscr}^2 + \gamma^{-1} v_s^2 k^2)/c_q^2 \quad , \tag{6.5}$$

and Γ,

$$\Gamma = \frac{1}{2}[(1 - \epsilon_q)a + b] \quad , \tag{6.6}$$

where a is related to the thermal diffusivity, D_T, by,

$$a = D_T \gamma \quad , \tag{6.7}$$

and b is related to the shear viscosity, η, by,

$$b = \frac{4\eta}{3\rho} \quad , \tag{6.8}$$

where we have also assumed that the bulk viscosity is negligible [261]. The unknown thermodynamic and transport properties in the hydrodynamic form for the DSF (c_s, D_T, η and γ) are then allowed to vary in order to fit to the experimentally obtained data, with a non-linear least mean squares fitting algorithm being used. The results of the fitting procedure are shown in figure 6.5, with the corresponding values in table 6.1. The third column in the table displays values from the literature for these variables, taken from MD calculations based on classical Yukawa potentials. The strongest difference between the two approaches lies in the ratio of heat capac-

ities, γ. It is obvious from looking at equation 6.2, however, that a large value of γ corresponds to a more prominent middle diffuse peak. It should therefore come as no surprise that conventional MD simulations under-estimate this value compared to experimental data, given the discrepancy shown between data and conventional simulations shown in fig 6.4. Although none of these variables have been measured directly, this method of fitting to experimental data does give an estimate of their values in the warm dense matter regime. Further scattering experiments would be necessary to determine whether or not this approach is a feasible method of gathering such information about a system. In any case, due to the high number of fitting parameters, one could never hope to predict the form of the DSF before any scattering experiments are performed. Molecular dynamics simulations, particularly those based on density functional theory, have far fewer parameters to vary, and hence are more suitable for predicting experimental data. On the other hand, little is known about the viscosity and other transport coefficients in the warm dense matter regime and hence results such as these are nevertheless of significant value.

It is also instructive to include radiative effects in the hydrodynamic model in order determine whether or not these play an important role in this regime. The plasma in question here is an optically dense fluid, and hence the properties of the system are expected to be affected by the opacity, κ. We assume this takes the value of the Rosseland mean opacity [262], κ_R [m^2 kg^{-1}] $= 1.04 \times 10^7\ \rho^{0.48}\ T^{-2.48}$. Calculations performed using this opacity did not change the results shown in figure 6.5, where radiative effects were omitted. We therefore conclude that, at these temperatures, the omission of radiative effects is a good approximation. This is an important conclusion. The molecular dynamics simulations performed throughout this thesis all ignore these effects, and moreover, little work has been to include radiation in the context of MD throughout the WDM community in general. At temperatures above 25 eV,

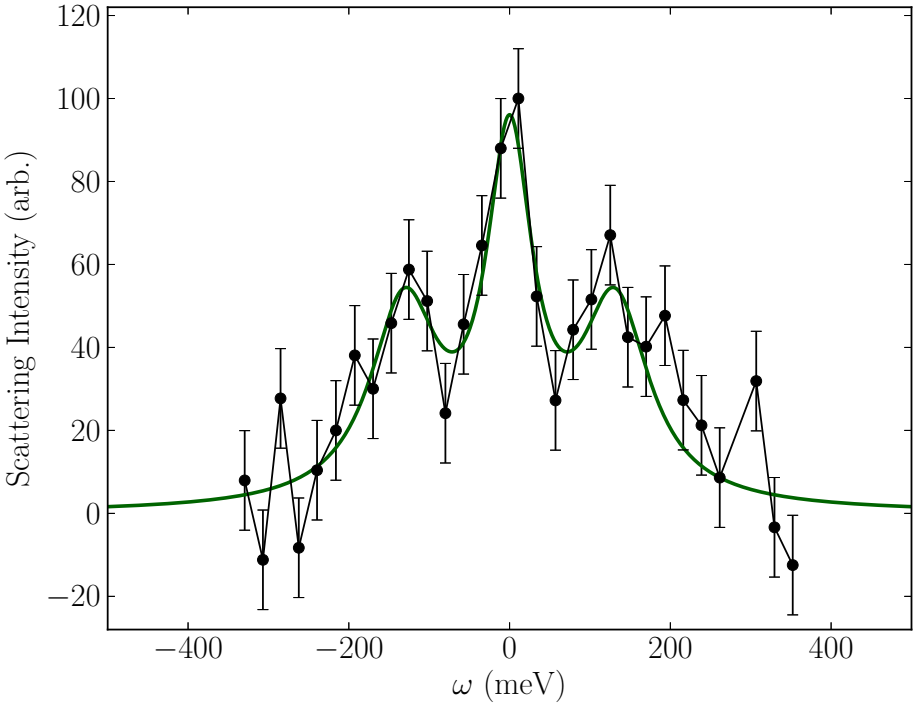

Figure 6.5: Fitting of the generalised hydrodynamic structure factor to scattering spectrum. The values of the fitting parameters are listed in table 6.1

on the other hand, radiative effects are predicted to become more important [260] and so one must treat results from any MD simulations at these temperatures some caution.

6.3 Conclusions

Results of an inelastic X-ray scattering experiment which was performed at the matter in extreme conditions end-station at the LCLS FEL have been shown. With this high resolution, the low frequency structural dynamics in warm dense matter were resolved for the first time. The data were compared to density functional theory molecular dynamics simulations based on conventional techniques as well as to the Langevin method, outlined in chapter 5. While the Nosé-Hoover thermostat failed to produce the central diffuse peak, seen in the experimental data, by selecting an

Variable	Fitted value	MD simulations
c_s (km s^1)	10.5 ± 1.5	9.67 [72]
D_T (m^2) s^{-1}	$1.2 \pm 0.4 \times 10^{-6}$	0.7×10^{-6} [263] 1.01×10^{-6} [264]
η (mPa s)	0.7 ± 0.3	2.97 [265] 1.16 [266]
γ (no units)	1.6 ± 0.3	1 [72]

Table 6.1: Parameters obtained from fitting the generalised hydrodynamic model to scattering data, compared to corresponding values, taken from the literature, based on classical molecular dynamics calculations. Errors on fitted values correspond to the 1-σ confidence interval.

appropriate friction value within the Langevin approach, good agreement between simulations and experimental data could be found.

The analytical hydrodynamic approach was also used to interpret the experimental data. Although there are several fitting parameters in this model, it is able to reproduce the data well. This method can be used to infer the values of the sound speed, the shear viscosity, the thermal diffusivity and the ratio of specific heats for the system. The measured values for these parameters were compared to previous calculations based on classical MD simulations with good agreement found in general, although a discrepancy was found in the heat capacity ratio, γ. This finding adds weight to the suggestion that a central peak ought to be present in the spectrum and is missing from conventional MD simulations.

More high resolution scattering experiments are necessary to validate both the molecular dynamics and the analytical models, with different scattering vectors or different temperature and density conditions being particularly useful.

Chapter 7

Conclusions

"There is a single light of science and to brighten it anywhere is to brighten it everywhere."

- *Isaac Asimov*, 1964 CE

This thesis has described three advances made in our understanding of the physics associated with the warm dense matter regime. This state of matter is found in planetary cores [13] and the crusts of neutron stars [14] as well as in inertial connement fusion experiments, where the deuterium-tritium capsule passes through the warm dense state en route to potential ignition in a hotter state. Better descriptions of this poorly understood state of matter are therefore the subject of great scientific interest.

Chapter 3 detailed an experiment that employs time-resolved X-ray scattering to directly measure temperature relaxation in a bulk sample after heating with an intense laser beam. These type of studies are important as they not only help with the understanding of experiments designed to create the WDM states, but also provide an insight into fundamental internal processes such as electron-ion coupling, which may contain a wealth of information about systems in the WDM regime. The value

obtained in this work for the electron-ion coupling rate in gold agrees with the reported data from a similar experiment where it was inferred by observing the shift in position of the peaks due to acoustic reverberation within the gold sample. Our analysis indicates that other factors may also determine the position of these peaks, which are not directly related to the energy relaxation time. The results displayed here may therefore give a more reliable estimate of the temperature relaxation time than previous studies. Our results confirm that the energy relaxation process in gold is a fast process in the bulk as well as on the surface of the sample. The work here opens up the possibility to study energy relaxation processes in such systems through large-scale MD simulations. This could be a particularly successful method at describing highly correlated systems where the complex ion-ion interactions renders experiments on this regime difficult to describe.

Chapter 4 showed the ability of X-ray polycapillary lenses to focus laser-produced X-ray sources to high intensities. The X-ray source used to probe high energy density states of matter must fulfill stringent requirements on photon number, bandwidth and divergence in single shot experiments. These requirements often necessitate a very small separation (a few mm) between the backlighter target used to produce X-rays and the main sample to be driven. This leads to signal-to-noise problems with detectors such as CCDs or image plates recording insufficient numbers of X-ray photons to make meaningful conclusions. In addition, the geometry of many pump-probe experiments is restricted due to the need to shield detectors sufficiently from background noise. The polycapillary lens enables the placement of the backlighter target at a much larger distance from the sample to be studied and greatly improves the signal-to-noise ratio. This is demonstrated by two simple diffraction experiments using pyrolytic graphite and polycrystalline aluminium. The diffracted He-α and He-β lines were seen with a good signal-to-noise ratio in both cases. Future experiments

to study high energy density states of matter could achieve better X-ray scattering or diffraction results using the setup described here.

Chapter 5 proposed the use of molecular dynamics simulations using a Langevin method as the most appropriate method of modelling matter in the WDM regime. Due to the inherent difficulties in modelling this type of matter, where classical long-range Coulomb forces dominate interactions between ions and electrons are partially to fully degenerate, current predictions of transport coefficients differ by many orders of magnitude. The prominent collective modes found in the dynamic structure factor serve as an important tool to validate theoretical predictions for WDM, with the recent advances in free electron laser technology allowing low frequency ion modes to be resolved for the first time. The results demonstrate the importance of properly including all effects that randomise the ionic motion when considering dynamic properties with MD simulations in the WDM regime. When using the Langevin method rather than conventional thermostats, significant changes arise for systems with strong damping, where a strong diffusive peak can be found in the DSF. Moreover, the strength and dispersion of the ion acoustic peaks change, which in turn is associated with changes in the diffusivity and other transport coefficients. The results have important implications for those looking to extract dynamic properties from molecular dynamics simulations in the WDM regime.

Chapter 6 compared the calculations of the DSF made in the previous chapter to inelastic X-ray scattering data from an experiment at the LCLS free-electron laser, where the low frequency structural dynamics in warm dense matter were resolved for the first time. While the Nosé-Hoover thermostat failed to produce the central diffuse peak seen in the experimental data, by selecting an appropriate friction value within the Langevin approach, good agreement between simulations and experimental data

could be found. A hydrodynamic approach was also used to interpret the experimental data. This method can be used to infer the values of the sound speed, the shear viscosity, the thermal diffusivity and the ratio of specific heats for the system. The measured values for these parameters were compared to previous calculations based on classical MD simulations with good agreement found in general, although a discrepancy was found in the heat capacity ratio, γ, adding weight to the suggestion that a central peak ought to be present in the spectrum and is indeed missing from MD simulations. More high resolution scattering experiments are necessary to validate both the molecular dynamics and the analytical models, with different scattering vectors or different, and more precisely measured, temperature and density conditions being particularly useful.

7.1 Future work

There are various strands of research which would naturally follow on from the work presented in this thesis. Broadly speaking, they fit into three categories:

- The use of X-ray optics to perform future pump-probe experiments in high energy density physics. The technique outlined in this work could be applied to any laser generated X-ray source with little difficulty. Moreover, one could even separate the collimating and the focusing parts of the X-ray optic, thus vastly increasing the distance between the X-ray source and the sample, or, alternatively, using two different target chambers entirely. This technique could equally be applied to any experiments suggested in the following two bullet points as well.

- The modelling of bulk, out-of-equilibrium samples through the use of large scale molecular dynamics simulations. Here we have used this technique to determine electron-ion coupling rates, yet there are a wealth of other material properties

that may be extracted from such MD simulations, such as transport or optical properties.

- It has been shown that dynamical electron-ion effects are important in the WDM regime. Here, we have proposed Langevin dynamics as way of randomising ion motion in order to model this, although there are other methods available. With increasingly advanced computers, one may soon be able to go beyond the Born-Oppenheimer approximation and include fully dynamical electrons. Whether this is best done by discarding the Chihara approximation, through the use of TD-DFT or Ehrenfest dynamics, or by using another method entirely, such as path integral Monte Carlo is, as of yet, unknown. Moreover, at higher temperatures, one must also begin to include the effects of radiation in the simulations. Further scattering experiments looking at low frequency structural dynamics of matter in the WDM regime are also becoming increasingly necessary in order to test the various models and therefore differentiate between them.

Appendix A

Dynamic structure factor calculations

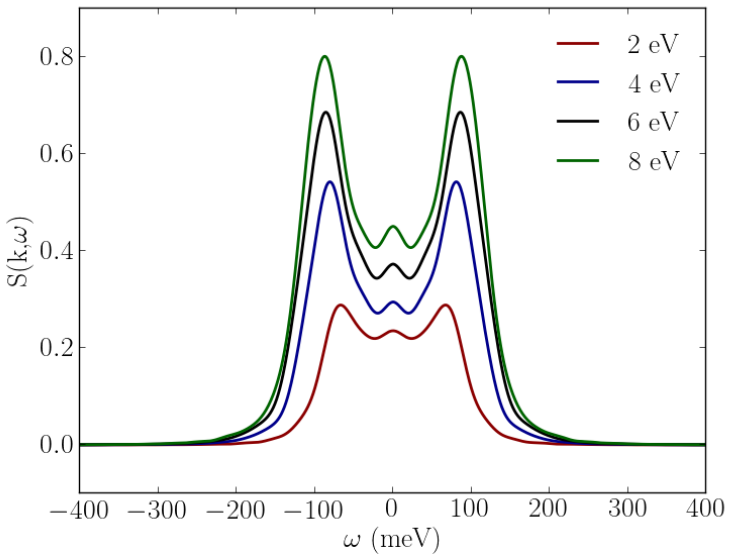

Figure A.1: The ion-ion dynamic structure factor for warm dense aluminium at $k = 0.92$ Å^{-1} and twice solid density (5.4 g cm^{-3}) for various temperatures. Simulations were run in ABINIT using the orbital free method, employing Langevin dynamics. The friction coefficient, σ, of 1.2×10^{14} s^{-1}, was taken from the best fit to the data in chapter 6. The k value was selected to best demonstrate the trend with temperature.

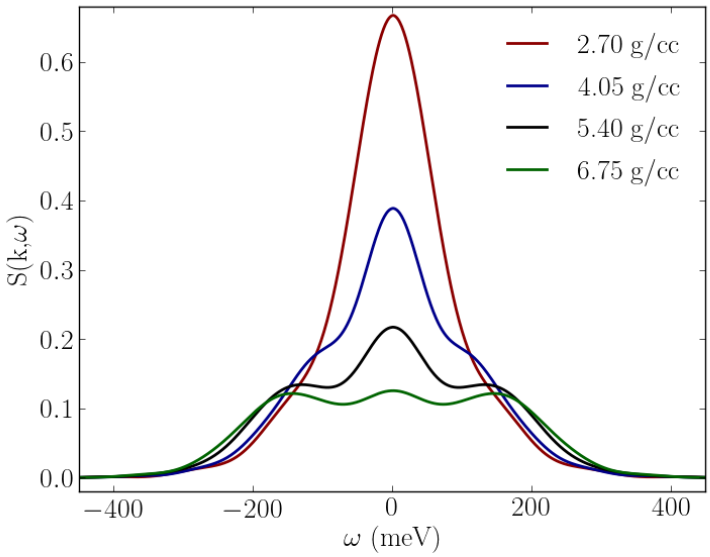

Figure A.2: The ion-ion dynamic structure factor for warm dense aluminium at $k = 1.6$ Å^{-1} and 4 eV for various densities. Simulations were run in ABINIT using the orbital free method, employing Langevin dynamics. The friction coefficient, σ, of $1.2 \times {}^{14}$ s^{-1}, was taken from the best fit to the data in chapter 6. The k value was selected to best demonstrate the trend with density.

This section shows the variation of the dynamic structure factor with both temperature and density. The whole curve increases in amplitude with temperature, due to a broadening out of the static structure factor, from a more structured system towards the ideal gas limit. The ion mode separation also increases with temperature, as equation 5.16 predicts. However, the ion modes also move out at higher densities, an effect not accounted for when collisions are ignored, such as in equation 5.16. Additionally, the strength of the central diffusive peak decreases with increasing density; the range considered here spans from solid density (2.7 g cm^{-3}) to 2.5 times compressed (6.75 g cm^{-3}).

Appendix B

List of publications

- T. G. White, **P. Mabey**, D. O. Gericke, N. J. Hartley, H. W. Doyle, D. McGonegle, D. Rackstraw, A. Higginbotham and G. Gregori. Electron-phonon equilibration in laser heated gold films. *Physical Review B*, 90:01345, 2014.
- **P. Mabey**, N.J. Hartley, H.W. Doyle, J.E. Cross, L. Ceurvorst, A. Savin, A. Rigby, M. Oliver, M. Calvert, I.J. Kim, D. Riley, P.A. Norreys, C.H. Nam, D.C. Carroll, C. Spindloe and G. Gregori. Characterization of X-ray lens for use in probing high energy density states of matter. *Journal of Instrumentation*, 10:04010, 2015.
- J. E. Cross, **P. Mabey**, D. O. Gericke and G. Gregori. Theory of density fluctuations in strongly radiative plasmas. *Physical Review E*, 93:033201, 2016.
- **P. Mabey**, S. Richardson, T. G. White, L. B. Fletcher, S. H. Glenzer, N. J. Hartley, J. Vorberger, D. O. Gericke, G. Gregori. A strong diffusive ion mode in dense ionised matter predicted by Langevin dynamics. *Nature Communications*, 8:14125, 2017.
- N. J. Hartley, N. Ozaki, T. Matsuoka, B. Albertazzi, A. Faenov, Y. Fujimoto, H. Habara, M. Harmand, Y. Inubushi, T. Katayama, M. Koenig, A. Krygier, **P. Mabey**, Y. Matsumura, S. Matsuyama, E. McBride, K. Miyanishi, G. Morard, T. Okuchi, T. Pikuz, O. Sakata, Y. Sano, T. Sato, T. Sekine, Y. Seto, K. Takahashi, K. A. Tanaka, Y. Tange, T. Togashi, Y. Umeda, T. Vinci, M. Yabashi, T. Yabuuchi, K. Yamauchi, and R. Kodama. Ultrafast Lattice Dynamics in Laser-Irradiated Gold Foils. Submitted to *Applied Physics Letters*, 110:071905 2017

Bibliography

[1] T. G. White, P. Mabey, D. O. Gericke, N. J. Hartley, H. W. Doyle, D. McGonegle, D. S. Rackstraw, A. Higginbotham, and G. Gregori. Electron-phonon equilibration in laser-heated gold films. *Physical Review B*, 90:014305, 2014.

[2] P. Mabey, N. J. Hartley, H. W. Doyle, J. E. Cross, L. Ceurvorst, A. Savin, A. Rigby, M. Oliver, M. Calvert, I. J. Kim, et al. Characterization of X-ray lens for use in probing high energy density states of matter. *Journal of Instrumentation*, 10(04):P04010, 2015.

[3] P. Mabey, S. Richardson, T. G. White, L. B. Fletcher, S. H. Glenzer, N. J. Hartley, J. Vorberger, D. O. Gericke, and G. Gregori. A strong diffusive ion mode in dense ionized matter predicted by langevin dynamics. *Nature Communications*, 8:14125, 2017.

[4] P. Melchior. *The physics of the earth's core: an introduction*. Elsevier, 2013.

[5] M. Schwarzschild. *Structure and evolution of stars*. Princeton University Press, 2015.

[6] T. Guillot. Interiors of giant planets inside and outside the solar system. *Science*, 286:72, 1999.

[7] S. Chandrasekhar. *The mathematical theory of black holes*. Oxford University Press, 1998.

[8] J. M. Lattimer and M. Prakash. The physics of neutron stars. *Science*, 304:536, 2004.

[9] R. P. Drake. *High energy density physics: fundamentals, inertial fusion, and experimental astrophysics*. Springer Science & Business Media, 2006.

[10] F. Graziani, M. P. Desjarlais, R. Redmer, and S. B Trickey. *Frontiers and challenges in warm dense matter*. Springer Science & Business Media, 2014.

[11] Plasma Science Committee et al. *Frontiers in high energy density physics: The X-games of contemporary science*. National Academies Press, 2003.

[12] S. Ichimaru. Strongly coupled plasmas: high-density classical plasmas and degenerate electron liquids. *Reviews of Modern Physics*, 54:1017, 1982.

[13] J. Daligault and S. Gupta. Electron-ion scattering in dense multi-component plasmas: application to the outer crust of an accreting neutron atar. *The Astrophysical Journal*, 703:994, 2009.

[14] J. Dai, Y. Hou, D. Kang, H. Sun, J. Wu, and J. Yuan. Structure, equation of state, diffusion and viscosity of warm dense Fe under the conditions of a giant planet core. *New Journal of Physics*, 15:045003, 2013.

[15] J. Schneider, C. Dedieu, P. Le Sidaner, R. Savalle, and I. Zolotukhin. Defining and cataloging exoplanets: the exoplanet.eu database. *Astronomy & Astrophysics*, 532:A79, 2011.

[16] M. Koenig, A. Benuzzi-Mounaix, A. Ravasio, T. Vinci, N. Ozaki, S. Lepape, D. Batani, G. Huser, T. Hall, D. Hicks, A. MacKinnon, P. Patel, H. S. Park, T. Boehly, M. Borghesi, S. Kar, and L. Romagnani. Progress in the study of warm dense matter. *Plasma Physics and Controlled Fusion*, 47(12B):B441, 2005.

[17] M. K. Matzen, M. A. Sweeney, R. G. Adams, J. R. Asay, J. E. Bailey, G. R. Bennett, D. E. Bliss, D. D. Bloomquist, T. A. Brunner, R. B. Campbell, et al. Pulsed-power-driven high energy density physics and inertial confinement fusion research. *Physics of Plasmas*, 12(5):055503, 2005.

[18] R. Betti and O. A. Hurricane. Inertial-confinement fusion with lasers. *Nature Physics*, 12(5):435, 2016.

[19] T. Ditmire. High-power lasers. *American Scientist*, 98:394, 2010.

[20] T. H. Maiman, R. H. Hoskins, I. J. d'Haenens, C. K. Asawa, and V. Evtuhov. Stimulated optical emission in fluorescent solids. II. spectroscopy and stimulated emission in ruby. *Physical Review*, 123(4):1151, 1961.

[21] H. W. Mocker and R. J. Collins. Mode competition and self-locking effects in a q-switched ruby laser. *Applied Physics Letters*, 7(10):270, 1965.

[22] F. J. McClung and R. W. Hellwarth. Giant optical pulsations from ruby. *Journal of Applied Physics*, 33(3):828, 1962.

[23] M. Pessot, P. Maine, and G. Mourou. 1000 times expansion/compression of optical pulses for chirped pulse amplification. *Optics Communications*, 62(6):419, 1987.

[24] D. Strickland and G. Mourou. Compression of amplified chirped optical pulses. *Optics Communications*, 56(3):219, 1985.

[25] D. Speck, E. Bliss, J. Glaze, J. Herris, F. Holloway, J. Hunt, B. Johnson, D. Kuizenga, R. Ozarski, H. Patton, et al. The Shiva laser-fusion facility. *IEEE Journal of Quantum Electronics*, 17(9):1599, 1981.

[26] T. R. Boehly, R. L McCrory, C. P. Verdon, W. Seka, S. J. Loucks, A. Babushkin, R. E. Bahr, R. Boni, D. K. Bradley, R. S. Craxton, et al. Inertial confinement fusion experiments with OMEGA - a 30 kj, 60 beam UV laser. *Fusion Engineering and Design*, 44(1):35, 1999.

[27] E. M. Campbell, J. T. Hunt, E. S. Bliss, D. R. Speck, and R. P. Drake. Nova experimental facility. *Review of Scientific Instruments*, 57(8):2101, 1986.

[28] C. Yamanaka, S. Nakai, T. Yamanaka, Y. Izawa, Y. Kato, K. Mima, K. Nishihara, T. Mochizuki, M. Yamanaka, M. Nakatsuka, et al. High thermonuclear neutron yield by shock multiplexing implosion with GEKKO XII green laser. *Nuclear Fusion*, 27(1):19, 1987.

[29] C. Le Blanc, C. Felix, N. Forget, J. C. Lagron, Ph. Hollander, A. M. Sautivet, C. Sauteret, and A. Migus. *The Petawatt Laser Glass Chain at LULI: Technical Issues and First Results*, page 321. Springer New York, 2004.

[30] C. N. Danson, P. A. Brummitt, R. J. Clarke, J. L. Collier, B. Fell, A. J. Frackiewicz, S. Hancock, S. Hawkes, C. Hernandez-Gomez, P. Holligan, M. H. R. Hutchinson, A. Kidd, W. J. Lester, I. O. Musgrave, D. Neely, D. R. Neville, P. A. Norreys, D. A. Pepler, C. J. Reason, W. Shaikh, T. B. Winstone, R. W. W. Wyatt, and B. E. Wyborn. Vulcan Petawatt - an ultra-high-intensity interaction facility. *Nuclear Fusion*, 44(12):S239, 2004.

[31] G. H. Miller, E. I. Moses, and C. R. Wuest. The National Ignition Facility: enabling fusion ignition for the 21st century. *Nuclear Fusion*, 44(12):S228, 2004.

[32] N. Hopps, C. Danson, S. Duffield, D. Egan, S. Elsmere, M. Girling, E. Harvey, D. Hillier, M. Norman, S. Parker, P. Treadwell, D. Winter, and T. Bett. Overview of laser systems for the orion facility at the AWE. *Applied Optics*, 52(15):3597, 2013.

[33] R. A. Cowley and A. D. B. Woods. Neutron scattering from liquid helium at high energies. *Physical Review Letters*, 21:787, 1968.

[34] W. Montfrooij, P. Westerhuijs, V. O. de Haan, and I. M. de Schepper. Fast sound in a helium-neon mixture determined by neutron scattering. *Physical Review Letters*, 63:544, 1989.

[35] M. Z. Mo, X. Shen, Z. Chen, R. K. Li, M. Dunning, K. Sokolowski-Tinten, Q. Zheng, S. P. Weathersby, A. H. Reid, R. Coffee, et al. Single-shot mega-electronvolt ultrafast electron diffraction for structure dynamic studies of warm dense matter. *Review of Scientific Instruments*, 87(11):11D810, 2016.

[36] L. M. Barker and R. E. Hollenbach. Laser interferometer for measuring high velocities of any reflecting surface. *Journal of Applied Physics*, 43(11):4669, 1972.

[37] M. D. Knudson, D. L. Hanson, J. E. Bailey, C. A. Hall, J. R. Asay, and W. W. Anderson. Equation of state measurements in liquid deuterium to 70 GPa. *Physical Review Letters*, 87:225501, 2001.

[38] A. B. Zylstra, J. A. Frenje, P. E. Grabowski, C. K. Li, G. W. Collins, P. Fitzsimmons, S. Glenzer, F. Graziani, S. B. Hansen, S. X. Hu, M. Gatu Johnson, P. Keiter, H. Reynolds, J. R. Rygg, F. H. Séguin, and R. D. Petrasso. Measurement of charged-particle stopping in warm dense plasma. *Physical Review Letters*, 114:215002, 2015.

[39] Y. Kuramitsu, Y. Sakawa, S. Dono, C. D. Gregory, S. A. Pikuz, B. Loupias, M. Koenig, J. N. Waugh, N. Woolsey, T. Morita, T. Moritaka, T. Sano, Y. Matsumoto, A. Mizuta, N. Ohnishi, and H. Takabe. Kelvin-helmholtz turbulence associated with collisionless shocks in laser produced plasmas. *Physical Review Letters*, 108:195004, 2012.

[40] A. Y. Faenov, I. Y. Skobelev, T. A. Pikuz, S. A. Pikuz, R. Kodama, and V. E. Fortov. Diagnostics of warm dense matter by high-resolution X-ray spectroscopy of hollow ions. *Laser and Particle Beams*, 33:27, 2015.

[41] R. Torchio, F. Occelli, O. Mathon, A. Sollier, E. Lescoute, L. Videau, T. Vinci, A. Benuzzi-Mounaix, J. Headspith, W. Helsby, et al. Probing local and electronic structure in warm dense matter: single pulse synchrotron X-ray absorption spectroscopy on shocked fe. *Scientific Reports*, 6:26402, 2016.

[42] R. Torchio, F. Occelli, O. Mathon, A. Sollier, E. Lescoute, L. Videau, T. Vinci, A. Benuzzi-Mounaix, J. Headspith, W. Helsby, et al. Probing local and electronic structure in warm dense matter: single pulse synchrotron X-ray absorption spectroscopy on shocked Fe. *Scientific Reports*, 6:26402, 2016.

[43] W. L. Bragg. The diffraction of short electromagnetic waves by a crystal. *Scientia*, 23(45):153, 1929.

[44] J. D. Watson, Francis H. C. Crick, et al. Molecular structure of nucleic acids. *Nature*, 171(4356):737, 1953.

[45] A. G. Michette and C. J. Buckley. *X-ray science and technology*. Institute of Physics Publishing, 1993.

[46] Q. Johnson, A. Mitchell, R. N. Keeler, and L. Evans. X-ray diffraction during shock-wave compression. *Physical Review Letters*, 25(16):1099, 1970.

[47] E. Förster, K. Goetz, K. Schäfer, and W. D. Zimmer. Laser generated plasma as a source for real time studies in X-ray crystal research: Part I: Fundamental remarks about source characteristics and requirements. *Laser and Particle beams*, 2(02):167, 1984.

[48] K. Schafer and W. D. Zimmer. Laser generated plasmas as a source for real time studies in X-ray crystal research part II: In search of an optimum choice of laser plasma coupling conditions. *Laser and Particle Beams*, 2:187, 1984.

[49] J. Arthur, G. Materlik, R. Tatchyn, and H. Winick. The LCLS: A fourth generation light source using the SLAC linac. *Review of Scientific Instruments*, 66(2):1987, 1995.

[50] P. Renaudin, C. Blancard, J. Clérouin, G. Faussurier, P. Noiret, and V. Recoules. Aluminum equation-of-state data in the warm dense matter regime. *Physical Review Letters*, 91(7):075002, 2003.

[51] J. Clérouin, P. Renaudin, Y. Laudernet, P. Noiret, and M. P. Desjarlais. Electrical conductivity and equation-of-state study of warm dense copper: Measurements and quantum molecular dynamics calculations. *Physical Review B*, 71:064203, 2005.

[52] L. B. Da Silva, P. Celliers, G. W. Collins, K. S. Budil, N. C. Holmes, T. W. Barbee Jr., B. A. Hammel, J. D. Kilkenny, R. J. Wallace, M. Ross, R. Cauble, A. Ng, and G. Chiu. Absolute equation of state measurements on shocked liquid deuterium up to 200 GPa (2 Mbar). *Physical Review Letters*, 78:483, 1997.

[53] W. B. Hubbard. Interiors of the giant planets. *Science*, 214(4517):145, 1981.

[54] J. Daligault. Crystal nucleation in the one-component plasma. *Physical Review E*, 73:056407, 2006.

[55] J. Vorberger and D. O. Gericke. Coupled mode effects on energy transfer in weakly coupled, two-temperature plasmas. *Physics of Plasmas*, 16(8):082702, 2009.

[56] P. Celliers, A. Ng, G. Xu, and A. Forsman. Thermal equilibration in a shock wave. *Physical Review Letters*, 68(15):2305, 1992.

[57] A. Ng. Outstanding questions in electron-ion energy relaxation, lattice stability, and dielectric function of warm dense matter. *International Journal of Quantum Chemistry*, 112(1):150, 2012.

[58] F. Dorchies, V. Recoules, J. Bouchet, C. Fourment, P. M. Leguay, B. I. Cho, K. Engelhorn, M. Nakatsutsumi, C. Ozkan, T. Tschentscher, M. Harmand, S. Toleikis, M. Störmer, E. Galtier, H. J. Lee, B. Nagler, P. A. Heimann, and J. Gaudin. Time evolution of electron structure in femtosecond heated warm dense molybdenum. *Physical Review B*, 92:144201, 2015.

[59] T. G. White, J. Vorberger, C. R. D. Brown, B. J. B. Crowley, P. Davis, S. H. Glenzer, J. W. O. Harris, D. C. Hochhaus, S. Le Pape, T. Ma, C. D. Murphy, P. Neumayer, L. K. Pattison, S. Richardson, D. O. Gericke, and G. Gregori. Observation of inhibited electron-ion coupling in strongly heated graphite. *Scientific Reports*, 2:889, 2012.

[60] J. Clérouin, G. Robert, P. Arnault, C. Ticknor, J. D. Kress, and L. A. Collins. Evidence for out-of-equilibrium states in warm dense matter probed by X-ray Thomson scattering. *Physical Review E*, 91:011101, 2015.

[61] W. R. Johnson and J. Nilsen. Average-atom treatment of relaxation time in X-ray Thomson scattering from warm dense matter. *Physical Review E*, 93:033205, 2016.

[62] M. Roth, I. Alber, V. Bagnoud, C. R. D. Brown, R. Clarke, H. Daido, J. Fernandez, K. Flippo, S. Gaillard, C. Gauthier, et al. Proton acceleration experiments and warm dense matter research using high power lasers. *Plasma Physics and Controlled Fusion*, 51(12):124039, 2009.

[63] A. B. Zylstra, J. A. Frenje, P. E. Grabowski, C. K. Li, G. W. Collins, P. Fitzsimmons, S. Glenzer, F. Graziani, S. B. Hansen, S. X. Hu, M. Gatu Johnson, P. Keiter, H. Reynolds, J. R. Rygg, F. H. Séguin, and R. D. Petrasso. Measurement of charged-particle stopping in warm dense plasma. *Physical Review Letters*, 114:215002, 2015.

[64] Z. Donkó and P. Hartmann. Shear viscosity of strongly coupled Yukawa liquids. *Physical Review E*, 78(2):026408, 2008.

[65] I. Morozov, H. Reinholz, G. Röpke, A. Wierling, and G. Zwicknagel. Molecular dynamics simulations of optical conductivity of dense plasmas. *Physical Review E*, 71(6):066408, 2005.

[66] S. Mazevet, J. Clérouin, V. Recoules, P. M. Anglade, and G. Zerah. Ab-initio simulations of the optical properties of warm dense gold. *Physical Review Letters*, 95:085002, 2005.

[67] H. Reinholz, G. Röpke, S. Rosmej, and R. Redmer. Conductivity of warm dense matter including electron-electron collisions. *Physical Review E*, 91(4):043105, 2015.

[68] B. Meerson. Nonlinear dynamics of radiative condensations in optically thin plasmas. *Reviews of Modern Physics*, 68:215, 1996.

[69] J. D. Lindl, P. Amendt, R. L. Berger, S. G. Glendinning, S. H. Glenzer, S. W. Haan, R. L. Kauffman, O. L. Landen, and L. J. Suter. The physics basis for ignition using indirect-drive targets on the National Ignition Facility. *Physics of Plasmas*, 11(2):339, 2004.

[70] S. H. Glenzer et al. Demonstration of ignition radiation temperatures in indirect-drive inertial confinement fusion hohlraums. *Physical Review Letters*, 106:085004, 2011.

[71] D. O. Gericke, J. Vorberger, K. Wünsch, and G. Gregori. Screening of ionic cores in partially ionized plasmas within linear response. *Physical Review E*, 81(6):065401, 2010.

[72] J. P. Mithen. *Molecular dynamics simulations of the equilibrium dynamics of nonideal plasmas*. PhD thesis, Trinity College, University of Oxford, 2012.

[73] D. A. Baiko, A. D. Kaminker, A. Y. Potekhin, and D. G. Yakovlev. Ion structure factors and electron transport in dense coulomb plasmas. *Physical Review Letters*, 81(25):5556, 1998.

[74] T. W. Johnston and J. M. Dawson. Correct values for high-frequency power absorption by inverse bremsstrahlung in plasmas. *Physics of Fluids*, 16(5):722, 1973.

[75] J. F. Seely and E. G. Harris. Heating of a plasma by multiphoton inverse bremsstrahlung. *Physical Review A*, 7(3):1064, 1973.

[76] L. Schlessinger and J. Wright. Inverse-bremsstrahlung absorption rate in an intense laser field. *Physical Review A*, 20(5):1934, 1979.

[77] R. O. Dendy. *Plasma physics: an introductory course*. Cambridge University Press, 1995.

[78] J. P. Freidberg, R. W. Mitchell, R. L. Morse, and L. I. Rudsinski. Resonant absorption of laser light by plasma targets. *Physical Review Letters*, 28(13):795, 1972.

[79] J. D. Colvin and D. H. Kalantar. Scaling of pressure with intensity in laser-driven shocks and effects of hot X-ray preheat. In *AIP Conference Proceedings*, volume 845, page 1413, 2006.

[80] S. A. Bonev, B. Militzer, and G. Galli. Ab initio simulations of dense liquid deuterium: Comparison with gas-gun shock-wave experiments. *Physical Review B*, 69(1):014101, 2004.

[81] S. N. Luo, B. J. Jensen, D. E. Hooks, K. Fezzaa, K. J. Ramos, J. D. Yeager, K. Kwiatkowski, and T. Shimada. Gas gun shock experiments with single-pulse X-ray phase contrast imaging and diffraction at the advanced photon source. *Review of Scientific Instruments*, 83(7):073903, 2012.

[82] J. C. Valenzuela, C. Krauland, D. Mariscal, I. Krasheninnikov, F. N. Beg, P. Wiewior, A. Covington, R. Presura, T. Ma, C. Niemann, et al. Diagnosing pulsed power produced plasmas with X-ray Thomson scattering at the Nevada Terawatt Facility. In *APS Meeting Abstracts*, 2015.

[83] P. Vinet, J. R. Smith, J. Ferrante, and J. H. Rose. Temperature effects on the universal equation of state of solids. *Physical Review B*, 35:1945, 1987.

[84] D. Beule, W. Ebeling, A. Förster, H. Juranek, S. Nagel, R. Redmer, and G. Röpke. Equation of state for hydrogen below 10000 K: From the fluid to the plasma. *Physical Review B*, 59:14177, 1999.

[85] Blinnikov, S. I., Panov, I. V., Rudzsky, M. A., and Sumiyoshi, K. The equation of state and composition of hot, dense matter in core-collapse supernovae. *Astronomy and Astrophysics*, 535:A37, 2011.

[86] K. P. Driver and B. Militzer. First-principles equation of state calculations of warm dense nitrogen. *Physical Review B*, 93:064101, 2016.

[87] D. C. Swift and R. G. Kraus. Properties of plastic ablators in laser-driven material dynamics experiments. *Physical Review E*, 77(6):066402, 2008.

[88] A. L. Kritcher, P. Neumayer, J. Castor, T. Döppner, R. W. Falcone, O. L. Landen, H. J. Lee, R. W. Lee, E. C. Morse, A. Ng, et al. Ultrafast X-ray Thomson scattering of shock-compressed matter. *Science*, 322(5898):691, 2008.

[89] H. J. Lee, P. Neumayer, J. Castor, T. Döppner, R. W. Falcone, C. Fortmann, B. A. Hammel, A. L. Kritcher, O. L. Landen, R. W. Lee, et al. X-ray Thomson scattering measurements of density and temperature in shock-compressed beryllium. *Physical Review Letters*, 102(11):115001, 2009.

[90] N. J. Hartley, P. Belancourt, D. A. Chapman, T. Dppner, R. P. Drake, D. O. Gericke, S. H. Glenzer, D. Khaghani, S. LePape, T. Ma, P. Neumayer, A. Pak, L. Peters, S. Richardson, J. Vorberger, T. G. White, and G. Gregori. Electron-ion temperature equilibration in warm dense tantalum. *High Energy Density Physics*, 14:1, 2015.

[91] S. H. Glenzer, O. L. Landen, P. Neumayer, R. W. Lee, K. Widmann, S. W. Pollaine, R. J. Wallace, G. Gregori, A. Höll, et al. Observations of plasmons in warm dense matter. *Physical Review Letters*, 98(6):065002, 2007.

[92] E. L. Saldin, E. A. Schneidmiller, and M. V. Yurkov. Coherence properties of the radiation from X-ray free electron laser. *Optics Communications*, 281(5):1179, 2008.

[93] R. Abela et al. The European X-ray free-electron laser. Technical report, DESY XFEL Project Group European, XFEL Project Team, Deutsches Elektronen-Synchrotron, Member of the Helmholtz Association, 2010.

[94] E. Burkel. Introduction to X-ray scattering. *Journal of Physics: Condensed Matter*, 13(34):7477, 2001.

[95] M. von Laue. Concerning the detection of X-ray interferences. *Nobel lecture*, 1915.

[96] B. E. Warren. *X-ray Diffraction*. Courier Corporation, 1969.

[97] A. Higginbotham and D. McGonegle. Prediction of Debye-Scherrer diffraction patterns in arbitrarily strained samples. *Journal of Applied Physics*, 115(17):174906, 2014.

[98] D. McGonegle, D. Milathianaki, B. A. Remington, J. S. Wark, and A. Higginbotham. Simulations of in situ X-ray diffraction from uniaxially compressed highly textured polycrystalline targets. *Journal of Applied Physics*, 118(6):065902, 2015.

[99] L. B. Fletcher, H. J. Lee, T. Döppner, E. Galtier, B. Nagler, P. Heimann, C. Fortmann, S. LePape, T. Ma, M. Millot, et al. Ultrabright X-ray laser scattering for dynamic warm dense matter physics. *Nature Photonics*, 9(4):274, 2015.

[100] B. Barbrel, M. Koenig, A. Benuzzi-Mounaix, E. Brambrink, C. R. D. Brown, D. O. Gericke, B. Nagler, M. Rabec le Gloahec, D. Riley, C. Spindloe, S. M. Vinko, J. Vorberger, J. Wark, K. Wünsch, and G. Gregori. Measurement of short-range correlations in shock-compressed plastic by short-pulse X-ray scattering. *Physical Review Letters*, 102:165004, 2009.

[101] J. Chihara. Difference in X-ray scattering between metallic and non-metallic liquids due to conduction electrons. *Journal of Physics F: Metal Physics*, 17(2):295, 1987.

[102] J. Chihara. Interaction of photons with plasmas and liquid metals-photoabsorption and scattering. *Journal of Physics: Condensed Matter*, 12(3):231, 2000.

[103] S. Galambosi. *Electronic excitations in solids studied using inelastic X-ray scattering*. PhD thesis, University of Helsinki, 2007.

[104] S. H. Glenzer and R. Redmer. X-ray Thomson scattering in high energy density plasmas. *Reviews of Modern Physics*, 81(4):1625, 2009.

[105] O. Ciricosta, S. M. Vinko, H.-K. Chung, B.-I. Cho, C. R. D. Brown, T. Burian, J. Chalupskỳ, K. Engelhorn, R. W. Falcone, C. Graves, et al. Direct measurements of the ionization potential depression in a dense plasma. *Physical Review Letters*, 109(6):065002, 2012.

[106] L. B. Fletcher, A. L. Kritcher, A. Pak, T. Ma, T. Döppner, C. Fortmann, L. Divol, O. S. Jones, O. L. Landen, H. A. Scott, et al. Observations of continuum depression in warm dense matter with X-ray Thomson scattering. *Physical Review Letters*, 112(14):145004, 2014.

[107] P. Neumayer, G. Gregori, A. Ravasio, M. Koenig, D. Price, K. Widmann, M. Bastea, O. L. Landen, and S. H. Glenzer. Solid-density plasma characterization with X-ray scattering on the 200 J Janus laser. *Review of Scientific Instruments*, 77(10):10F317, 2006.

[108] T. Döppner, A. L. Kritcher, D. Kraus, S. H. Glenzer, B. L. Bachmann, D. Chapman, G. W. Collins, R. W. Falcone, J. Hawreliak, O. L. Landen, et al. X-ray Thomson scattering as a temperature probe for gbar shock experiments. In *Journal of Physics: Conference Series*, volume 500, page 192019. IOP Publishing, 2014.

[109] J. Vorberger and D. O. Gericke. *Ab initio* approach to model X-ray diffraction in warm dense matter. *Physical Review E*, 91:033112, 2015.

[110] A. D. Baczewski, L. Shulenburger, M. P. Desjarlais, S. B. Hansen, and R. J. Magyar. X-ray Thomson scattering in warm dense matter without the Chihara decomposition. *Physical Review Letters*, 116(11):115004, 2016.

[111] G. Gregori and D. O. Gericke. Low frequency structural dynamics of warm dense matter. *Physics of Plasmas*, 16(5):056306, 2009.

[112] S. Plimpton. Fast parallel algorithms for short-range molecular dynamics. *Journal of computational physics*, 117(1):1, 1995.

[113] B.-Y. Cao, M. Chen, and Z.-Y. Guo. Effect of surface roughness on gas flow in microchannels by molecular dynamics simulation. *International Journal of Engineering Science*, 44(13):927, 2006.

[114] G. C. Lie and E. Clementi. Molecular-dynamics simulation of liquid water with an ab initio flexible water-water interaction potential. *Physical Review A*, 33(4):2679, 1986.

[115] G. Mogni, A. Higginbotham, K. Gaál-Nagy, N. Park, and J. S. Wark. Molecular dynamics simulations of shock-compressed single-crystal silicon. *Physical Review B*, 89(6):064104, 2014.

[116] K. F. Mansfield and D. N. Theodorou. Molecular dynamics simulation of a glassy polymer surface. *Macromolecules*, 24(23):6283, 1991.

[117] M. H. Shapiro and T. A. Tombrello. Simulation of cluster impacts on metallic surfaces. *Physical Review Letters*, 65(1):92, 1990.

[118] J. Vorberger, Z. Donko, I. M. Tkachenko, and D. O. Gericke. Dynamic ion structure factor of warm dense matter. *Physical Review Letters*, 109:225001, 2012.

[119] L. Verlet. Computer 'experiments' on classical fluids. I. thermodynamical properties of Lennard-Jones molecules. *Physical Review*, 159(1):98, 1967.

[120] S. Nosé. A unified formulation of the constant temperature molecular dynamics methods. *The Journal of chemical physics*, 81(1):511, 1984.

[121] W. G. Hoover. Canonical dynamics: equilibrium phase-space distributions. *Physical Review A*, 31(3):1695, 1985.

[122] D. J. Evans and G. P. Morriss. The isothermal/isobaric molecular dynamics ensemble. *Physics Letters A*, 98(8):433, 1983.

[123] N. Binggeli and J. R. Chelikowsky. Langevin molecular dynamics with quantum forces: application to silicon clusters. *Physical Review B*, 50(16):11764, 1994.

[124] J. von Plato. Boltzmann's ergodic hypothesis. *Archive for History of Exact Sciences*, 42(1):71, 1991.

[125] T. G. White, S. Richardson, B. J. B. Crowley, L. K. Pattison, J. W. O. Harris, and G. Gregori. Orbital-free density-functional theory simulations of the dynamic structure factor of warm dense aluminum. *Physical Review Letters*, 111(17):175002, 2013.

[126] H. R. Rüter and R. Redmer. Ab initio simulations for the ion-ion structure factor of warm dense aluminum. *Physical Review Letters*, 112(14):145007, 2014.

[127] J. Vorberger and D. O. Gericke. Effective ion-ion potentials in warm dense matter. *High Energy Density Physics*, 9(1):178, 2013.

[128] M. S. Daw and M. I. Baskes. Semiempirical, quantum mechanical calculation of hydrogen embrittlement in metals. *Physical Review Letters*, 50(17):1285, 1983.

[129] E. W. Brown, B. K. Clark, J. L. DuBois, and D. M. Ceperley. Path-integral Monte Carlo simulation of the warm dense homogeneous electron gas. *Physical Review Letters*, 110(14):146405, 2013.

[130] K. P. Driver and B. Militzer. All-electron path integral monte carlo simulations of warm dense matter: application to water and carbon plasmas. *Physical Review Letters*, 108(11):115502, 2012.

[131] R. E. Wyatt. *Quantum dynamics with trajectories: introduction to quantum hydrodynamics*, volume 28. Springer Science and Business Media, 2006.

[132] B. Militzer, W. B. Hubbard, J. Vorberger, I. Tamblyn, and S. A. Bonev. A massive core in Jupiter predicted from first-principles simulations. *The Astrophysical Journal Letters*, 688(1):L45, 2008.

[133] N. Goldman, E. J. Reed, I. F. W. Kuo, L. E. Fried, C. J. Mundy, and A. Curioni. Ab initio simulation of the equation of state and kinetics of shocked water. *The Journal of Chemical Physics*, 130(12):124517, 2009.

[134] W. Lorenzen, B. Holst, and R. Redmer. First-order liquid-liquid phase transition in dense hydrogen. *Physical Review B*, 82(19):195107, 2010.

[135] K. Wünsch, J. Vorberger, and D. O. Gericke. Ion structure in warm dense matter: Benchmarking solutions of hypernetted-chain equations by first-principle simulations. *Physical Review E*, 79(1):010201, 2009.

[136] D. Swift, J. Hawreliak, D. Braun, A. Kritcher, S. H. Glenzer, G. W. Collins, S. Rothman, D. Chapman, and S. Rose. Gigabar material properties experiments on NIF and OMEGA. *AIP Conference Proceedings*, 1426(1):477, 2012.

[137] N. Amadou, E. Brambrink, A. Benuzzi-Mounaix, G. Huser, F. Guyot, S. Mazevet, G. Morard, T. De Resseguier, T. Vinci, K. Myanishi, et al. Direct laser-driven ramp compression studies of iron: A first step toward the reproduction of planetary core conditions. *High Energy Density Physics*, 9(2):243, 2013.

[138] T. G. White, N. J. Hartley, B. Borm, B. J. B. Crowley, J. W. O. Harris, D. C. Hochhaus, T. Kaempfer, K. Li, P. Neumayer, L. K. Pattison, et al. Electron-ion equilibration in ultrafast heated graphite. *Physical Review Letters*, 112(14):145005, 2014.

[139] U. Zastrau, P. Sperling, M. Harmand, A. Becker, T. Bornath, R. Bredow, S. Dziarzhytski, T. Fennel, L. B. Fletcher, E. Förster, et al. Resolving ultrafast heating of dense cryogenic hydrogen. *Physical Review Letters*, 112(10):105002, 2014.

[140] Z. Chen, B. Holst, S. E. Kirkwood, V. Sametoglu, M. Reid, Y. Y. Tsui, V. Recoules, and A. Ng. Evolution of ac conductivity in nonequilibrium warm dense gold. *Physical Review Letters*, 110:135001, 2013.

[141] G. Bannasch, J. Castro, P. McQuillen, T. Pohl, and T. C. Killian. Velocity relaxation in a strongly coupled plasma. *Physical Review Letters*, 109:185008, 2012.

[142] S. P. Hau-Riege, A. Graf, T. Döppner, R. A. London, J. Krzywinski, C. Fortmann, S. H. Glenzer, M. Frank, K. Sokolowski-Tinten, M. Messerschmidt, C. Bostedt, S. Schorb, J. A. Bradley, A. Lutman, D. Rolles, A. Rudenko, and B. Rudek. Ultrafast transitions from solid to liquid and plasma states of graphite induced by X-ray free-electron laser pulses. *Physical Review Letters*, 108:217402, 2012.

[143] M. Nicoul, U. Shymanovich, A. Tarasevitch, D. von der Linde, and K. Sokolowski-Tinten. Picosecond acoustic response of a laser-heated gold film studied with time-resolved X-ray diffraction. *Applied Physics Letters*, 98(19), 2011.

[144] Z. Lin, L. V. Zhigilei, and V. Celli. Electron-phonon coupling and electron heat capacity of metals under conditions of strong electron-phonon nonequilibrium. *Physical Review B*, 77:075133, 2008.

[145] P. M. Leguay, A. Lévy, B. Chimier, F. Deneuville, D. Descamps, C. Fourment, C. Goyon, S. Hulin, S. Petit, O. Peyrusse, J. J. Santos, P. Combis, B. Holst, V. Recoules, P. Renaudin, L. Videau, and F. Dorchies. Ultrafast short-range

disordering of femtosecond-laser-heated warm dense aluminum. *Physical Review Letters*, 111:245004, 2013.

[146] P. Celliers, A. Ng, G. Xu, and A. Forsman. Thermal equilibration in a shock wave. *Physical Review Letters*, 68:2305, 1992.

[147] A. Ng, P. Celliers, G. Xu, and A. Forsman. Electron-ion equilibration in a strongly coupled plasma. *Physical Review E*, 52:4299, 1995.

[148] D. Riley, N. C. Woolsey, D. McSherry, I. Weaver, A. Djaoui, and E. Nardi. X-ray diffraction from a dense plasma. *Physical Review Letters*, 84:1704, 2000.

[149] M. W. C. Dharma-Wardana and F. Perrot. Energy relaxation and the quasiequation of state of a dense two-temperature nonequilibrium plasma. *Physical Review E*, 58:3705, 1998.

[150] J. Vorberger, D. O. Gericke, Th. Bornath, and M. Schlanges. Energy relaxation in dense, strongly coupled two-temperature plasmas. *Physical Review E*, 81:046404, 2010.

[151] G. Gregori and D. O. Gericke. A reduced coupled-mode description for the electron-ion energy relaxation in dense matter. *EPL (Europhysics Letters)*, 83(1):15002, 2008.

[152] J. Daligault and G. Dimonte. Correlation effects on the temperature-relaxation rates in dense plasmas. *Physical Review E*, 79(5):056403, 2009.

[153] M. W. C. Dharma-Wardana. Electron-ion and ion-ion potentials for modeling warm dense matter: Applications to laser-heated or shock-compressed Al and Si. *Physical Review E*, 86(3):036407, 2012.

[154] B. Holst, V. Recoules, S. Mazevet, M. Torrent, A. Ng, Z. Chen, S. E. Kirkwood, V. Sametoglu, M. Reid, and Y. Y. Tsui. Ab initio model of optical properties of two-temperature warm dense matter. *Physical Review B*, 90(3):035121, 2014.

[155] T. Ao, Y. Ping, K. Widmann, D. F. Price, E. Lee, H. Tam, P. T. Springer, and A. Ng. Optical properties in nonequilibrium phase transitions. *Physical Review Letters*, 96(5):055001, 2006.

[156] E. Bévillon, J.-P. Colombier, V. Recoules, and R. Stoian. Free-electron properties of metals under ultrafast laser-induced electron-phonon nonequilibrium: A first-principles study. *Physical Review B*, 89(11):115117, 2014.

[157] J. Bardeen, L. N. Cooper, and J. R. Schrieffer. Theory of superconductivity. *Physical Review*, 108:1175, 1957.

[158] N. W. Ashcroft and N. D. Mermin. *Solid state physics*. Saunders, 1976.

[159] S.-S. Wellershoff, J. Hohlfeld, J. Güdde, and E. Matthias. The role of electron–phonon coupling in femtosecond laser damage of metals. *Applied Physics A*, 69(1):S99, 1999.

[160] M. C. Klein, F. Hache, D. Ricard, and C. Flytzanis. Size dependence of electron-phonon coupling in semiconductor nanospheres: The case of CdSe. *Physical Review B*, 42:11123, 1990.

[161] D. Bäuerle. *Laser processing and chemistry*. Springer, 2011.

[162] S. Atzeni and J. Meyer-ter Vehn. *The physics of inertial fusion*. Oxford University Press, 2009.

[163] S. I. Anisimov, B. L. Kapeliovich, and T. L Perel'man. Electron emission from metal surfaces exposed to ultrashort laser pulses. *Journal of Experimental and Theoretical Physics*, 66:776, 1974.

[164] B. L. Altshuler, A. G. Aronov, and P. A. Lee. Interaction effects in disordered Fermi systems in two dimensions. *Physical Review Lett.*, 44:1288, 1980.

[165] M. B. Agranat, S. I. Anisimov, and B. I. Makshantsev. The anomalous thermal radiation from metals produced by ultrashort laser pulses. I. *Applied Physics B*, 47(3):209, 1988.

[166] H. E. Elsayed-Ali and T. Juhasz. Femtosecond time-resolved thermomodulation of thin gold films with different crystal structures. *Physical Review B*, 47:13599, 1993.

[167] Z. G. Wang, C. Dufour, E. Paumier, and M. Toulemonde. The Se sensitivity of metals under swift-heavy-ion irradiation: a transient thermal process. *Journal of Physics: Condensed Matter*, 6(34):6733, 1994.

[168] M. Toulemonde, W. Assmann, C. Trautmann, F. Grüner, H. D. Mieskes, H. Kucal, and Z. G. Wang. Electronic sputtering of metals and insulators by swift heavy ions. *Nuclear Instruments and Methods in Physics Research Section B: Beam Interactions with Materials and Atoms*, 212:346, 2003.

[169] T. Q. Qiu and C. L. Tien. Size effects on nonequilibrium laser heating of metal films. *Journal of Heat Transfer*, 115(4):842, 1993.

[170] P. E. Hopkins and P. M. Norris. Substrate influence in electron–phonon coupling measurements in thin Au films. *Applied Surface Science*, 253(15):6289, 2007.

[171] J. K. Chen and J. E. Beraun. Numerical study of ultrashort laser pulse interactions with metal films. *Numerical Heat Transfer: Part A: Applications*, 40(1):1, 2001.

[172] E. Carpene. Ultrafast laser irradiation of metals: Beyond the two-temperature model. *Physical Review B*, 74(2):024301, 2006.

[173] H. Hakkinen and U. Landman. Superheating, melting, and annealing of copper surfaces. *Physical Review Letters*, 71(7):1023, 1993.

[174] C. Schäfer, H. M. Urbassek, and L. V. Zhigilei. Metal ablation by picosecond laser pulses: A hybrid simulation. *Physical Review B*, 66(11):115404, 2002.

[175] D. S. Ivanov and L. V. Zhigilei. Combined atomistic-continuum modeling of short-pulse laser melting and disintegration of metal films. *Physical Review B*, 68(6):064114, 2003.

[176] Z. Lin and L. V. Zhigilei. Time-resolved diffraction profiles and atomic dynamics in short-pulse laser-induced structural transformations: Molecular dynamics study. *Physical Review B*, 73(18):184113, 2006.

[177] C. Rose-Petruck, R. Jimenez, T. Guo, A. Cavalleri, C. W. Siders, F. Rksi, J. A. Squier, B. C. Walker, K. R. Wilson, and C. P. J. Barty. Picosecond-milliangstrom lattice dynamics measured by ultrafast X-ray diffraction. *Nature*, 398(6725):310, 1999.

[178] B. Y. Mueller and B. Rethfeld. Relaxation dynamics in laser-excited metals under nonequilibrium conditions. *Physical Review B*, 87:035139, 2013.

[179] K. Kadau, T. C. Germann, P. S. Lomdahl, and B. L. Holian. Microscopic view of structural phase transitions induced by shock waves. *Science*, 296(5573):1681, 2002.

[180] M. Suggit, A. Higginbotham, G. Mogni, J. Wark, E. Bringa, P. Erhart, J. Hawreliak, B. Remington, and N. Park. Shock induced deformation twinning in tantalum md simulations. In *APS Shock Compression of Condensed Matter Meeting Abstracts*, volume 1, page 6004, 2013.

[181] G Mogni, A Higginbotham, K. Gaál-Nagy, N. Park, and J. S. Wark. Molecular dynamics simulations of shock-compressed single-crystal silicon. *Physical Review B*, 89(6):064104, 2014.

[182] W. S. Fann, R. Storz, H. W. K. Tom, and J. Bokor. Direct measurement of nonequilibrium electron-energy distributions in subpicosecond laser-heated gold films. *Physical Review Letters*, 68(18):2834, 1992.

[183] S. D. Brorson, J. G. Fujimoto, and E. P. Ippen. Femtosecond electronic heat-transport dynamics in thin gold films. *Physical Review Letters*, 59:1962, 1987.

[184] T. Juhasz, H. E. Elsayed-Ali, G. O. Smith, C. Suárez, and W. E. Bron. Direct measurements of the transport of nonequilibrium electrons in gold films with different crystal structures. *Physical Review B*, 48:15488, 1993.

[185] T. G. White. *Study of high energy density matter through quantum molecular dynamics and time resolved X-ray scattering*. PhD thesis, Trinity College, University of Oxford, 2014.

[186] H. W. Sheng, M. J. Kramer, A. Cadien, T. Fujita, and M. W. Chen. Highly optimized embedded-atom-method potentials for fourteen fcc metals. *Physical Review B*, 83:134118, 2011.

[187] J. Hohlfeld, S.-S. Wellershoff, J. Güdde, U. Conrad, V. Jähnke, and E. Matthias. Electron and lattice dynamics following optical excitation of metals. *Chemical Physics*, 251(1):237, 2000.

[188] M. Ligges, I. Rajkovic, P. Zhou, O. Posth, C. Hassel, G. Dumpich, and D. von der Linde. Observation of ultrafast lattice heating using time resolved electron diffraction. *Applied Physics Letters*, 94(10), 2009.

[189] O. B. Wright. Ultrafast nonequilibrium stress generation in gold and silver. *Physical Review B*, 49:9985, 1994.

[190] T. Ma, T. Döppner, R. W. Falcone, L. Fletcher, C. Fortmann, D. O. Gericke, O. L. Landen, H. J. Lee, A. Pak, J. Vorberger, K. Wünsch, and S. H. Glenzer. X-ray scattering measurements of strong ion-ion correlations in shock-compressed aluminum. *Physical Review Letters*, 110:065001, 2013.

[191] D. Kraus, J. Vorberger, D. O. Gericke, V. Bagnoud, A. Blažević, W. Cayzac, A. Frank, G. Gregori, A. Ortner, A. Otten, F. Roth, G. Schaumann, D. Schumacher, K. Siegenthaler, F. Wagner, K. Wünsch, and M. Roth. Probing the complex ion structure in liquid carbon at 100 GPa. *Physical Review Letters*, 111:255501, 2013.

[192] R. Tommasini, R. Bruch, E. Fill, and A. Bjeoumikhov. Convergent-beam diffraction of ultra-short hard X-ray pulses focused by a capillary lens. *Applied Physics B*, 82(4):519, 2006.

[193] G. Chabrier, F. Douchin, and A. Y. Potekhin. Dense astrophysical plasmas. *Journal of Physics: Condensed Matter*, 14(40):9133, 2002.

[194] B. A. Remington, R. P. Drake, and D. D. Ryutov. Experimental astrophysics with high power lasers and Z pinches. *Reviews of Modern Physics*, 78:755, 2006.

[195] R. Kodama, P. A. Norreys, K. Mima, A. E. Dangor, R. G. Evans, H. Fujita, Y. Kitagawa, K. Krushelnick, T. Miyakoshi, N. Miyanaga, T. Norimatsu, S. J. Rose, T. Shozaki, K. Shigemori, A. Sunahara, M. Tampo, K. A. Tanaka, Y. Toyama, T. Yamanaka, and M. Zepf. Fast heating of ultra-high-density plasma as a step towards laser fusion ignition. *Nature*, 412(6849):798, 2001.

[196] H. J. Kunze, E. Fünfer, B. Kronast, and W. H. Kegel. Measurement of the spectral distribution of light scattered by a θ-pinch plasma. *Physics Letters*, 11(1):42, 1964.

[197] S. H. Glenzer, W. Rozmus, B. J. MacGowan, K. G. Estabrook, J. D. De Groot, G. B. Zimmerman, H. A. Baldis, J. A. Harte, R. W. Lee, E. A. Williams, and B. G. Wilson. Thomson scattering from high-Z laser-produced plasmas. *Physical Review Letters*, 82:97, 1999.

[198] A. Delserieys, F. Y. Khattak, C. L. S. Lewis, and D. Riley. Optical Thomson scatter from a laser-ablated magnesium plume. *Journal of Applied Physics*, 106(8), 2009.

[199] G. Gregori, S. H. Glenzer, W. Rozmus, R. W. Lee, and O. L. Landen. Theoretical model of X-ray scattering as a dense matter probe. *Physical Review E*, 67:026412, 2003.

[200] S. H. Glenzer, G. Gregori, R. W. Lee, F. J. Rogers, S. W. Pollaine, and O. L. Landen. Demonstration of spectrally resolved X-ray scattering in dense plasmas. *Physical Review Letters*, 90:175002, 2003.

[201] D. Riley, J. J. Angulo-Gareta, F. Y. Khattak, M. J. Lamb, P. S. Foster, E. J. Divall, C. J. Hooker, A. J. Langley, R. J. Clarke, and D. Neely. K-α yields from Ti foils irradiated with ultrashort laser pulses. *Physical Review E*, 71(1):016406, 2005.

[202] D. Riley, F. Y. Khattak, O. A. M. B. Percie du Sert, R. J. Clarke, E. J. Divall, M. Edwards, P. S. Foster, C. J. Hooker, A. J. Langley, P. Mistry, et al. Efficient K-α and He-α emission from Ti foils irradiated with 400 nm, 45 fs laser pulses. *Journal of Quantitative Spectroscopy and Radiative Transfer*, 99(1):537, 2006.

[203] G. Nersisyan, M. Makita, K. McKeever, T. Dzelzainis, S. White, E. Nedanovska, B. Kettle, R. Nicholl, G. Williams, D. Riley, and C. L. S. Lewis. Electron refluxing and K-shell line emission from Ti foils irradiated with sub-picosecond laser pulses at 527 nm. *Physical Review E*, 85:056415, 2012.

[204] N. L. Kugland, G. Gregori, S. Bandyopadhyay, C. M. Brenner, C. R. D. Brown, C. Constantin, S. H. Glenzer, F. Y. Khattak, A. L. Kritcher, C. Niemann, A. Otten, J. Pasley, A. Pelka, M. Roth, C. Spindloe, and D. Riley. Evolution of elastic X-ray scattering in laser-shocked warm dense lithium. *Physical Review E*, 80:066406, 2009.

[205] S. P. Regan, K. Falk, G. Gregori, P. B. Radha, S. X. Hu, T. R. Boehly, B. J. B. Crowley, S. H. Glenzer, O. L. Landen, D. O. Gericke, T. Döppner, D. D. Meyerhofer, C. D. Murphy, T. C. Sangster, and J. Vorberger. Inelastic X-ray scattering from shocked liquid deuterium. *Physical Review Letters*, 109:265003, 2012.

[206] C. R. D. Brown, D. O. Gericke, M. Cammarata, B. I. Cho, T. Döppner, K. Engelhorn, E. Förster, C. Fortmann, D. Fritz, E. Galtier, S. H. Glenzer, M. Harmand, P. Heimann, N. L. Kugland, D. Q. Lamb, H. J. Lee, R. W. Lee, H. Lemke, M. Makita, A. Moinard, C. D. Murphy, B. Nagler, P. Neumayer, K.-U. Plagemann, R. Redmer, D. Riley, F. B. Rosmej, P. Sperling, S. Toleikis, S. M. Vinko, J. Vorberger, S. White, T. G. White, K. Wünsch, U. Zastrau, D. Zhu, T. Tschentscher, and G. Gregori. Evidence for a glassy state in strongly driven carbon. *Scientific Reports*, 4:5214, 2014.

[207] M. K. Urry, G. Gregori, O. L. Landen, A. Pak, and S. H. Glenzer. X-ray probe development for collective scattering measurements in dense plasmas. *Journal of Quantitative Spectroscopy and Radiative Transfer*, 99(1):636, 2006.

[208] F. Coppari, R. F. Smith, J. H. Eggert, J. Wang, J. R. Rygg, A. Lazicki, J. A. Hawreliak, G. W. Collins, and T. S. Duffy. Experimental evidence for a phase transition in magnesium oxide at exoplanet pressures. *Nature Geoscience*, 6(11):926, 2013.

[209] A. Higginbotham, S. Patel, J. A. Hawreliak, O. Ciricosta, G. W. Collins, F. Coppari, J. H. Eggert, M. J. Suggit, H. Tang, and J. S. Wark. Single photon energy dispersive X-ray diffraction. *Review of Scientific Instruments*, 85(3), 2014.

[210] D.C. Eder, G. Pretzler, E. Fill, K. Eidmann, and A. Saemann. Spatial characteristics of K-α radiation from weakly relativistic laser plasmas. *Applied Physics B*, 70(2):211, 2000.

[211] A. Ravasio, G. Gregori, A. Benuzzi-Mounaix, J. Daligault, A. Delserieys, A. Ya. Faenov, B. Loupias, N. Ozaki, M. Rabec le Gloahec, T. A. Pikuz, D. Riley, and M. Koenig. Direct observation of strong ion coupling in laser-driven shock-compressed targets. *Physical Review Letters*, 99:135006, 2007.

[212] S. N. Chen, G. Gregori, P. K. Patel, H.-K. Chung, R. G. Evans, R. R. Freeman, E. Garcia Saiz, S. H. Glenzer, S. B. Hansen, F. Y. Khattak, J. A. King, A. J. Mackinnon, M. M. Notley, J. R. Pasley, D. Riley, R. B. Stephens, R. L. Weber, S. C. Wilks, and F. N. Beg. Creation of hot dense matter in short-pulse laser-plasma interaction with tamped titanium foils. *Physics of Plasmas*, 14(10):102701, 2007.

[213] I. J. Paterson, R. J. Clarke, N. C. Woolsey, and G. Gregori. Image plate response for conditions relevant to laser-plasma interaction experiments. *Measurement Science and Technology*, 19(9):095301, 2008.

[214] A. Rousse, P. Audebert, J.-P. Geindre, F. Fallies, J.-C. Gauthier, A. Mysyrowicz, G. Grillon, and A. Antonetti. Efficient K-α X-ray source from femtosecond laser-produced plasmas. *Physical Review E*, 50(3):2200, 1994.

[215] G. I. Kerley. Equation of state and phase diagram of dense hydrogen. *Physics of the Earth and Planetary Interiors*, 6(1):78, 1972.

[216] D. A. Chapman, J. Vorberger, L. B. Fletcher, R. A. Baggott, L. Divol, T. Döppner, R. W. Falcone, S. H. Glenzer, G. Gregori, T. M. Guymer, et al. Observation of finite-wavelength screening in high-energy-density matter. *Nature Communications*, 6:6839, 2015.

[217] J. Sheffield, D. Froula, S. H. Glenzer, and N. C. Luhmann Jr. *Plasma scattering of electromagnetic radiation: theory and measurement techniques*. Academic Press, 2010.

[218] P. Neumayer, C. Fortmann, T. Döppner, P. Davis, R. W. Falcone, A. L. Kritcher, O. L. Landen, H. J. Lee, R. W. Lee, C. Niemann, et al. Plasmons in strongly coupled shock-compressed matter. *Physical Review Letters*, 105(7):075003, 2010.

[219] H. D. Whitley, D. M. Sanchez, S. Hamel, A. A. Correa, and L. X. Benedict. Molecular dynamics simulations of warm dense carbon. *Contributions to Plasma Physics*, 55(5):390, 2015.

[220] S. Mazevet, V. Recoules, J. Bouchet, F. Guyot, M. Harmand, A. Ravasio, and A. Benuzzi-Mounaix. Ab initio calculation of X-ray absorption of iron up to 3 Mbar and 8000 K. *Physical Review B*, 89(10):100103, 2014.

[221] C. Fiolhais, F. Nogueira, and M. A. L. Marques. *A primer in density functional theory*, volume 620. Springer Science & Business Media, 2003.

[222] C. F. Schwenk, H. H. Loeffler, and B. M. Rode. Molecular dynamics simulations of Ca2+ in water: Comparison of a classical simulation including three-body corrections and Born-Oppenheimer ab initio and density functional theory quantum mechanical/molecular mechanics simulations. *The Journal of Chemical Physics*, 115(23):10808, 2001.

[223] B. M. Rice and E. F. C. Byrd. Theoretical study of shocked formic acid: Born-Oppenheimer MD calculations of the shock Hugoniot and early-stage chemistry. *The Journal of Physical Chemistry B*, 120(8):1711, 2015.

[224] P. Hohenberg and W. Kohn. Inhomogeneous electron gas. *Physical Review*, 136(3B):B864, 1964.

[225] F. Lambert, J. Clérouin, and S. Mazevet. Structural and dynamical properties of hot dense matter by a Thomas-Fermi-Dirac molecular dynamics. *EPL (Europhysics Letters)*, 75(5):681, 2006.

[226] C. Huang and E. A. Carter. Transferable local pseudopotentials for magnesium, aluminum and silicon. *Physical Chemistry Chemical Physics*, 10(47):7109, 2008.

[227] W. G. Hoover, A. J. C. Ladd, and B. Moran. High-strain-rate plastic flow studied via nonequilibrium molecular dynamics. *Physical Review Letters*, 48(26):1818, 1982.

[228] F. Zhang. Operator-splitting integrators for constant-temperature molecular dynamics. *The Journal of chemical physics*, 106(14):6102, 1997.

[229] J.-P. Hansen, I. R. McDonald, and E. L. Pollock. Statistical mechanics of dense ionized matter. III. Dynamical properties of the classical one-component plasma. *Physical Review A*, 11(3):1025, 1975.

[230] N. M. Gill, R. A. Heinonen, C. E. Starrett, and D. Saumon. Ion-ion dynamic structure factor of warm dense mixtures. *Physical Review E*, 91:063109, 2015.

[231] C. E. Starrett and D. Saumon. Models of the elastic X-ray scattering feature for warm dense aluminum. *Physical Review E*, 92:033101, 2015.

[232] L. Harbour, M. W. C. Dharma-Wardana, D. D. Klug, and L. J. Lewis. A critical assessment of models of pair-interactions and screening used in analyzing recent warm dense matter (WDM) experiments. *arXiv:1604.02453*, 2016.

[233] G. Dimonte and J. Daligault. Molecular-dynamics simulations of electron-ion temperature relaxation in a classical coulomb plasma. *Physical Review Letters*, 101(13):135001, 2008.

[234] J. N. Glosli, F. R. Graziani, R. M. More, M. S. Murillo, F. H. Streitz, M. P. Surh, L. X. Benedict, S. Hau-Riege, A. B. Langdon, and R. A. London. Molecular dynamics simulations of temperature equilibration in dense hydrogen. *Physical Review E*, 78(2):025401, 2008.

[235] Z. Moldabekov, P. Ludwig, M. Bonitz, and T. Ramazanov. Ion potential in warm dense matter: Wake effects due to streaming degenerate electrons. *Physical Review E*, 91(2):023102, 2015.

[236] P. Sperling, E. J. Gamboa, H. J. Lee, H. K. Chung, E. Galtier, Y. Omarbakiyeva, H. Reinholz, G. Röpke, U. Zastrau, J. Hastings, et al. Free-electron X-ray laser measurements of collisional-damped plasmons in isochorically heated warm dense matter. *Physical Review Letters*, 115(11):115001, 2015.

[237] S. A Khrapak, O. S. Vaulina, and G. E. Morfill. Self-diffusion in strongly coupled Yukawa systems (complex plasmas). *Physics of Plasmas*, 19(3):034503, 2012.

[238] O. Vaulina, S. Khrapak, and G. Morfill. Universal scaling in complex (dusty) plasmas. *Physical Review E*, 66(1):016404, 2002.

[239] Y. Feng, J. Goree, and B. Liu. Identifying anomalous diffusion and melting in dusty plasmas. *Physical Review E*, 82(3):036403, 2010.

[240] J. Dai, Y. Hou, and J. Yuan. Unified first principles description from warm dense matter to ideal ionized gas plasma: Electron-ion collisions induced friction. *Physical Review Letters*, 104(24):245001, 2010.

[241] P. Vieillefosse and J.-P. Hansen. Statistical mechanics of dense ionized matter. V. Hydrodynamic limit and transport coefficients of the classical one-component plasma. *Physical Review A*, 12(3):1106, 1975.

[242] A. V. Plyukhin. Generalized Fokker-Planck equation, Brownian motion, and ergodicity. *Physical Review E*, 77(6):061136, 2008.

[243] A. Ng, P. Celliers, G. Xu, and A. Forsman. Electron-ion equilibration in a strongly coupled plasma. *Physical Review E*, 52(4):4299, 1995.

[244] C. P. Flynn and R. S. Averback. Electron-phonon interactions in energetic displacement cascades. *Physical Review B*, 38(10):7118, 1988.

[245] M. W. Finnis, P. Agnew, and A. J. E. Foreman. Thermal excitation of electrons in energetic displacement cascades. *Physical Review B*, 44(2):567, 1991.

[246] A. Caro and M. Victoria. Ion-electron interaction in molecular-dynamics cascades. *Physical Review A*, 40(5):2287, 1989.

[247] A. M. Stoneham. Energy transfer between electrons and ions in collision cascades in solids. *Nuclear Instruments and Methods in Physics Research Section B: Beam Interactions with Materials and Atoms*, 48(1):389, 1990.

[248] P. Nozières and D. Pines. *The theory of quantum liquids*. Perseus, 1999.

[249] R. H. Williams and W. R. Chappell. Microscopic theory of density fluctuations and diffusion in weakly ionized plasmas. *Physics of Fluids*, 14(3):591, 1971.

[250] A. I. Momot and A. G. Zagorodny. Fluctuations in collisional plasma in the presence of an external electric field. *Physics of Plasmas*, 18(10):102110, 2011.

[251] P. Willmott. *An introduction to synchrotron radiation: Techniques and applications*. John Wiley & Sons, 2011.

[252] J. J. MacFarlane, I. E. Golovkin, and P. R. Woodruff. HELIOS-CR - a 1-D radiation-magnetohydrodynamics code with inline atomic kinetics modeling. *Journal of Quantitative Spectroscopy and Radiative Transfer*, 99(1):381, 2006.

[253] J. Amann, W. Berg, V. Blank, F.-J. Decker, Y. Ding, P. Emma, Y. Feng, J. Frisch, D. Fritz, J. Hastings, et al. Demonstration of self-seeding in a hard-X-ray free-electron laser. *Nature Photonics*, 6(10):693, 2012.

[254] S. Huotari, G. Vankó, F. Albergamo, C. Ponchut, H. Graafsma, C. Henriquet, R. Verbeni, and G. Monaco. Improving the performance of high-resolution X-ray spectrometers with position-sensitive pixel detectors. *Journal of Synchrotron Radiation*, 12(4):467, 2005.

[255] S. Ranganathan and S. Yip. Memory functions for kinetic theory models of density fluctuations in fluids. *Physica A: Statistical Mechanics and its Applications*, 100(1):127, 1980.

[256] J. P. Mithen, J. Daligault, and G. Gregori. Comparative merits of the memory function and dynamic local-field correction of the classical one-component plasma. *Physical Review E*, 85(5):056407, 2012.

[257] J. P. Mithen, J. Daligault, and G. Gregori. Extent of validity of the hydrodynamic description of ions in dense plasmas. *Physical Review E*, 83(1):015401, 2011.

[258] James P. Mithen, J. Daligault, B. J. B. Crowley, and G. Gregori. Density fluctuations in the Yukawa one-component plasma: An accurate model for the dynamical structure factor. *Physical Review E*, 84(4):046401, 2011.

[259] R. Schmidt, B. J. B. Crowley, J. Mithen, and G. Gregori. Quantum hydrodynamics of strongly coupled electron fluids. *Physical Review E*, 85(4):046408, 2012.

[260] J. E. Cross, P. Mabey, D. O. Gericke, and G. Gregori. Theory of density fluctuations in strongly radiative plasmas. *Physical Review E*, 93(3):033201, 2016.

[261] G. Salin and J.-M. Caillol. Equilibrium molecular dynamics simulations of the transport coefficients of the Yukawa one component plasma. *Physics of Plasmas*, 10(5):1220, 2003.

[262] J. E. Cross, B. Reville, and G. Gregori. Scaling of magneto-quantum-radiative hydrodynamic equations: From laser-produced plasmas to astrophysics. *The Astrophysical Journal*, 795(1):59, 2014.

[263] H. O. and S. Hamaguchi. Molecular dynamics evaluation of self-diffusion in Yukawa systems. *Physics of Plasmas*, 7(11):4506, 2000.

[264] Z. Donkó and P. Hartmann. Thermal conductivity of strongly coupled Yukawa liquids. *Physical Review E*, 69(1):016405, 2004.

[265] T. Saigo and S. Hamaguchi. Shear viscosity of strongly coupled Yukawa systems. *Physics of Plasmas*, 9(4):1210, 2002.

[266] K. Y. Sanbonmatsu and M. S. Murillo. Shear viscosity of strongly coupled Yukawa systems on finite length scales. *Physical Review Letters*, 86(7):1215, 2001.